Computer-based simulation of the effects of instrumental delivery on the fetal head

Vilius Audinis

School of Computing Sciences

University of East Anglia

A thesis submitted for the Degree of Doctor of Philosophy

May 2017

Abstract

Fetal head moulding is a phenomenon that happens during the process of human childbirth. Due to the highly deformable fetal scalp being in contact with the maternal anatomy, the shape of the fetal head changes. This can be beneficial when the fetal head dimensions are very similar to the dimensions of the female pelvis hence allowing the baby to progress safely through the birth canal. Conversely, excessive head moulding may have serious effects on the baby's wellbeing. The first part of this thesis presents a computer-based finite element model of fetal head moulding as an improvement on previously developed models. The second part of the research focuses on another cause of potentially excessive fetal head moulding, i.e. the incorrect use of obstetric instruments including the obstetric forceps and the ventouse (vacuum extractor). The degree of damage that may be caused by incorrectly placing a forceps (i.e. asymmetric placement of the blades) or a ventouse (i.e. placement on top of soft parts of the skull such as the fontanelles) was assessed by means of finite element analysis after developing a set of software tools to facilitate these experiments. The final results of this research included: an improved and more realistic model of fetal head moulding under conditions of normal delivery, and results that reveal the great potential of severe damage that obstetric forceps and/or the ventouse may cause to the baby's head when applied incorrectly.

Acknowledgements

First of all I wanted to thank my Mum, Dad and Brother. Thank you for providing me with enough love, support and happiness to be able to stand on my own two feet. Thank you to all my close friends and colleagues who have helped me and stayed by my side. Thank you to Zelim Gerikhanov!

I especially wanted to thank my Supervisor, Dr. Rudy Lapeer. Without his support, guidance and belief I would not have been able to see the end of this journey.

My biggest heartfelt thank you of all goes to my incredible wife, your love and support give me the strength to achieve my goals in life. I love you!

Contents

List of Figures

Glossary of Terms

- Aponeuroses - A sheet of pearly white fibrous tissue which takes the place of a tendon in sheet-like muscles that have a wide area of attachment [35]
- Bregma - The point where the frontal bone and parietal bones meet [36]
- Cardiotocography (CTG) - A technical means of recording the fetal heartbeat and uterine contractions during pregnancy and throughout labour
- Cephalohaematomas - Bleeding which occurs under the skin in the periosteum of the baby's skull bone. It causes unnecessary pooling of blood between the skull and inner layers of the skin but does not pose threat to brain cells [37]
- Cephalopelvic Disproportion - When the baby's head or body is too large to fit through the mother's pelvis [38]
- Cerebrospinal Fluid (CSF) - A clear, colourless bodily fluid found in the brain and spine. It acts as a cushion or buffer for the brain's cortex, providing basic mechanical and immunological protection to the brain inside the skull [39]
- Computerised Tomography (CT) - Also known as Computerised Axial Tomography (CAT) Scans, produce detailed images of inside the body including organs, blood vessels and bones. They do this by using computer-processed x-ray images which have been taken at multiple angles [40]
- Dura Mater - The tough outermost membrane which covers the brain and spinal cord
- Endomyometritis - Inflammation or infection of the endometrium - the inner lining of the uterus. It can be obstetric or non-obstetric [41]

- Endosteal surface - A thin vascular membrane of connective tissue that lines the surface of the bony tissue that forms the central cavity of long bones [42]

- Euclidean distance - The straight-line distance between two points

- Erb's palsy - Paralysis of the arm caused by injury to the upper group of the arm's main nerves. It most commonly, but not exclusively, arises from shoulder dystocia. It can resolve naturally over a period of months, require rehabilitative therapy or surgery [43]

- Finite element - A numerical technique for finding approximate solutions to boundary value problems for partial differential equations. It is also referred to as Finite Element Analysis [44]

- Haptics - The application of tactile sensation and control to interactions with computer applications

- Heuristic - An approach to problem solving which allows a person to learn or discover something for themselves, even if the method or means is not guaranteed to be perfect

- Infinitesimal area - An area so small it is usually unmeasurable

- Ischial spine - Forms the posterior border of the body of the ischium [45]

- Ischium - Forms the lower and back part of the hip bone [45]

- Levator ani - A broad, thin muscle situated on either side of the pelvis. It is formed from three muscle components: the puborectalis, the pubococcygeus muscle and the iliococcygeus muscle. These unite to form the greater part of the pelvic floor [46]

- Lower uterine segment - The inferior section of the uterus, the lower extremity of which joins with the cervical canal and, during pregnancy, expands to become the lower part of the uterine cavity. This is not the active contracting portion of the uterus [47]
- Magnetic Resonance Imaging (MRI) - A type of scan that uses strong magnetic fields and radio waves to produce detailed images of the inside of the body [48]
- Meninges - The three membranes that surround the brain and spinal cord. The primary function is to protect the central nervous system
- Multigravida - A woman who has been pregnant for at least a second time
- Multiparous - A woman who has had more than one child
- Nulligravida - A woman who has never been pregnant
- Occiput anterior vertex presentation - When the back of the baby's head is facing the mother's front [49]
- Occiput posterior vertex presentation- When the back of baby's head is against the mother's back [49]
- Parietal peritoneum - Lines the internal surface of the abdominopelvic wall and extends to the organs [50]
- Perineum - The area between the anus and the scrotum or vulva
- Peritoneal cavity - The potential space between the parietal peritoneum and visceral peritoneum [51]

- Peritoneum - helps support the organs in the abdominal cavity and also allows nerves, blood vessels, and lymph vessels to pass through to the organs. It consists of two parts; the parietal and visceral [50]
- Pfannenstiel incision - A transverse abdominal surgical incision. It allows access to the abdomen
- Placental abruption - When the placental lining has separated from the uterus of the mother prior to delivery [52]
- Placenta praevia - Exists when the placenta is inserted wholly or in part into the lower segment of the uterus [53]
- Primigravida - A woman who is pregnant for the first time or has been pregnant once
- Pudendal nerve - The main nerve of the perineum
- Rectus sheath - Is formed by the aponeuroses of the transverse abdominal and the external and internal oblique muscles [54]
- Sagittal suture - A dense, fibrous joint made of connective tissue between the two parietal bones of the skull
- Shoulder dystocia - After the delivery of the head, the shoulder of the baby becomes stuck behind the mother's pubic bone, delaying the baby's birth [55]
- Subgaleal / Subaponeurotic Hemorrhage - Bleeding in the potential space between the skull and scalp [56]
- Sub-occipito bregmatic (SOB) plane - Extends from the nape of the neck to the centre of the bregma [57]

- Subperiosteal space - The space beneath the periosteal - a dense layer of vascular connective tissue enveloping the bones except at the surfaces of the joints [58]

- Synostosed sagittal suture - Occurs when the suture at the top of the skull, in between the parietal bones, (the sagittal suture) fuses. This leads to a lack of growth in width and compensatory growth in length, resulting in a long, narrow skull [59]

- Umbilical cord prolapse - When the umbilical cord descends through the cervix before the presenting part of the fetus [60]

- Visceral peritoneum - Covers many abdominal organs including the stomach, spleen, liver, intestines (from the distal duodenum to the upper end of the rectum), uterus and ovaries [50]

1 Introduction

1.1 Childbirth and instrumental intervention

Human childbirth is a process all of us undergo and is often labelled the most risky event we are bound to experience during our lifetime. However, in the developed world, the field of obstetrics has come a long way in the last fifty years or so mainly thanks to the use of more powerful drugs and electronic monitoring equipment. As such, the probability of long-term morbidity or mortality of a newborn is relatively low. Nonetheless, there is still a small but significant percentage of childbirths that may result in an adverse outcome. One such outcome is failure to progress during the expulsion or second stage of delivery. Reasons for this outcome can be macrosomia (large baby), shoulder dystocia (baby's shoulder impacts with the maternal pelvis), malpresentation (for example, breech presentation in the worst case), etc. When failure to progress occurs, the first action that the obstetrician may take is use of instruments such as the obstetric forceps and ventouse (vacuum extraction) which allow the operator to exert more grip and additional force on the head (presenting part) of the baby. Correct use of obstetric instruments carries relatively low risk. However, incorrect placement of forceps blades or the vacuum extraction cup may cause severe injuries to the baby's face and scalp and in extreme cases may lead to death. The work presented in this thesis investigates the effect of instrumental delivery on the fetal scalp bones and underlying structures by means of a biomechanics model and finite element analysis (FEA).

1.2 List of contributions

1.2.1 Novel contributions to the field of research

The principal contribution to the research community by this thesis is the in-depth analysis of how the fetal skull is affected by the use of instrumental interventions during the second stage of labour.

This has been achieved by the improvement of various subject specific computer methods and methodologies and the creation of novel methods and ideas, which are outlined in this thesis.

To summarise, the main contributions are:

- An improved model of fetal head moulding during the first stage of labour based on earlier models. Improvements include areas such as fetal skull geometry, FE mesh quality, convergence and load models.

- An improved model of the fetal head-to-cervix pressure (HCP) based on earlier models. Improvements include the precise measurement of cervical dilatation.

- A novel method for calculating and applying forceps induced forces upon the fetal skull within a custom-built simulation environment.

- A novel method of calculating and applying ventouse related pressures and forces within a custom-built simulation environment.

- Finite element analyses of a large variation of realistic instrumental placements. Experimental results indicate clinically relevant conclusions that shed a better light on the nature of instrumental delivery during complicated childbirths.

1.2.2 Contributions by publications

A number of publications have resulted in part or primarily because of the content covered in this thesis. The currently published material and the sections of the thesis that they relate to are as follows:

- Conference: MICCAI 2014 - Medical Image Computing and Computer Assisted Intervention. Title: A Computer-Based Simulation of Obstetric Forceps Placement [61, 62]. Covered in Chapters 4 and 5.
- Conference: SIMULIA UK Regional User Meeting 2014. Title: Simulation of vacuum extraction during childbirth using finite element analysis [63]. Covered in Chapters 4 and 5.
- Conference: E-Health and Bioengineering Conference (EHB), 2013 - sponsored by the IEEE. Title: Towards a forward engineered simulation of the cardinal movements of human childbirth [64].
- Conference: 2nd European Conference in Simulation in Women's Health. Abstract.

Additional contribution by workshop:

- 1st European Conference in Simulation in Women's Health - Appendix B

1.3 Thesis plan & outline

The main aim of this study is to conduct a clinically significant investigation into the mechanical effects that the fetal skull may undergo during instrumental interventions. To achieve this, the following tasks had to be completed:

- The creation of a biomechanical model of fetal head moulding suitable for analysis using the Finite Element Method (FEM).

- The creation of a biomechanical model of the contact interaction between obstetric forceps and the fetal head suitable for analysis using the FEM.
- The creation of a biomechanical model of the contact interaction between vacuum extractor and the fetal head suitable for analysis using the FEM.

Chapters 2 through 7 describe the work that was done to achieve the tasks outlined above. The appendices provide additional supporting work that relates to that which is covered in the main body of this thesis.

Chapter 2

Describes an in-depth investigation into the different types of instrumental interventions, their clinical and physical implications as well as outlining various complications that could arise because of their use. Existing research in this field of study is also analysed and material relevant to the work required to achieve the outlined tasks is detailed.

Chapter 3

Describes the various software tools and computer algorithms as part of a simulation environment necessary to facilitate the main analyses on fetal head moulding and the effect of instrumental delivery.

Chapter 4

Covers the development of a new biomechanical model of fetal head moulding during the first stage of labour. Results of experimental analyses using the FEM are presented and discussed.

Chapter 5

Covers the development of biomechanical models of instrumental delivery including obstetric forceps and vacuum extraction. Results of experimental analyses using the FEM are presented and discussed.

Chapter 6

Concludes the thesis with a statement of what has been achieved and sheds light on where further improvements can be made in future work.

2 Background

2.1 The stages of labour

The process of giving birth is complicated, but is generally considered to have three distinct stages:

- First stage - During this stage contractions begin and progressively get stronger and more frequent. This is the stage during which the uterine cervix starts the dilatation process. In normal cases without complications, this stage is the longest of the three stages of labour and could last up to 20 hours, although for a multiparous woman, this stage is generally shorter (2-10 hours) [65].
- Second stage - Once the uterine cervix has become fully dilated at approx. 10 cm, the second stage of labour starts. This stage is considered to be the "pushing stage", causing the baby to make its way from the uterus to the vagina and ends when the baby has been fully delivered.
- Third stage - The final stage of labour is described as the stage during which the placenta is delivered, after which the normal process of labour is complete.

Since the main objective of this study is to analyse the effects of labour and instrumental intervention on the fetal skull, the third stage will not be discussed further.

2.1.1 First stage of labour

Intrauterine pressure cycle

The contractions experienced during the first stage of labour cause what is described as the intrauterine pressure (IUP) cycle, whereby the pressure within

Figure 1: Intrauterine pressure and fetal heart rate pattern [1].

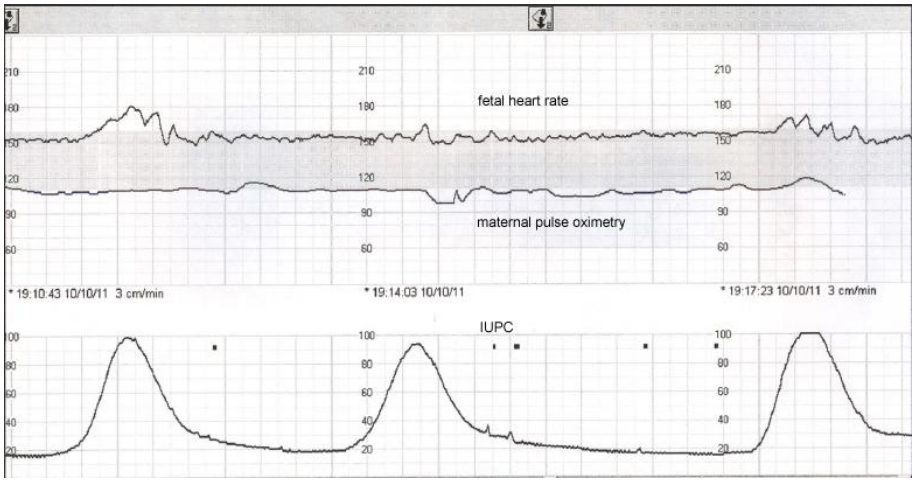

Figure 2: A detailed example of an intrauterine pressure pattern. The marked features are; Pp - Peak pressure, Pi - Peak intensity, Pb - Basal pressure, Tc - Period of contraction, Ti - Interval between contractions, Tr - Period during which the pressure rises. Figure based on the original in [1].

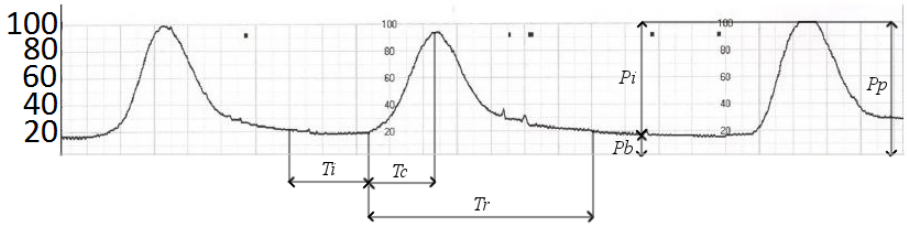

the uterus increases periodically thus expelling the fetus from within the uterus. Figure 1 shows an example of such a cycle together with the effects on the fetal heart rate and Figure 2 provides more details on the features shown by the pattern.

The visual pattern of the IUP cycle as shown in Figure 1, which is the result of what is know as cardiotocography (CTG), has a direct effect on the fetal heart rate. This relation between the two patterns is very important because it is the main indicator of fetal distress and whether additional help is required to expedite the labour process. An abnormal CTG may also indicate the need for an emergency Caesarean Section (CS). The IUP pattern as shown in Figure 2 is

characterised by:

- The basal pressure, Pb, denotes the IUP at rest in between contractions. It should remain within a similar range in between contractions as there should be no bearing down forces at this stage in the cycle.

- The maximum (peak) pressure of the IUP cycle, Pp, denotes the peak of each contraction.

- The intensity of the change in pressure, Pi, is the difference between Pb and Pp. A marked decrease in this value may indicate possible problems with the course of labour which may further prompt for assistance/intervention.

- The time between each contraction, Ti. The frequency of contractions in a cycle is measured in either 10 or 60 minute intervals depending on the current stage of the labour process. When the contractions are just starting at the beginning of the first stage of labour, the frequency will be too low to measure in 10 minute increments, but this changes as the end of the first stage of labour approaches.

- The contraction period, Tc, is the total duration of each contraction as visualised by the wave in a CTG.

- The period during which the pressure is increasing, Tr, is known as the period of rise of pressure.

Cervical effacement and dilatation

Before the onset of labour, the cervical rim thickness will be 2 - 4 cm and fully closed as shown in Figure 3. As the onset of labour starts, the thickness of the cervix will shorten as it becomes retracted and more malleable. The process of this "thinning" is called effacement and a cervix is fully effaced once dilatation

Figure 3: An example of a closed cervix without effacement. Image obtained from [2].

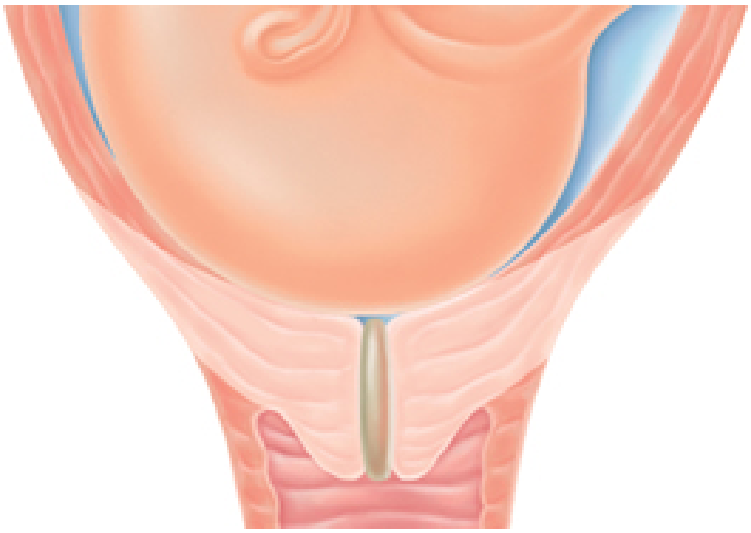

starts as shown in Figure 4. In simple terms, the process of cervical dilatation is the opening of the cervix from its closed state to its fully open state at approx. 10 cm as shown in Figure 6. The process of cervical dilatation is facilitated and is a direct result of the IUP with the rise in pressure resulting in an increase of the head-to-cervix (HTC) force [66].

2.1.2 Second stage of labour

Due to the persistent contact of the uterine cervix with the fetal head over a period of several hours (typically about 10 hours), the first stage of labour has a significant and guaranteed effect on fetal head moulding. This is why this dissertation focuses on the first stage of labour only and does not include moulding due to the substantially shorter second stage of labour (expulsion of the baby) which does not necessarily involve fetal head moulding and is also complex to model. In particular, the interaction with the bony pelvis and pelvic floor muscles requires non-linear soft tissue finite element models, including contact mechanics, which are beyond the scope of this thesis and only a brief account of

Figure 4: An example of an effaced cervix starting to undergo dilatation. Image obtained from [2].

the second stage is therefore provided.

The second stage starts when the cervix is fully dilatated to approx. 10 cm as shown in Figure 6. At this point in time, the uterus and the vagina make a continuous opening known as the birth canal through which the baby is delivered. In the majority of normal cases the fetal head exhibits a distinct set of movements called the "cardinal movements". The most essential cardinal movemments to allow the baby to progress through the birth canal are: flexion, internal rotation, extension and external rotation [64]. Furthermore the progress of the childbirth process is quantified by the fetal head station as described in the next section.

2.1.3 Fetal head station

The position of the head within the birth canal is classified according to its position relative to the ischial spines, i.e. -5 to +5 - see Figure 7. This classification system was implemented in 1988, by the American College of Obstetricians and Gynaecologists (ACOG). The 11 positions are referred to as stations, which for

Figure 5: Fetal head-to-cervix interaction. *Dmax* represents the point at which the uterine cervix will achieve a full dilatation of approx. 10 cm (note that due to omission of skin this value is approx. 9.5cm for the skull). $D1$ denotes the lower diameter of the head-to-cervix contact and $D2$, the maximum. *Fexp* represents the resultant force caused by the buildup of hydrostatic pressure during an Intrauterine pressure cycle.

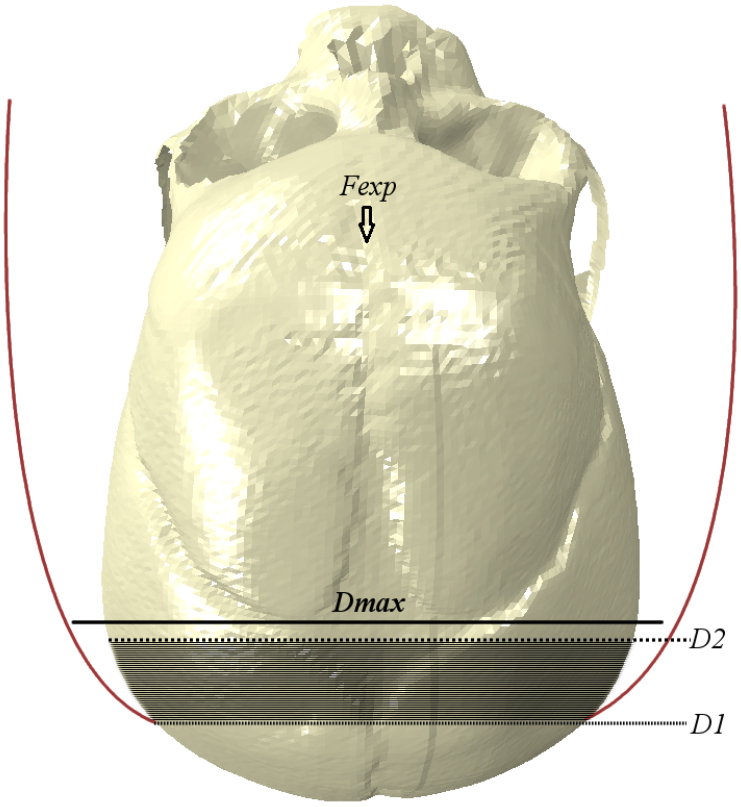

Figure 6: An example of a fully dilatated cervix. A partial section of an image obtained from [2].

clinical purposes have been divided into four groups [67]:

1. **High** - [-5, -4, -3, -2, -1]
2. **Mid** - [0, +1]
3. **Low** - [+2, +3]
4. **Outlet** - [+4, +5]

2.2 Interventional procedures

Although many cases of childbirth pass without any complications, operative delivery is still fairly common and varies between 10 - 13% for instrumental deliveries [68] and 20-30% for Caesarean Sections (CS) [69] in the UK. In cases where complications during labour result in a prolonged second stage, often labelled as 'failure to progress', delivery must be expedited using one of the following interventional procedures:

- Delivery with the use of obstetric forceps

Figure 7: Fetal head stations relative to the Pelvic Ischial Spines (marked in red). Fetal head position in this diagram is +0.5 but would most likely be evaluated to be either 0 or +1 (Mid Station) in a clinical setting. Diagram shown is an altered version of an image originally obtained from StratOG.

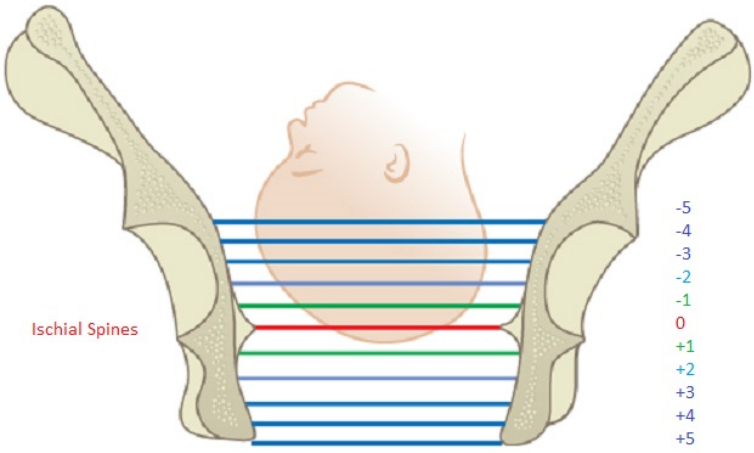

- Delivery with the use of the Ventouse or Vacuum Extractor (VE)
- Operative delivery by Caesarean Section (CS)

The instrumental methods are not mutually exclusive and can often be used in succession if any of them fail to progress the labour. In fact, in some cases the use of forceps after a failed vacuum extraction attempt is advised [68, 70].

Due to the reduced use of regional/general anaesthesia and less maternal trauma when compared with forceps, VE has become "the instrument of first choice" for many obstetricians [71, 72, 68]. However, the benefits of intervention by VE as opposed to forceps are still up for debate as there seem to be little or no difference between neonatal morbidity incidence rates [73]. The decline in forceps use has also been linked with the lack of available training (which we discuss later in the chapter). This is further compounded by the increasing trend to undergo CS, meaning that the application of existing training methods is becoming less frequent.

2.2.1 Caesarean section

In simple terms, CS is an operative method of delivering a baby. This procedure has existed in some form for many centuries, with some reports and anecdotal evidence appearing from the early 16th century [74]. Until the late 16th and early 17th centuries, the procedure used to be known as "caesarean operation". Gradually, the term "operation" was replaced with the term "section" following Jacques Guillimeau's 1598 book on midwifery in which the term "section" was introduced [74].

The exact description of what was to be achieved by this method of delivery varied widely throughout its history, but in most cases (especially before the 19th century), it would appear that this was an operation of last resort that would be performed on a dead or dying mother in order to try and save the life of the baby. This is by no means exclusive as there have been some reports of such procedures being performed on mothers that were able to survive.

In a modern context, this procedure is generally known as one of two scenarios:

- Elective CS - or planned CS. In these cases, the whole event has been planned and arranged before the onset of labour. The reasons for the use of this option over a natural vaginal birth are discussed in more detail later in this section.

- Emergency CS - or unplanned CS. Adopted when maternal or fetal complications arise either shortly before or during labour.

Indicators

There are a number of physiological factors that may result in the decision to deliver by elective CS.

- Cephalopelvic disproportion - This occurs when a baby's head or body is too large to fit through the mother's pelvis.
- Fetal malpresentation - Especially breech presentation, where the buttocks/feet are the presenting part at the uterine cervix.
- Multiple gestation - Although this is a strong indicator, it does not always lead to a CS intervention because a natural vaginal birth still remains a viable option in such cases.
- Placenta praevia - Low-lying placenta.
- Previous CS - In fact this is the leading cause for a CS to be performed again [68].
- Diseases - Such as active Genital Herpes or HIV.

Some of the major reasons for emergency CS are:

- Lack of progression using natural means.
- Failure to deliver using other instrumental means such as forceps and VE.
- Placental abruption.
- Non-Reassuring fetal heart rate trace - This could be caused by many factors, including oxygen deprivation (asphyxia).
- Umbilical cord prolapse.

The CS procedure in a nutshell

As with all operative procedures, there will be variations to the general case but for the most part the CS will be performed in the following major steps (these steps have been somewhat generalised to cover the main aspects without going

into excessive detail that would detract from the rest of the content covered in this thesis):

- Abdominal incision - This is the first step of the actual operative procedure which has a number of variants as shown in Figure 8. Although historically, the vertical midline incision (such as any of the vertical types shown in Figure 8) was used most often. The vertical incision type has fallen out of favour because it is considered less cosmetically acceptable, more painful and is also associated with more post-operative complications than the horizontal type incisions.

- Access to the uterus - This involves opening the initial incision to allow for better access to the underlying anatomy, i.e. the parietal peritoneum, which is then incised to open up the peritoneal cavity. The opening is then assessed to ensure there is adequate space for the delivery of the fetal head before incising the visceral peritoneum and proceeding to the next stage of the operation.

- Incision of the uterus - At this stage the uterus must be cut open to gain access to the fetus held within. The uterine incision is followed by the rupturing and opening of the amniotic sac.

- Delivery of the fetus - At this point the baby is delivered through the opening.

- Next, the placenta is delivered.

- Closure and drains - The cavity is drained of fluids and cleaned before it is closed and left to heal, forming a scar. The quality of the repair at this stage has very important implications for future pregnancies and is discussed in more detail in section 2.2.2.

Figure 8: Types of uterine incisions for Caesarean Section, as shown by [3]

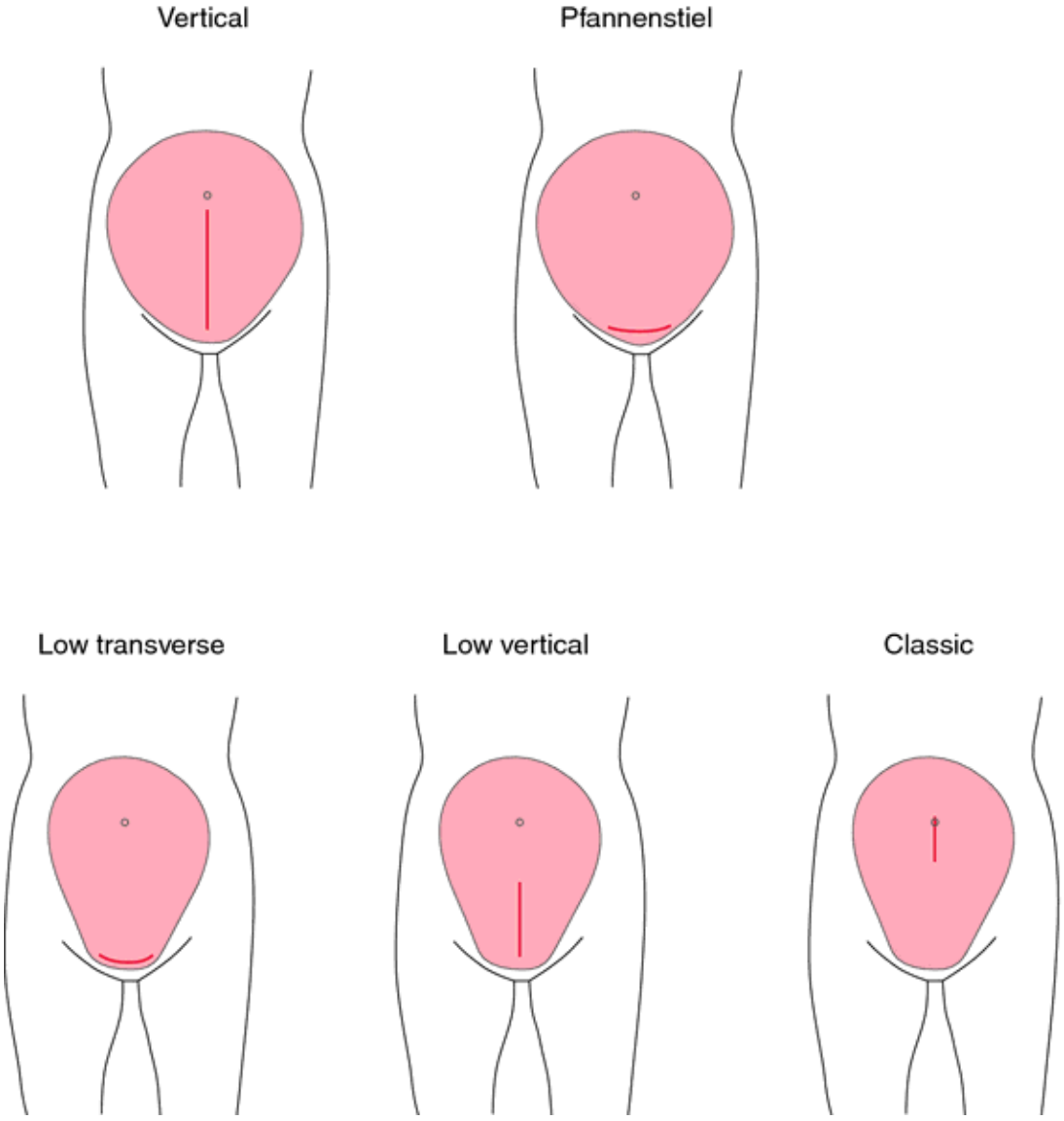

Complications associated with CS

In modern times CS has become a far safer procedure than it has been historically. This has been largely due to improvements to operative techniques and the application of anaesthetics. There remain a large list of complications that are associated with CS and these are generalised as being either intraoperative or postoperative. Of all possible complications associated with the procedure, there is one complication that can be described as the worst possible outcome:

- Maternal mortality - This can happen due to a large number of factors which can happen during the operation as well as during the postoperative recovery stage.

Other, less serious complications include, but are not limited to:

- Urinary tract injury
- Gastrointestinal tract injury
- Infection
- Endomyometritis
- Placenta praevia
- Incomplete scar healing
- Uterine scar rupture
- Low blood pressure - Blood pressure drops can be commonly seen as complication of the spinal anaesthetic.

Figure 9: "The Air Tractor" as presented by James Young Simpson on 20/12/1848, to a meeting of the Edinburgh Obstetric Society [4]

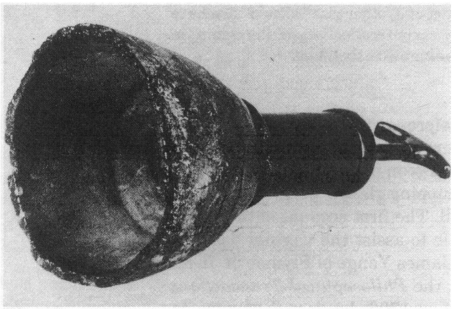

2.2.2 Vacuum extraction

Unless an elective CS was planned, VE is generally considered to be the first type of instrumental intervention to attempt when labour fails to progress.

First attempts of VE were made in the first half of the 18th century. Early designs of these instruments were mostly derivations of the cupping technique but because such use in obstetrics required a stable vacuum to be formed and maintained, creating a viable instrument proved difficult. The first vacuum based instrument with some degree of success in obstetrics was first presented in 1848 by James Young Simpson. "The Air Tractor", as shown in Figure 9, was a simple device consisting of a cup attached to a metal syringe used to create a vacuum.

The reason for its limited success was due to the following:

- The lack of pelvic curvature of the external surface of the cup limited the application of the device when higher applications were required.
- Much like other devices of the time, the instrument lacked any way of replenishing the vacuum once the initial evacuation of the syringe was completed.
- The inability to replenish the vacuum meant that the suction force was limited, affecting the chances of a successful intervention before the cup

Figure 10: Malmström's obstetrical vacuum extractor, Gothenburg, Sweden, 1979 [5].

became detached from the fetal head.

The instrument proposed by Simpson did not get any further development and applications of VE diminished in the context of obstetric applications for over a century. In 1957 Dr Tage Malmström developed a new type of extractor which uses a metal suction cup and a better pump capable of replenishing the vacuum once the cup has been attached to the fetal head. The initial design had issues and was continuously improved upon, leading to widespread use in Europe [73], with the device shown in Figure 10 being the end result. This device addressed all of the limitations of Simpson's VE, including the limited traction force that could be exerted.

The basic principle of VE has changed little in the years that followed, with main advances being in the form of changes in cup materials (with the move to hard plastic and rubber materials) and miniaturisation to make the equipment smaller. These improvements have led to the development of small disposable

Figure 11: 'Clinical Innovations Kiwi' hard plastic cup ventouse [6].

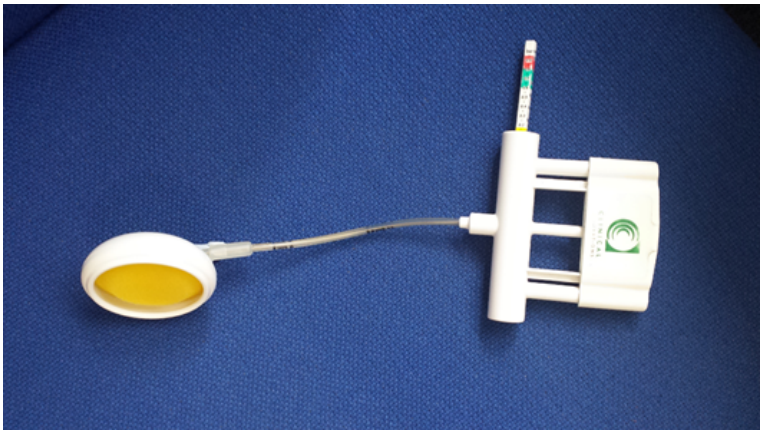

Figure 12: 'Clinical Innovations Kiwi' hard plastic cup ventouse as applied to a baby head model (ESP ZKK-240K) [7].

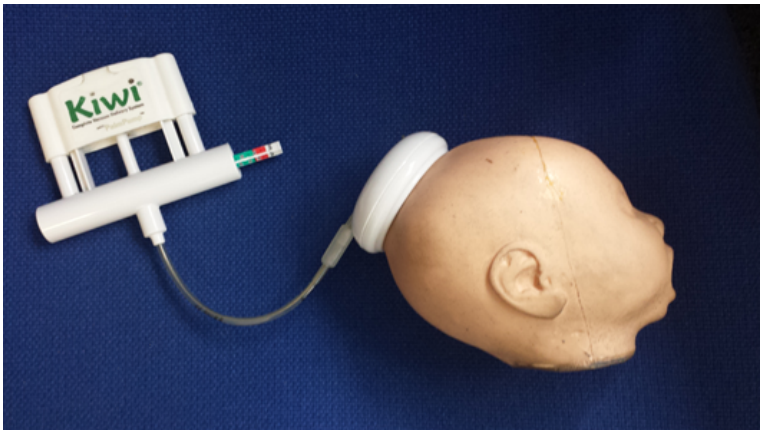

VE instruments such as the 'Clinical Innovations Kiwi' hard plastic cup ventouse as shown in Figure 11 and Figure 12.

Risks associated with VE

As with all obstetric interventions, VE also carries some risks to the mother and the baby. Some of the complications that can result are:

- Scalp wounds (mostly superficial) - The process is likely to leave some markings or deformations on the baby's head. But commonly this is a superficial injury that goes away quickly.

- Haematoma - Different types of heamatomas such as a cephalohaematoma or a subgaleal haematoma can result. For further clarification, a cephalohaematoma means bleeding is contained within the fibrous covering of the skull bones and is a relatively minor issue. When blood accumulates underneath the scalp, a subgaleal haematoma, then the issue becomes a life-threatening condition.

- Haemorrhage - Are similar complications to the haematomas as they also involve blood loss. Figure 21 lists many more variations.

2.2.3 Obstetric forceps

The use of forceps for assisted vaginal delivery was introduced after their invention in the early 17th century. Even with additional methods of instrumental intervention available, the use of forceps remains widespread [73, 37, 70, 72] and are generally introduced in the second stage of labour, when for a number of possible reasons, normal delivery can no longer continue. In general terms, the choice of instrument is governed by the delivery ward management policy and practices, meaning that forceps will not necessarily be the first option of intervention and as described in the previous section is likely to be the second option after VE [72, 71].

Figure 13: An example of a Neville-Barnes forceps [8]

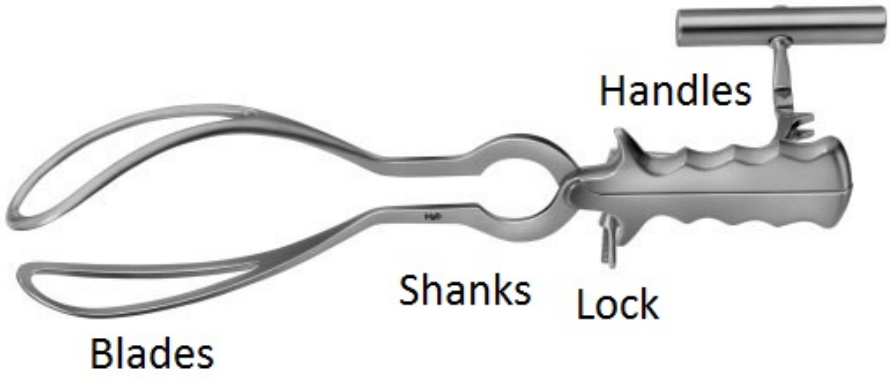

By design, forceps consist of four sections that allow the head of the neonate to be grasped, whilst the practitioner pulls on the handles providing traction and/or rotation in order to assist a troublesome delivery:

1. **Blades** - Arguably the most important part of the instrument, the design of the blades incorporates two types of curvature. The cephalic curve adapts to the neonate's head whilst the pelvic curve adapts to the path of the birth canal allowing for easier navigation. Examples of various curvatures can be seen in Figure 14. The importance of the blade shape and the interaction it has with the fetal head is further described and investigated in Chapter 5.

2. **Shanks** - The neck of the instrument; they often vary in length depending on the application but in most cases the shanks are two parallel bars which can sometimes be crossed.

3. **Lock** - This is the method of securing the separate sections of the instrument together after they have been inserted and positioned. The actual locking device is known to vary amongst various forceps designs.

4. **Handles** - This is the section used by the practitioner to apply traction

Figure 14: Forceps and curvature examples [8]. Top row left; Kielland forceps. Top row right; Simpson-Braun forceps. Bottom row left; Simpson forceps. Bottom row right; Wrigley forceps.

and/or rotation. As with the other sections of the instrument, these are known to have many variations and further attachments to help increase the traction force.

Forceps intervention techniques

There are three classifications of forceps delivery and they all relate directly to the four groups of fetal head station evaluations that were described in Section 2.1.3. The three classifications are as follows [68, 75, 76]:

1. **High Forceps** - This relates to the High position group in the aforementioned classification. In such cases a delivery by the use of forceps is rarely performed, because in this position the head is very rarely engaged and performing such a delivery is known to have very high morbidity rate to both the neonate and the mother. In such cases, CS is the common course of action [77, 78, 69].

2. **Mid Forceps -** As with the previous method this relates directly to the Mid classification. This method of delivery is performed only if the fetal

head is engaged in order to avoid excessive harm to the neonate. Engagement of the head is determined by a number of abdominal and vaginal examinations. CS is the common alternative if the use of forceps is deemed too dangerous. At this point the fetal head is in an occipital position meaning that the practitioner must first correct the position by rotation before any traction is applied (this is one of the advantages of using obstetric forceps). Mid forceps deliveries require the use of rotational forceps. Rotational forceps do not have a pelvic curve so that the fetal head can be rotated safely (see Figure (14) for an example of such forceps type).

3. **Low Forceps** - This method relates to the Low and Outlet groups of positional classification. This procedure is the most common procedure which occurs when the fetal head has reached the perineal floor and is visible at the vulva. Since there is no need for any rotation to be performed, the forceps blades have curves as shown in Figure 13. This is also the stage where VE is becoming the chosen method of delivery. More discussion and investigation on this stage of instrumental delivery is done in Chapter 5.

Forceps intervention example

Before forceps are introduced, the precise position of the fetal head is obtained by the operator. It is of utmost importance to know when to stop applying pressure on the forceps to avoid head trauma. Knowing when to stop is also critical as failing to do so could prove to be highly damaging and possibly result in morbidity. The application of forceps in a low forceps delivery mode will now be reviewed. Note that this is only a standardised method of delivery which can vary depending on the type of forceps and the ability of the operator. The outlined steps are presented as described by Maternal and Childhealth Advocacy International (MCAI) [9].

Figure 15: Introduction of the left forceps blade in to the birth canal [9].

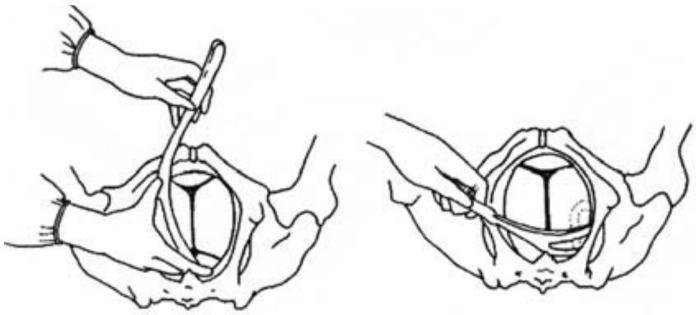

1. Ideally the sagittal suture should be in the midline and straight, guaranteeing an occiput anterior or occiput posterior position.

2. Provided that the above is true, the left blade is then introduced, as shown in Figure 15.

3. Once the left blade has been positioned the right blade is introduced. See Figure 16.

4. The blades are then locked into place as shown in Figure 17. If there is difficulty locking the blades they are usually repositioned before locking is attempted again.

5. Once the forceps have been locked into place, steady traction is applied in time with each contraction. See Figure 18.

Risks of forceps interventions

All instrumental interventions have their inherent risks, according to a number of publications and training materials [79, 80, 68, 75]. Some of the main risks posed by forceps include:

Figure 16: Introduction of the right forceps blade in to the birth canal [9].

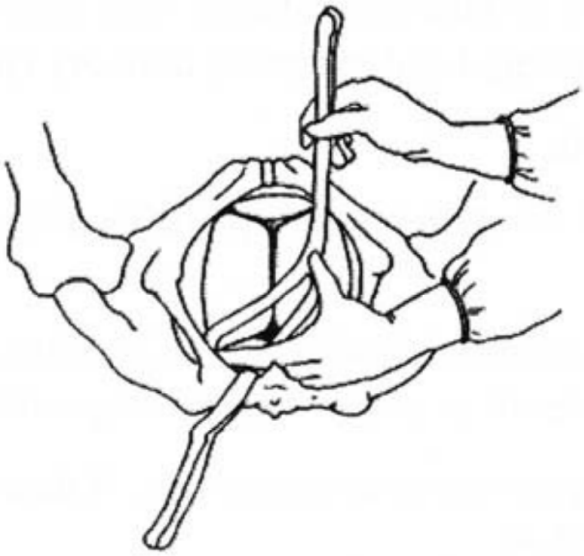

Figure 17: Lock both forceps blades [9].

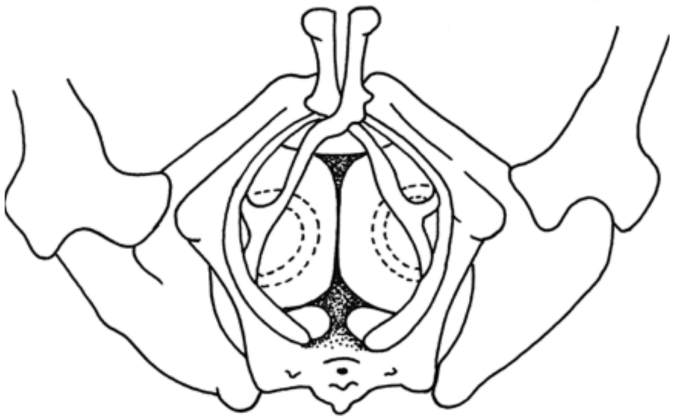

Figure 18: Using the forceps, apply traction to the head in time with each contraction and bearing down effort [9].

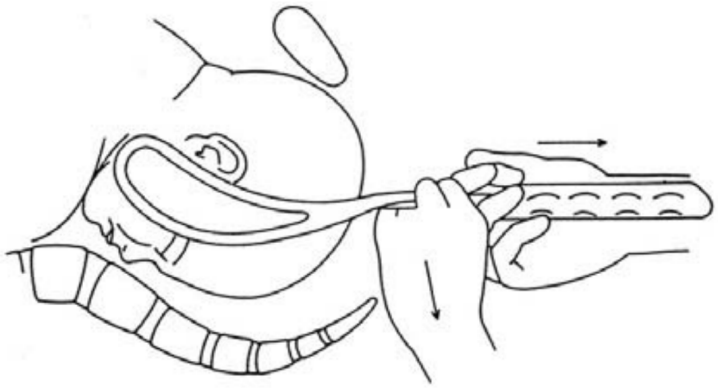

1. **Forceps Marks** - It is common to witness some soft tissue damage to the face and head after the use of forceps (as shown in Figure 19). Sometimes these can be of a more serious nature for example in the case of skin lacerations but these are seldom life threatening.

2. **Cephalohaematomas** - These are collections of blood confined by the subperiosteal space of the bone where they occur as shown in Figure 20 and Figure 21.

3. **Subgaleal / Subaponeurotic Haemorrhage** - Potentially a very serious complication resulting in a mortality rate of up to 20% of cases [81].

As with fetal complications, there are a number of maternal injuries and complications that can arise. The most common of these are:

1. **Lacerations** - Perineal lacerations and episiotomy extensions are common complications (see Figure (22)). The latter being the most common with the use of forceps. Episiotomy based deliveries have been linked to an increased chance of anal sphincter muscle damage leading to later complications [82, 83, 41].

Figure 19: An example of a skin mark left by a forceps application [10]

Figure 20: Skull radiographs showing lateral and frontal views of a soft tissue mass overlying a synostosed sagittal suture. Image adapted from [11]

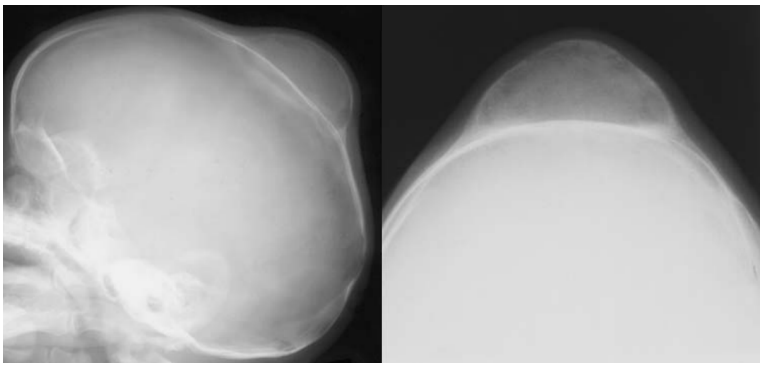

Figure 21: Fetal haemorrhage types

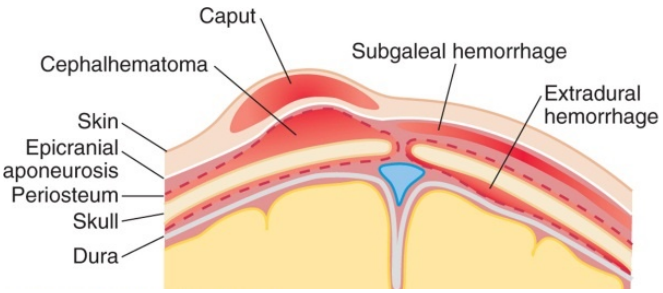

Figure 22: Visual representations of vaginal/perineal tearing. Top row left; first degree tear. Top row right; second degree tear. Bottom row left; third degree tear. Bottow row right; fourth degree tear [12]

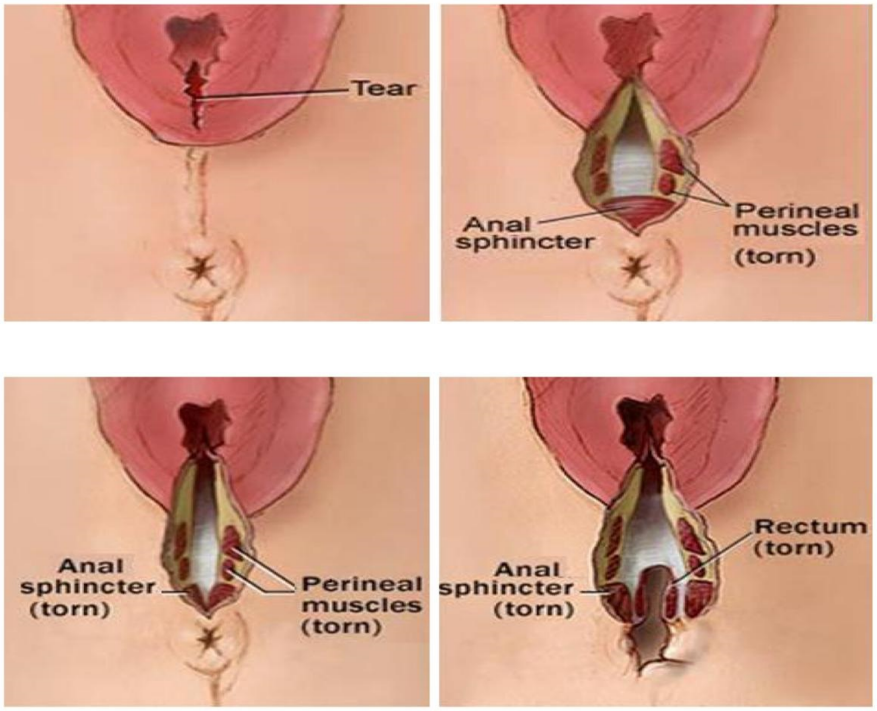

2. **Stress urinary and anal incontinence** - A common result of any vaginal delivery [84].

2.3 Training and computer simulation in obstetrics

2.3.1 Mechanical simulation

The first account of a mechanical 'birth simulator' dates back to as early as 1759. Angelique du Coudray Le Boursier, a French midwife, developed the 'Machine a Accoucher' - Delivery Machine - which rather than being a 'machine', consisted of mannequin models of the mother and fetus; The former comprising the maternal pelvis, the perineum and the legs, whilst the latter was an articulated floppy doll. Materials used included leather, wicker and cotton [85]. The

maternal mannequin's legs rested on an iron support. Apparently, the original model comprised a cadaveric bony pelvis of a young woman. Mechanical birth simulators developed later aimed to improve upon this concept by using better models of the maternal pelvic region and the fetus. More recently, commercial simulators such as the PROMPT trainer by Limbs & Things, Ltd., and Noelle and Victoria by Gaumard are state of the art dummy-based mechanical simulators and are mainly used for training of delivery and monitoring skills for apprentice midwives and obstetricians.

2.3.2 Virtual simulation

Visualising and simulating the birth process on computers is a relatively recent development [86][87][88]. In 1993 J.-D. Boissonnat and B. Geiger published details on their novel approach to a birth simulation using a virtual environment [89][90] as shown in Figure 23. The simulation environment consisted of a female pelvis and a fetal head modelled from Magnetic Resonance Imaging (MRI) data using a type of spatial triangulation method developed by the authors. The MRI data used was not that of a pregnant woman but instead that of a non-pregnant woman adjusted to mimic what the former would look like. Similarly, the fetal head model was derived from an MRI scan of an adult head. Difficulty in obtaining the required pregnant data was cited as the reason for this modelling approach. Given the simplicity of the simulated environment and the lack of any significant interface with it, the clinical value of this exercise is questionable. The authors themselves state that further development and testing within a clinical environment would have to be undertaken before any clinically significant outcomes could be derived.

Another publication in 1993 by K. Lehmann et al. also proposed a computer based simulation for the prevention of birth trauma [91]. Geometry was

Figure 23: Example of a 3D simulator developed by J. -D. Boissonnat and B. Geiger Source: [13]

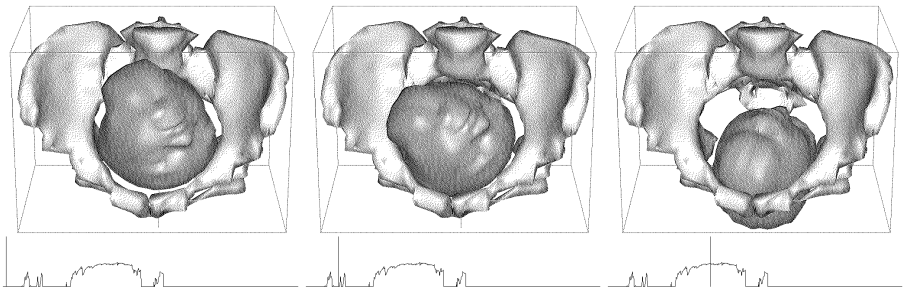

extracted using MRI data. The extracted geometry was then used to create a set of Finite Element (FE) meshes. These were then run in a simulation environment to extract information on the possible forces exerted during the birthing process. Clearly this approach seems superior to the one taken by Boissonnat and Geiger largely because soft tissue was considered in the simulation environment, but much like Boissonnat's and Geiger's simulator, further work needed to be undertaken to determine the clinical significance and accuracy of this simulation.

Y. Liu et al. [14] describe yet another attempt at modelling the birthing process. Unlike the preceding simulators, geometric representation of the maternal pelvis has been constructed from a set of Computed Tomographic (CT) pelvimetry data. The reconstruction process involved a number of different steps, some automated some manual. The fetal anatomy was initially obtained from ultrasound images and later from x-ray CT and MRI data - see Figure 24. Unlike the process of extracting the pelvic information, the process involved in reconstructing the fetal data remains unclear. The simulation environment focuses on cephalopelvic disproportion. The authors stipulate that it is the difference between the size of the maternal pelvis and the fetal size that is the problem in the active management of labour. In order to simulate this effect the approach taken was to alter the bony pelvic geometry by fitting a smooth surface around

Figure 24: MRI and CT Reconstruction of the fetal head. Source: [14]

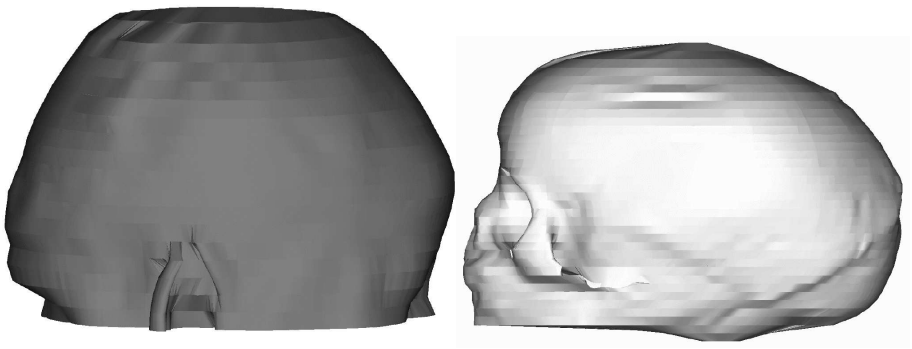

Figure 25: Pelvic model with a smooth inner surface. Source: [14]

the inner surface as shown in Figure 25.

The purpose of reconstructing the fetal data from several different sources remains unexplained by the authors. The full simulation shown in Figure 26 clearly shows that the geometry does not correspond to either of the examples shown in Figure 24. It is possible that a merging procedure was performed to obtain a final fetal head model but without further information from the authors this would only be speculation. This fact throws into question the accuracy and clinical significance of the simulation environment, which seems at best only a slight improvement over the work done by Boissonnat and Geiger [90].

The maternal pelvis and fetal head approach was further investigated by Forster et al. in 2001 [15]. The birthing simulator called Anapelvis (shown in

Figure 26: Example 3D simulator developed by Y. Liu et al. Source: [14]

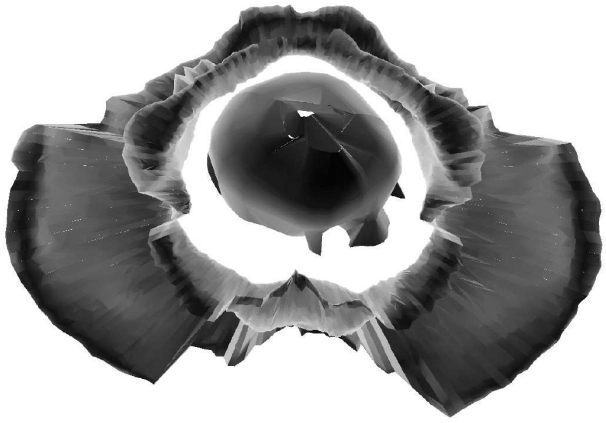

Figure 27: Anapelvis example. Source: [15]

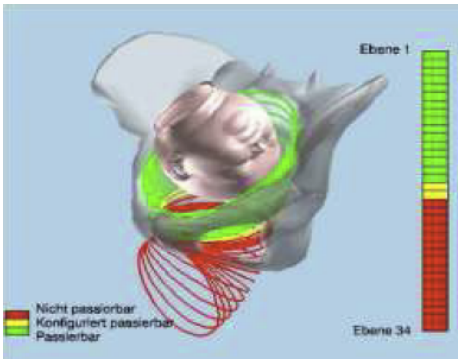

Figure 27) was developed based on the approach used by Boissonnat et al., but unlike the other simulators it was evaluated within a clinical setting. In a period of two years the system was used in 71 different cases. The stated accuracy of the simulation in predicting an accurate outcome is significant, confirming the viability of a virtual simulation.

A 2003 publication by B. Gonik et al. [16] describes a mathematical dynamic computer model used for determining birthing forces that are associated with the onset of shoulder dystocia (SD). Unlike any of the other virtual birthing simulators described thus far, the authors of this paper propose the use of an existing commercial computer software package MADYMO used by the automotive

Figure 28: MADYMO example. Source: [16]

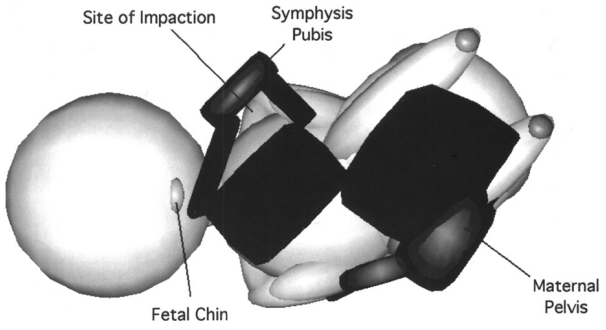

industry. MADYMO was used to model a visually simplistic, but mechanically sound representation of a fetus as shown in Figure 28. The simulation environment also includes a number of simplified pelvic sections, also shown in Figure 28. The approach taken by Gonik et al. [92] has produced a very specialised simulation environment that allows for detailed analysis of major forces believed to be the main cause of shoulder dystocia (SD). The authors stipulate that although important, the clinical significance of the results and observations of the simulator remain unclear.

In 2004, Kheddar et al. developed a more advanced birthing simulator capable of modelling the pelvic muscles [17][93] as shown in Figure 29. As with all preceding simulators, the maternal pelvis was reconstructed from medical imaging techniques such as MRI and CT. The pelvic muscles were modelled as a type of skeletal muscle with biomechanical properties as specified by Fung[94]. Interestingly the fetal model was not based on any medical imaging data but instead was manually constructed and then scaled to match average fetal dimensions described in a number of publications [95][19]. Another important aspect of this simulator is the inclusion of a haptic interface that allows for physical manipulation by a user of the system. The haptic interface allows for this simulation environment to be used not just for planning and prediction but also for training purposes akin to the mechanical simulators described in the previous section.

Figure 29: A haptics enabled simulation. Source: [17]

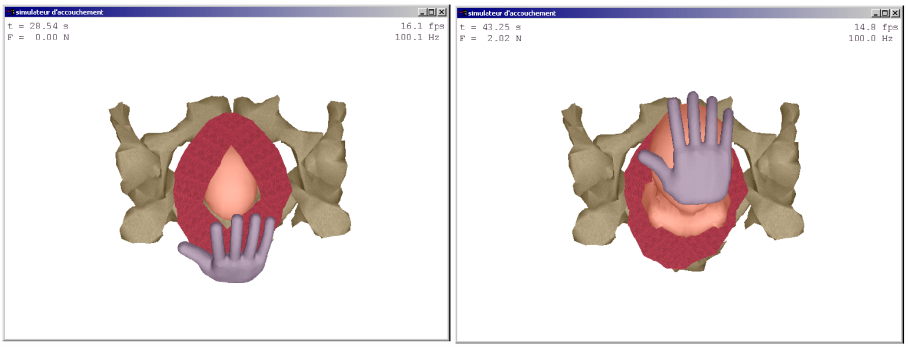

Figure 30: Fetal topology reconstruction. Source: [18]

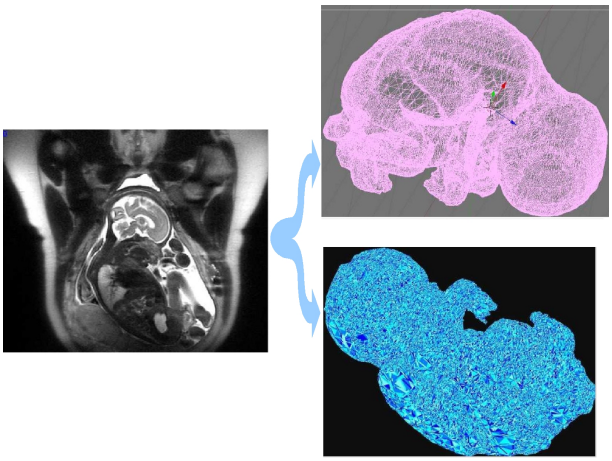

In 2009, R. Buttin et al. published details of arguably the most complex birthing simulator to date [18]. The simulation environment not only considers the bony pelvic structure and fetus but extends the soft tissue modelling aspect far beyond that of Kheddar et al. Although the common procedure of extracting pelvic topology from medical imaging data was once again repeated here, the fetal information was also extracted in the same manner. Rather than adapt a fetal model, an actual in situ fetus was extracted and reconstructed as shown in Figure 30. This is of great importance, as it is the first time a virtual simulator has such an accurate fetal representation.

To save on computation time, all aspects of the simulation environment were

Figure 31: Simplification of the maternal pelvic model. Source: [18]

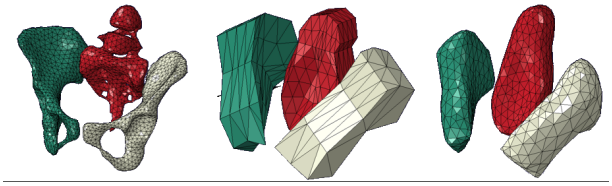

Figure 32: Simplification of the fetal model. Source: [18]

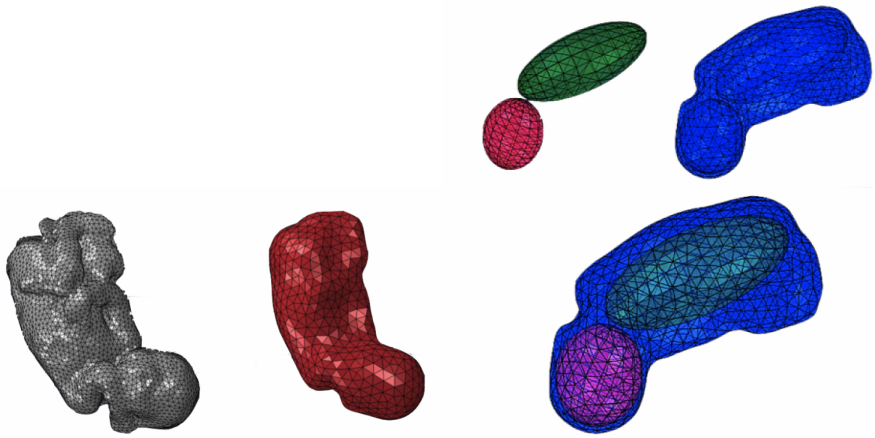

then simplified. This does bring into question the need to extract very accurate models from medical data if they are going to be simplified to the extent shown in Figure 31 and Figure 32. One other shortcoming of this simulation environment is the lack of any accurate fetal articulation. The authors do describe a simple articulation of the head which is modelled by the deformation of the fetal skin tissue as shown in Figure 33 but this limits the scope of the simulation environment.

2.3.3 Specialised virtual simulation

Due to the complexities of simulating and visualising childbirth, the majority of the simulation environments covered in the previous section had to greatly simplify the problem domain [96][21][22].

In 1999 R. J. Lapeer published a thesis describing the process by which fe-

Figure 33: Fetal articulation example. Source: [18]

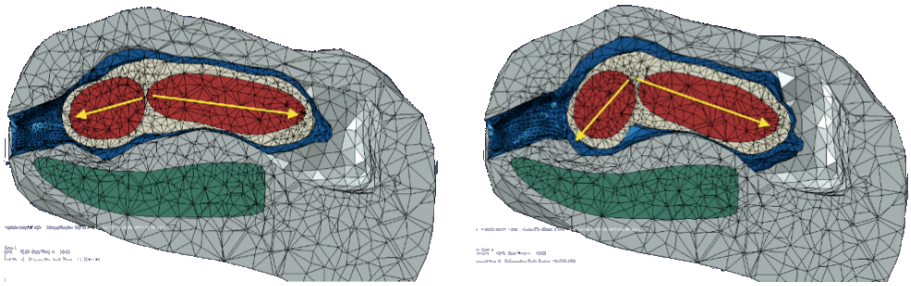

Figure 34: Example of fetal head moulding. Source: [19]

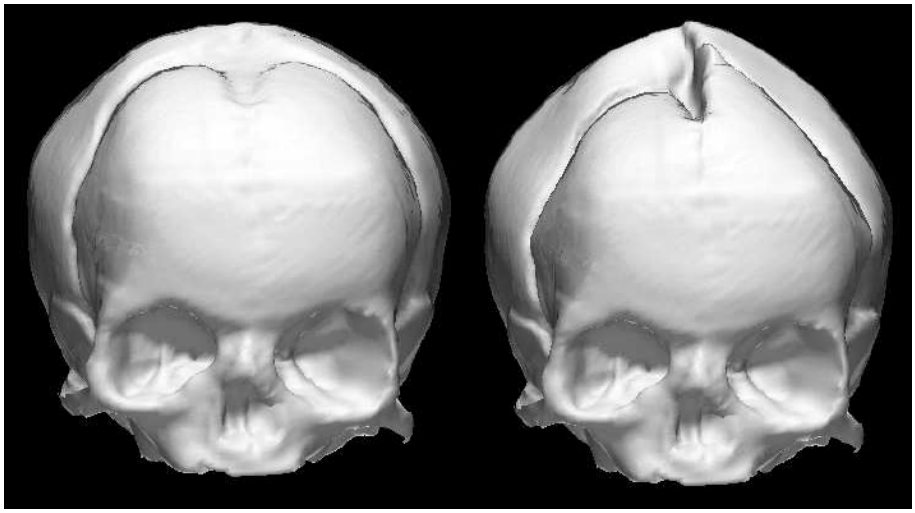

tal head moulding could be simulated [19]. The purpose of the project was to develop a simulation environment capable of modelling the intra-uterine forces that affect a fetal skull during the first stage of labour that cause it to deform as shown in Figure 34. By accurate representation of the anatomical biomechanical properties, Lapeer was able to simulate the fetal moulding to a clinically significant degree. The process of simulating fetal head moulding was further explained in a paper published by Lapeer and R. W. Prager in 2001.

The effects childbirth has on the pelvic floor is also an area of great interest [95][13][22][21] and a number of virtual simulation environments attempt to model aspects of this. A 2005 paper by Delancey et al. describes a simulation of

Figure 35: Pudendal nerve simulation example. Source: [20]

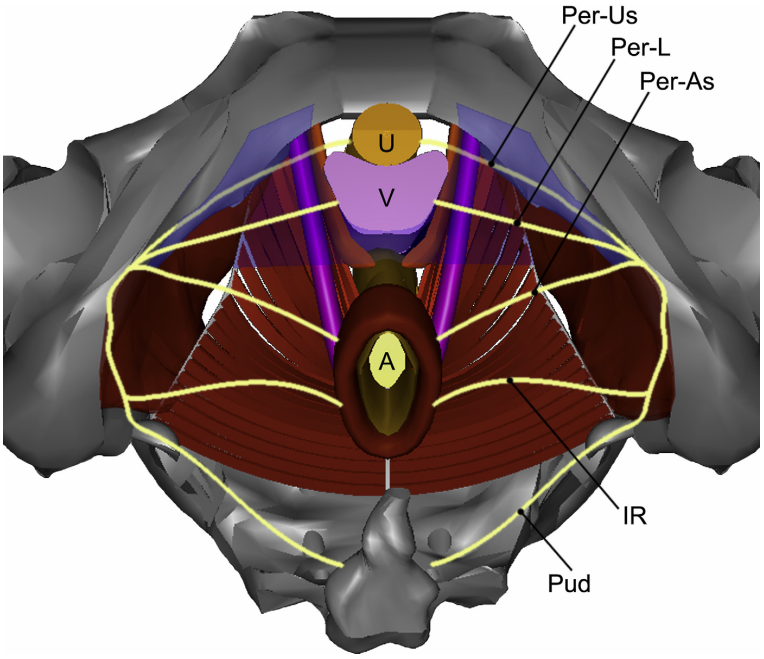

pudendal nerve stretch during vaginal birth [20]. The geometry of the nerve and its main branches were modelled on a number of cadaver dissections. The simulation environment makes use of an existing pelvic model from I-DEAS software, to which the nerve model is attached, as shown in Figure 35.

In 2008, L. Hoyte et al. published a paper [13] describing a method of determining the quantity and distribution of the levator ani (pelvic floor muscle) stretch during a childbirth simulation. The maternal pelvis and its levator ani muscle were reconstructed from medical imaging data obtained from a young nulligravida as shown in Figure 36. An FE model of the muscle was then created and analysed in a simulation which forced a fetal sized object through it, as shown in Figure 37.

Another paper also published in 2008 by Parente et al. [21] investigates the stretch to the levator ani muscle. The authors reconstructed the muscle from a set of geometric point data as shown in Figure 38 but unlike the subject data

Figure 36: Maternal pelvis and levator ani. Source: [13]

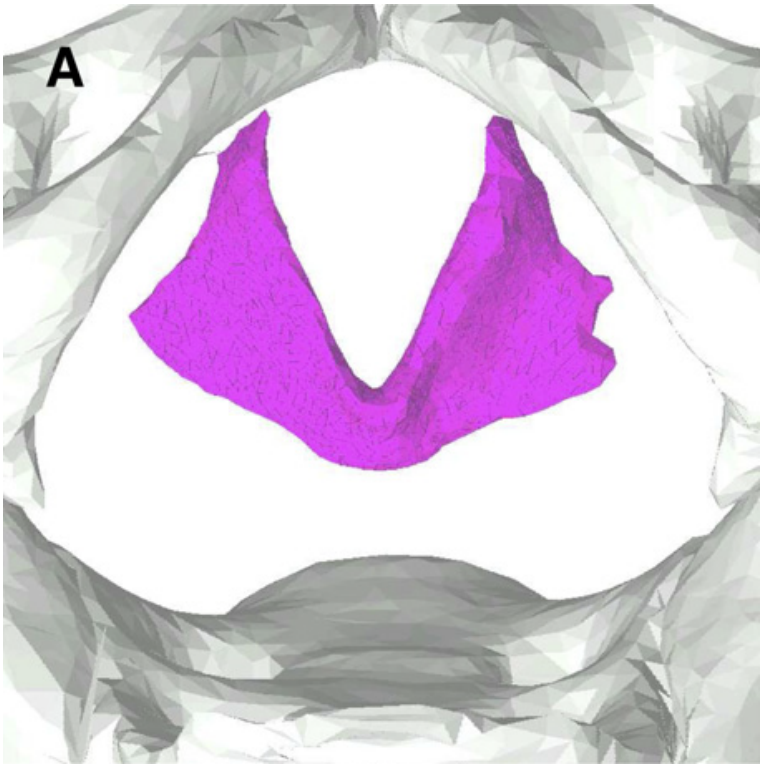

modelled by Hoyte et al. the dataset for this project was obtained from an embalmed 72-year-old female. The development in this area of birth simulation provides interesting insight into how the pelvic floor behaves during childbirth and may provide important quantitative information when applied to a more generic birth simulation environment.

Parente et al. further developed the simulator described in their 2008 paper [21] and published a set of new results based on the additional work [22]. The focus of the paper was to investigate the effects that a malpositioned fetal head would have on the pelvic floor. The simulation featured a fetal model based on the principal obstetric dimensions of the fetal head. The fetal model used by Parente et al. had no articulation since the simulation only required the fetal head to obtain results. The trunk of the body as seen in Figure 39 seems to be included for completion purposes only. The numerical simulation was performed

Figure 37: Levator ani stretch due to fetal head. Source: [13]

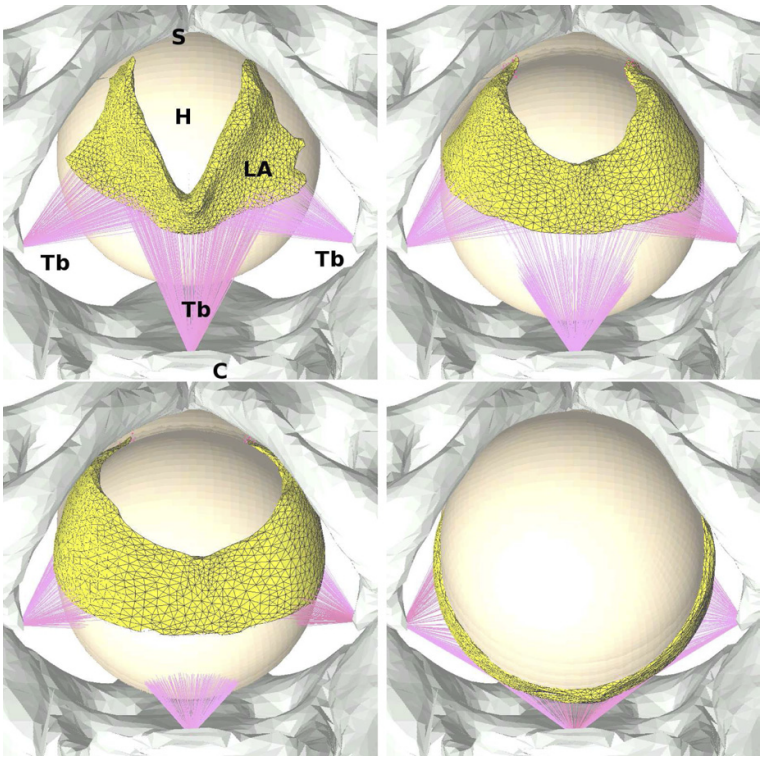

Figure 38: Levator ani reconstruction. Source: [21]

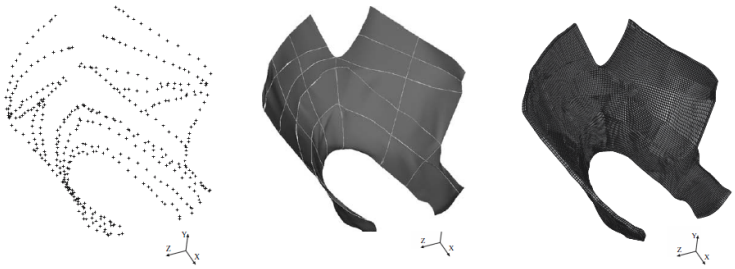

Figure 39: Simulation example by Parente et al. Source: [22]

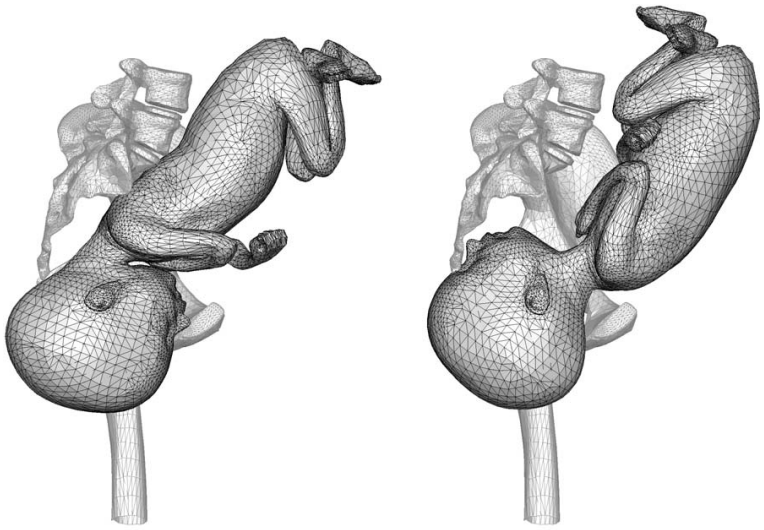

using the implicit version of ABAQUS software.

2.3.4 Hybrid simulation

Unlike the mechanical simulators, one major shortcoming for most of the virtual simulators described in the previous section is the lack of any physical interface. This limits the use of the simulation in a training environment. To overcome this shortcoming a number of hybrid simulators have been developed. These are systems with physical models interfacing to some extent with a computer to obtain visual/numerical results.

An example of this approach can be seen in a 1989 paper published by B. Gonik et al. [23]. They describe a way of evaluating the effect that a maternal pelvic orientation has on force reduction in cases of shoulder dystocia (SD). The simulation environment consisted of a fetal model fitted with a number of sensors, a rudimentary model of a maternal pelvis and a tactile sensing glove as shown in Figure 40. This setup allowed for both a viable evaluation tool and a training scenario, albeit a very specialised one.

Figure 40: Shoulder Dystocia force reduction simulator schematic. Source: [23]

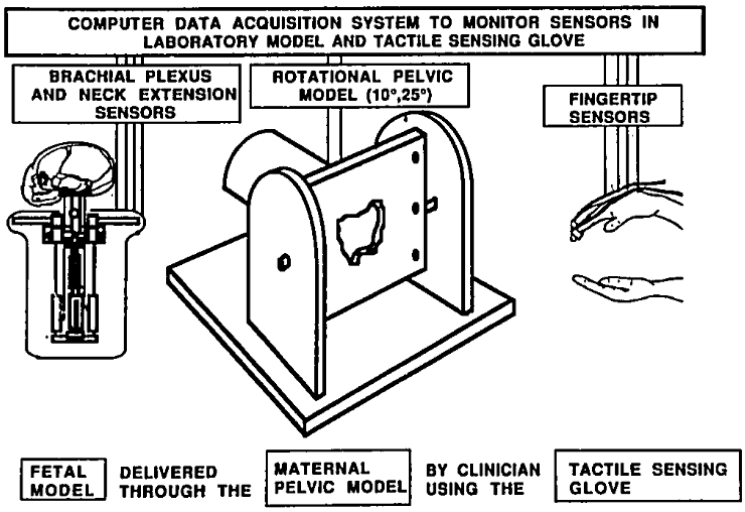

Details of a different hybrid simulator were published in 1995 by R. H. Allen et al. [24]. The simulation environment was very specialised to solve a specific problem which in this case was to determine the clinician's applied loads on the newborn, as shown in Figure 41. The simulator provides a computer interface capable of determining a number of different forces applied by a clinician as shown in Figure 42 with the use of multiple strain gauges. The simulation environment was then tested by 14 clinicians who performed a set of scenarios ranging from standard delivery to an incidence of SD. The resulting information may prove to be very useful if a future project had to consider any externally applied forces.

This simulator described by Gonik et al. [24] was further developed by McDonald et al., details of which were published in 2005 [25]. The system had been considerably improved with the use of new fetal and maternal models as shown in Figure 43. This setup allows for greater realism and accuracy of the forces applied by a clinician during a real delivery. The added realism of the models also makes it more viable as a training tool rather than just a laboratory experiment.

In 2004 a new approach at creating a hybrid birth simulator was described

Figure 41: Simulator example. Source: [24]

Figure 42: Forces tested. Source: [24]

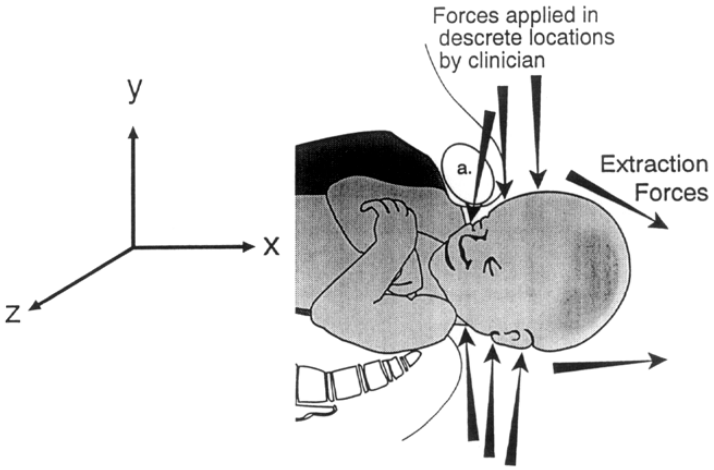

Figure 43: Improved biofidelic birthing simulator. Source: [25]

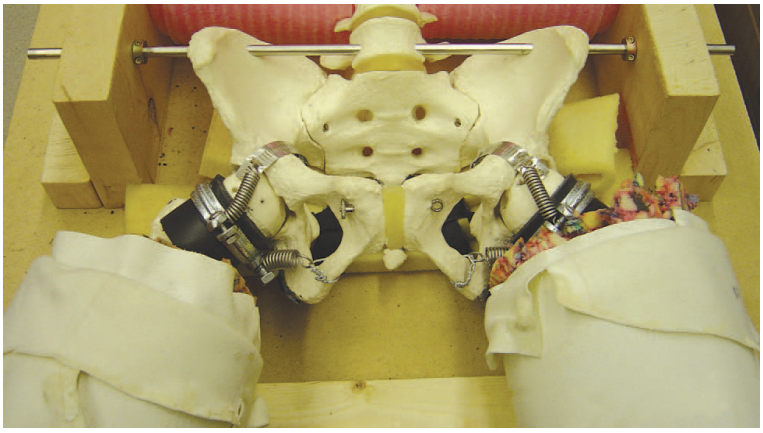

Figure 44: BirthSIM. Source: [26]

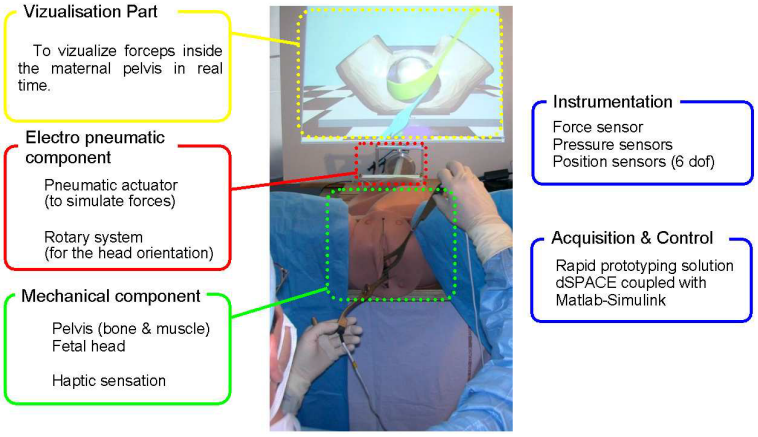

by R. Silveira et al. [26]. The approach was to create a complex mechanical maternal abdomen model that would also have a virtual representation. As the main purpose of the simulation was to train clinicians in forceps blade placement, the fetus only had a head representation. The movement of the forceps blades was tracked in real-time which corresponded to a set of virtual blades within a virtual environment (Figure 44).

The system interface was developed further by O. Dupuis et al. and described in a 2006 publication [27]. The tracking of the forceps blades allows the simulation environment to give a visual representation of the paths taken (Figure

Figure 45: Blade motion tracking in BirthSIM. The tracelines shown inthe graph represent the displacement of both forceps blades along the X, Y and Z axis in the case of an Occiput Anterior head presentation at a station evaluation of +5. Each axis in the graph represents the displacement in cm along the stated axis. Colours represent motion performed by different operators. Adapted for clarity from: [27]

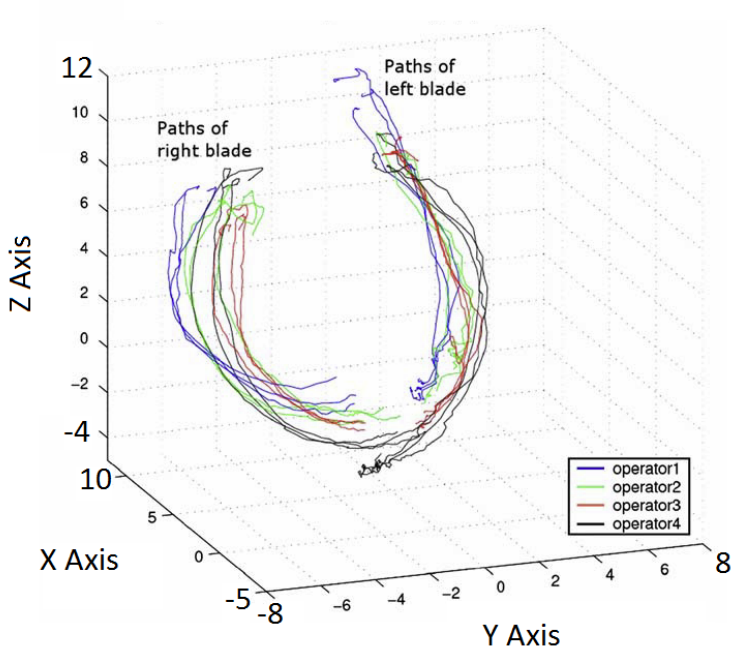

45) which can then be analysed by the clinician who undertook the task. The pressure at which the fetal head is pulled is also recorded providing an important dataset which can be used in additional training and in future projects.

An alternative method of forceps simulation can be seen in a paper published by R. J. Lapeer et al. in 2004 [28]. The system consists of a virtual fetal model extracted from MRI data of a stillborn fetus. The system then uses an optical tracking interface to position the virtual fetus in relation to the real obstetric blades as shown in Figure 46. This is a novel approach to forceps simulation as motion tracked augmented reality had not yet been implemented for this problem domain. The nature of the simulation means that haptic feedback would be limited in regards to any resistance a clinician would experience by pulling on a

Figure 46: Virtual forceps simulation. Source: [28]

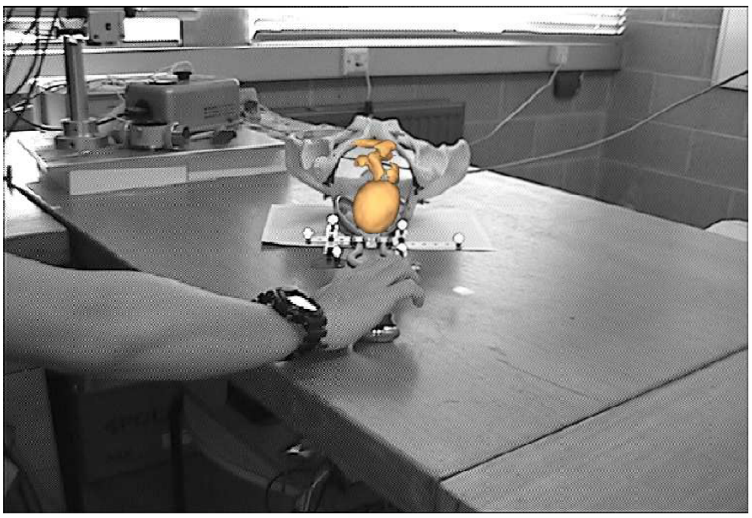

fetal head during a delivery.

An interesting approach to a haptics enabled birth simulator was published by A. F. Abate et al. in 2010 [29]. Although the simulation environment itself is basic when compared to some of the other virtual simulators described earlier, the way a user can interact with it is novel. Unlike many of the virtual simulators in the previous section, this system makes use of two exoskeletons for the arms and a virtual reality visor as shown in Figure 47. This approach allows for direct interaction with the virtual environment and makes this a feasible alternative to fully mechanical training simulators. There are some drawbacks however; the fidelity of the exoskeleton is minimal and has high cost implications.

2.3.5 Investigating the effect of obstetric forceps on the fetal head

Lapeer et al. [61] investigated the effect on the fetal head of incorrectly (asymmetrically) placed forceps using a static FE model. They found that the degree of deformation of the fetal skull bones and fontanelles and the shear stress induced in fragile parts of the fetal skull were substantially (and dangerously) higher when forceps blades were placed asymmetrically as compared to symmetric, cor-

Figure 47: Virtual training exoskeleton. Source: [29]

rect placement. Su et al. [97] also investigated the effect of forceps on the fetal head but focussed their study on the effect of the materials and shape of the forceps blades with the expectation of designing better instruments to reduce the stress on the newborn's head and pressure on its neck.

3 Software Tools Development

The complicated process of modelling and simulating various aspects of labour and the instrumental interventions that this study focussed on required the development of software based solutions. The main issues that had to be addressed by the software were:

1. Geometry of the anatomical components, i.e. fetal skull, maternal pelvis, obstetric forceps and ventouse cup.

2. Determine/set the position of the fetal head/skull in the maternal pelvis.

3. Apply forceps blades and a vacuum extraction suction cup to the fetal skull to determine the contact pressures and forces involved.

The information regarding the application of forceps and the VE suction cup will be covered in Chapter 5.

3.1 Model Geometry

Following the extensive review of various literature (much of which has been described in Chapter 2) and investigations in to the medical aspects of childbirth, it was concluded that in order to correctly set up the experiments for analysing the impact of instrumental interventions on the fetal skull, the following geometric models were required:

- Maternal pelvis
- Fetal skull/head
- Forceps
- Vacuum extraction suction cup

Figure 48: Volume rendered CT scans of the abdomen and pelvis of the Visible Female [30]

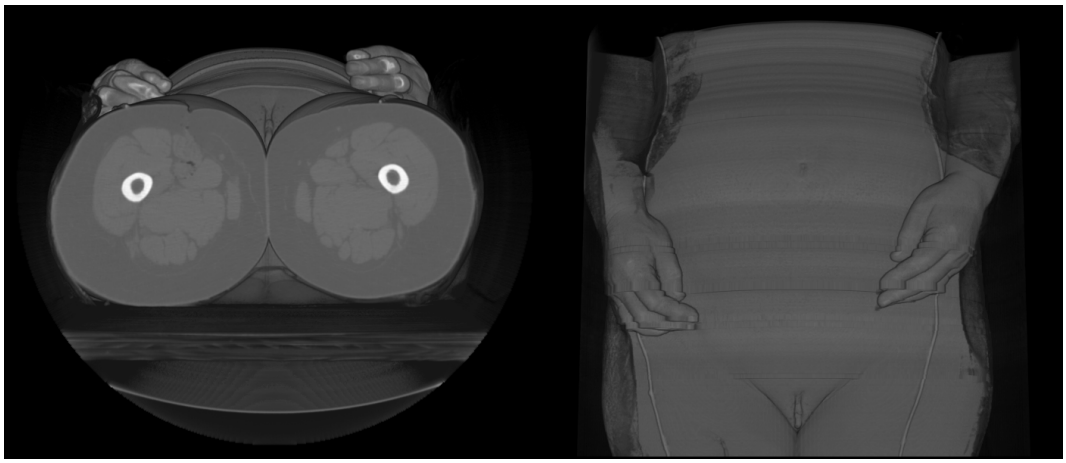

3.1.1 Maternal Pelvis

An initial model of the maternal pelvis was developed using CT scan data by Audinis [98]. The process was as follows:

Data extraction from a CT scan meant that the resulting pelvic model would be of high fidelity and would therefore be suitable for various uses in simulating birth related processes, examinations and interventions. Scan data was obtained from the Visible Female (VF) of the Visible Human Project [30] and reconstructed in volumetric form with the use of the 3DView software [28] developed at the UEA. The extraction occurred in the following set of steps:

- Combine relevant CT scan slices into a 3D volumetric representation, as shown in Figure 48.

- Perform grayscale based thresholding to expose bone information. This is achieved by applying an alpha value on anything outside of a specified grayscale range, as shown in Figure 49.

- Using the marching cubes algorithm [31], triangulate any visible bones to form a mesh based object. Once again, this process uses a specified

Figure 49: Thresholded Visible Female data to expose the bony pelvis.

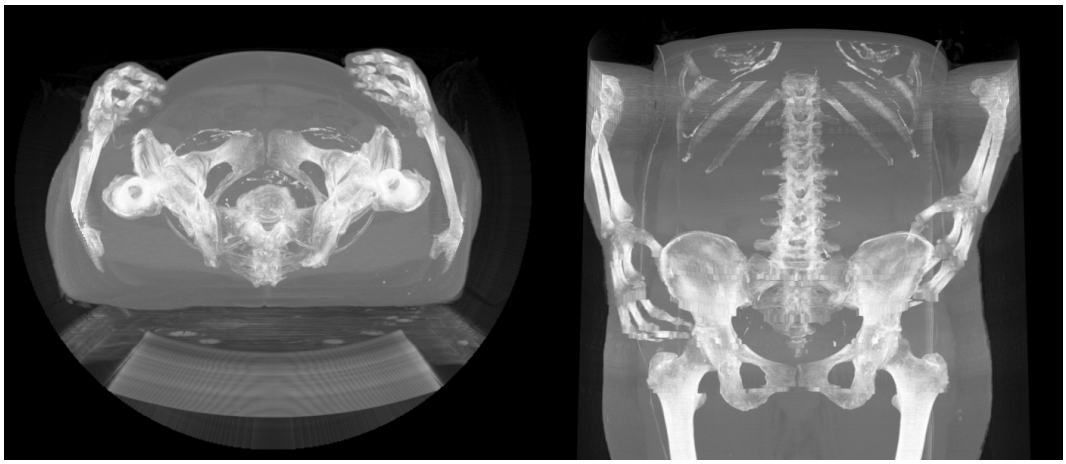

Figure 50: Extracted surface of the volumetric data shown in Figure 49 after using the marching cubes algorithm [31].

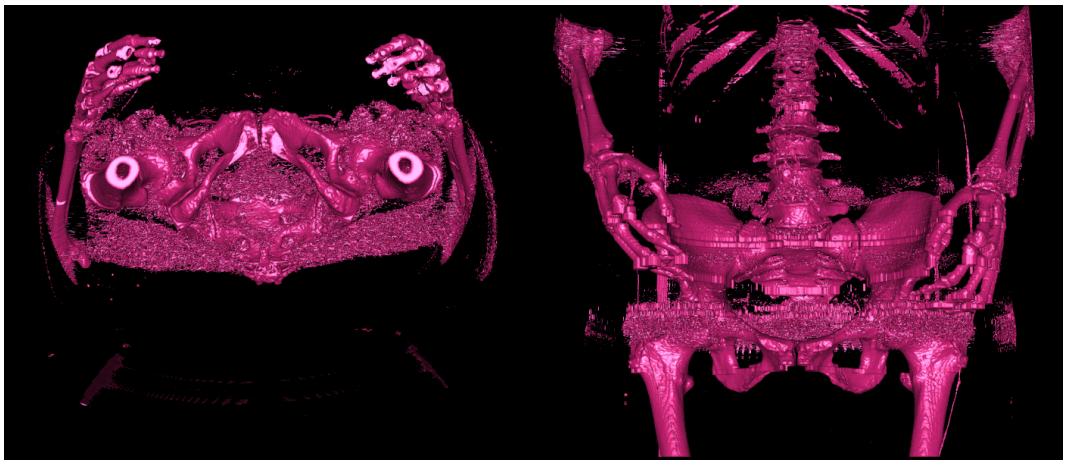

grayscale range to which the triangulation algorithm is applied, producing a mesh based model ready for alterations/post processing, as shown in Figure 50.

- The next step involves the use of a mesh editing software, e.g. 3D Studio Max [99], to remove any unwanted geometry due to parts in the CT data that have the same grayscale range as bone.

Figure 51: Geometric surface model of the maternal pelvis following initial noise removal.

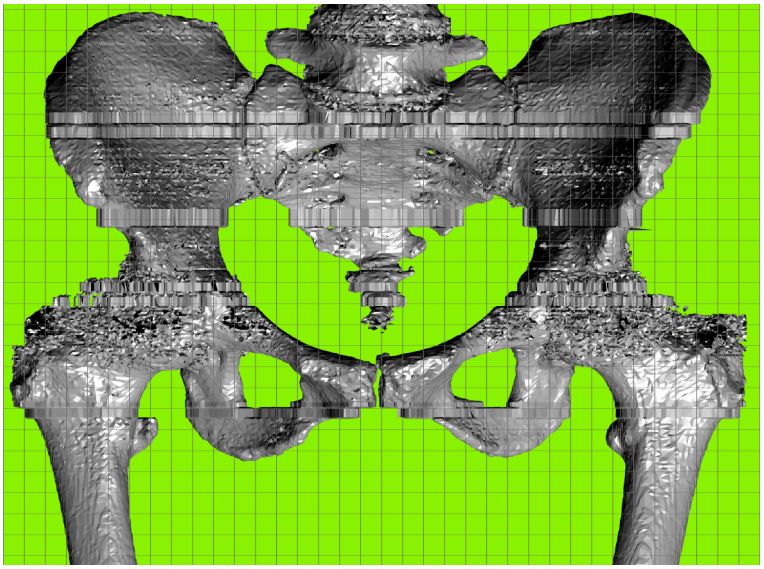

- Further mesh artifact removal and general mesh repair. The need for this step comes from the fact that a volumetric representation of the initial scan data means that not just the bone surface was triangulated, but the inside parts too. Additionally, some parts were missed because of grayscale values that were outside of the given 'bone' range when trying to extract the bone information in previous steps and therefore produced holes - see Figures 52 and 53.

- The final step involves optimising the mesh triangle count by collapsing triangles. The initial count of polygons at the start of the process was over 3M which was down to just above 64,000 once finished as shown in Figure 54. This was later adjusted further if and when required.

3.1.2 Fetal Skull

The original skull model was developed by Lapeer [19]. Here it is simplified in terms of polygon count and then optimised in terms of triangle aspect ratio. The

Figure 52: Meshed part with incorrect hole (left) and after correction (right).

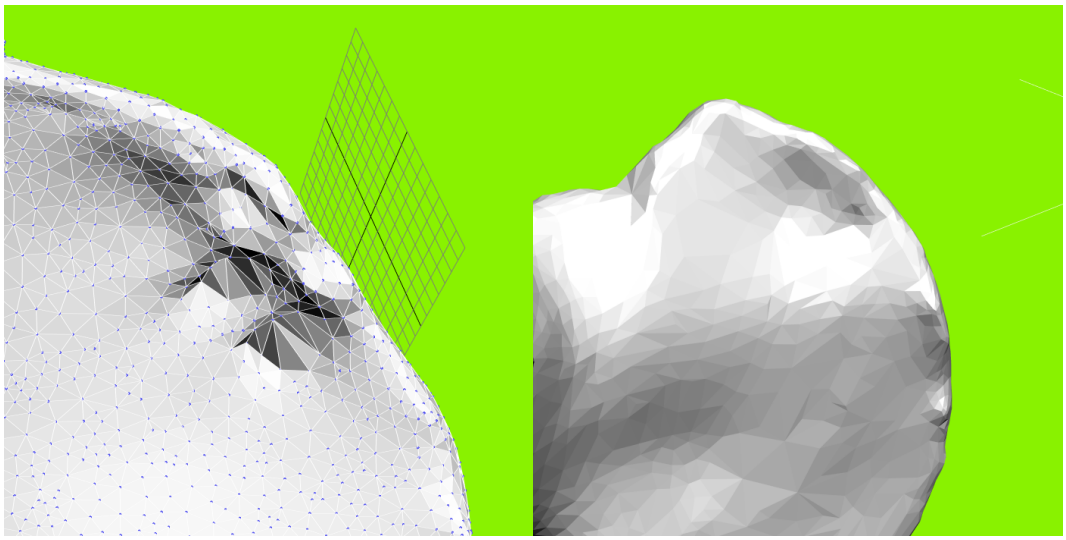

Figure 53: Meshed part with incorrect hole and noise (left) and after correction (right).

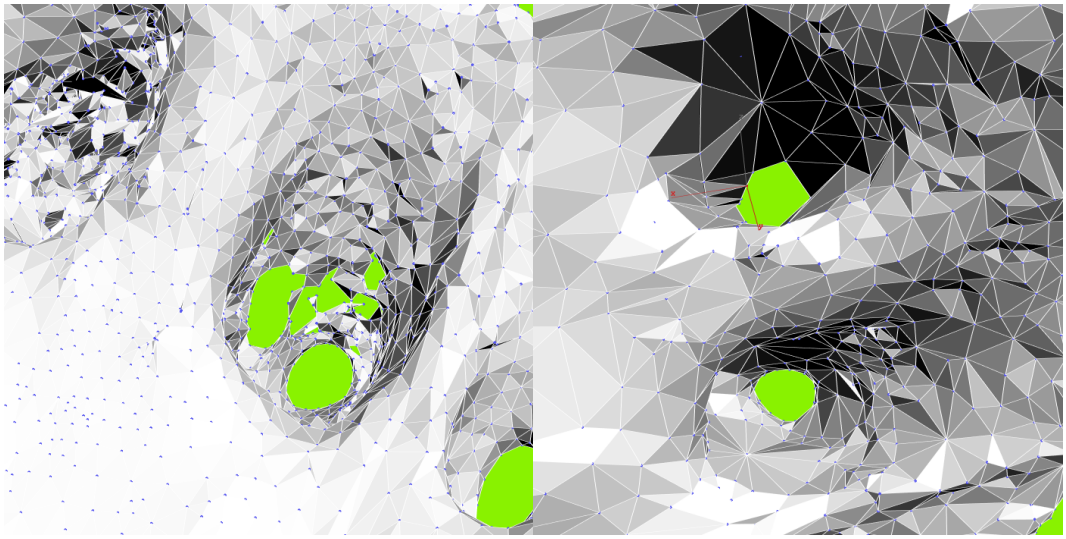

Figure 54: Final mesh models of the maternal pelvis. Left; 3M triangles : Right; 64,000 triangles.

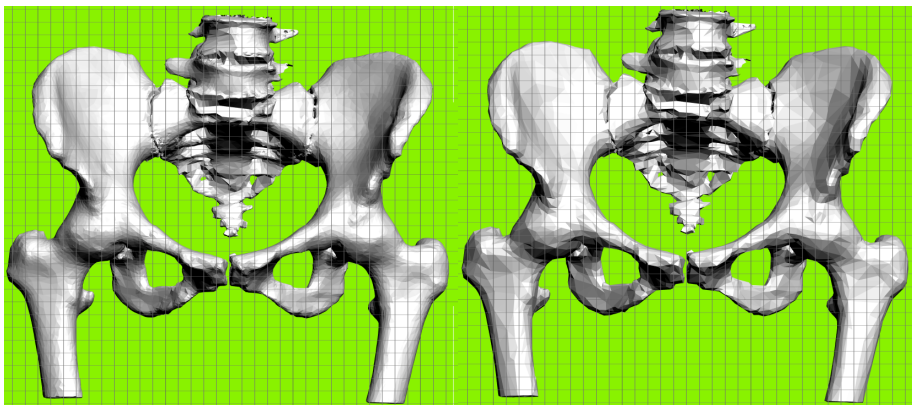

former is necessary to keep the processing time at interactive speeds for setting up the instrumental experiments (see Chapter 5). Figure 55.

3.2 Collision Detection

Due to the nature of the problem domain, there was a need to develop a very robust collision detection engine. This engine includes various approaches to collision detection;

- Axis Aligned Bounding Boxes (AABB).
- Separating axis theorem (SAT).
- Euclidean distance testing.
- Normal based exclusion.
- Triangle-Triangle detection (Tri-Tri).
- Further optimisation.

Figure 55: Left; Fetal skull model by Lapeer (~64,000 triangles). Right; Decimated and optimised skull model (~7,000 triangles).

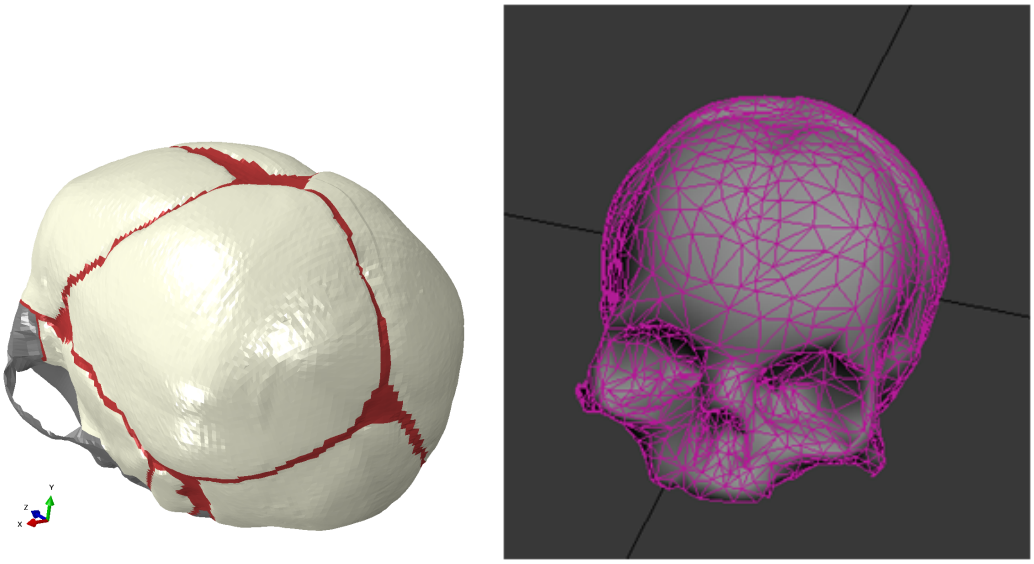

3.2.1 Axis Aligned Bounding Boxes

The geometric models developed and used in this thesis contain many triangles. This has a couple of implications:

- Many triangles mean high fidelity of a model and a close approximation of the real world topology that is being modelled.
- More triangles means more individual triangle to triangle interactions when there are multiple models in the current scene.

It is possible to just check all triangle instances of two models against each other but this would be very slow for all but models containing only a few triangles. This issue is essentially that of a problem domain being too large so to address this the problem domain must be minimised. This was achieved using AABBs. An AABB is simply a virtual bounding volume (a box) which encompasses all (or a subset of) elements of a given geometric model. The minimum and maximum points of the initial "root" AABB node would be the minima and maxima of

Figure 56: Binary-tree based AABB construction.

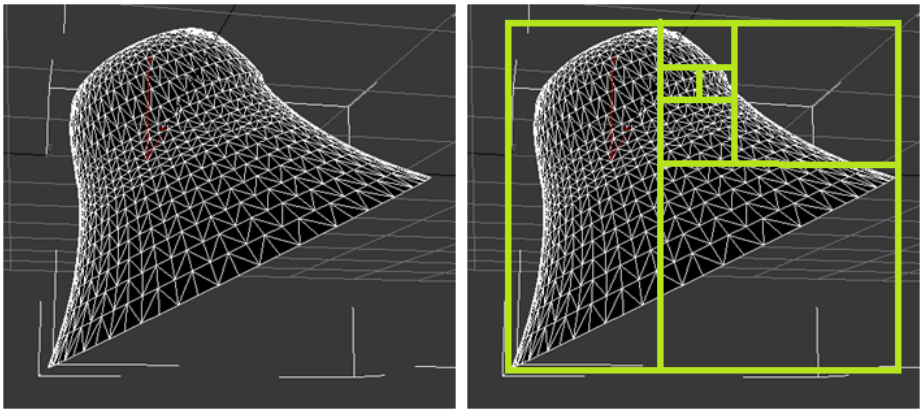

the triangle coordinates that make up the model. These are found by a pre-processing step which checks all model triangles once and updates minima and maxima for the bounding volume.

Once the bounding root volume has been calculated, the root AABB can be broken down into smaller chunks which all encompass an increasingly smaller subset of the model elements. For this thesis a binary-tree method was initially used as shown in Figure 56 (bounding boxes were split in half along either the x, y or z-axis), but was later adapted to an octree (split into 8 sections) to decrease the AABB tree depth. The resulting AABB tree is shown in Figure 57.

3.2.2 Separating axis theorem

Now that the problem domain has been compartmentalised with the use of bounding volumes, it is time to narrow down which element subsets may potentially collide. Separating Axis Theorem (SAT) is a fast generic method for analysing whether two convex shapes are intersecting.

In simple terms, the definition of the SAT algorithm can be stated as: for a pair of non intersecting polytopes, there exists at least one axis upon which the projection of the polytopes will not overlap [100]. Using this method requires

Figure 57: An example of AABB tree on a geometric pelvis model. The bigger bounding volumes represent larger element counts within each bounding volume.

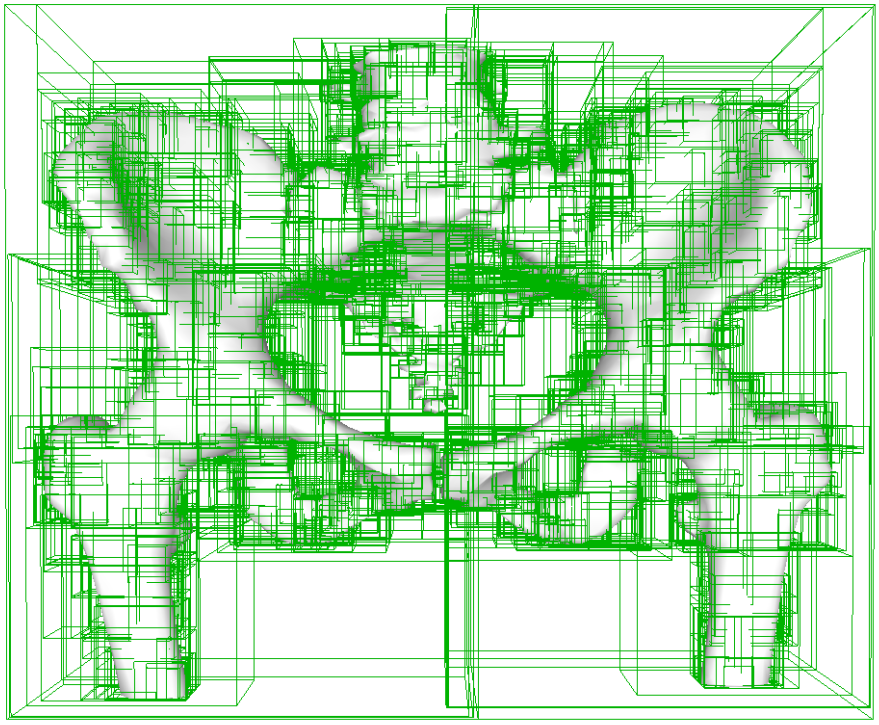

Figure 58: Example of Separating Axis Theorem; No collision with 2 seperating axes.

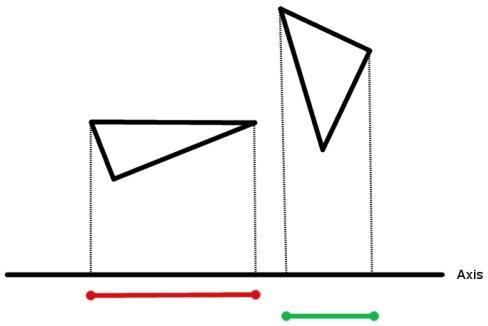

Figure 59: Example of Separating Axis Theorem; No collision with 1 seperating axis.

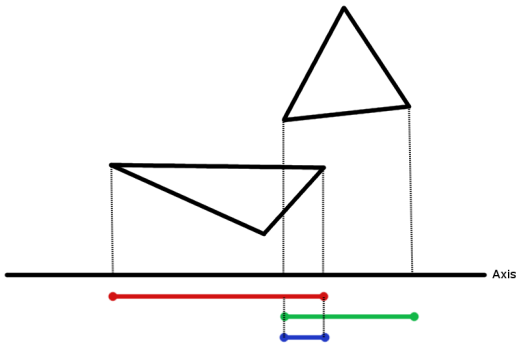

the simplification of the 3D space to a set of three 2D projections on the x, y and z axes respectively. An example is shown in Figures 58 and 59.

3.2.3 Euclidean distance testing

The use of bounding boxes provides a smaller subset of triangle elements that need to be tested but a direct tri-tri testing even with a reduced subset still has the potential to be relatively slow. An additional optimisation to mitigate this issue is the use of Euclidean distance testing between the centre points of

2 triangles. The criterion of excluding two triangles of potentially colliding is based on the Euclidean distance D_e in a 3D space given two points (x_1, y_1, z_1) and (x_2, y_2, z_2) and is given by:

$$D_e = \sqrt{(x_2 - x_1)^2 + (y_2 - y_1)^2 + (z_2 - z_1)^2} > D_{ref} \tag{1}$$

where D_{ref} is 2 times the largest center-to-edge distance of any triangle within a given mesh. In order to make the best use of this optimisation, the triangle mesh elements should all be relatively uniform in size. If this is not the case, some elements may be evaluated as colliding meaning that other, more computationally expensive stages, may have additional elements to test. Conversely and worse, potentially colliding triangles may have been excluded hence missing a collision. Because the models in this study do not contain uniformly sized elements, with uniformly sized edges, a further scaling factor >1 on D_{ref} is used to decide if a potential collision should be investigated further.

3.2.4 Normal based exclusion

In order to optimise the collision detection further, a normal vector direction comparison method was implemented. The method discounts any triangles, which are facing in the wrong direction (to a predetermined range and error metric) and thus cannot collide, but would normally undergo tri-tri collision testing due to their proximity to each other.

3.2.5 Tri-Tri intersection detection

The field of collision detection is well established and there are a number of algorithms that have been developed to find intersections between two triangles. Some of the fastest and most established of these algorithms are:

- Tomas Möller - A fast triangle-triangle intersection test [100]
- Guigue and Devillers - Fast and robust triangle-triangle overlap test using orientation predicates [101]
- Tropp et al. - A fast triangle to triangle intersection test for collision detection [102]

To address the needs of this study, Thomas Möller's Tri-Tri intersection with no division operation test was chosen. The steps of the algorithm are described in detail in Möller's paper [100], and in summary as outlined by Möller, the algorithm is as follows:

1. Compute plane equation of triangle 2
2. Reject as trivial if all vertices of triangle 1 are on the same side
3. Compute plane equation of triangle 1
4. Reject as trivial if all vertices of triangle 2 are on the same side
5. Compute intersection line and project onto largest axis
6. Compute the intervals for each triangle
7. Intersect the intervals

Applying this method of collision detection to the suite of the other tests outlined in this section allowed for real-time interaction between multiple geometric models. An example of the proposed collision detection engine in use is demonstrated by Figure 60.

Figure 60: Collision detection between a model of a pelvis and fetal skull using the proposed collision detection engine. Top; AABB tests of skull and pelvis. Middle; Colliding AABBs of skull and pelvis respectively. Bottom; Tri-Tri collisions between skull and pelvis.

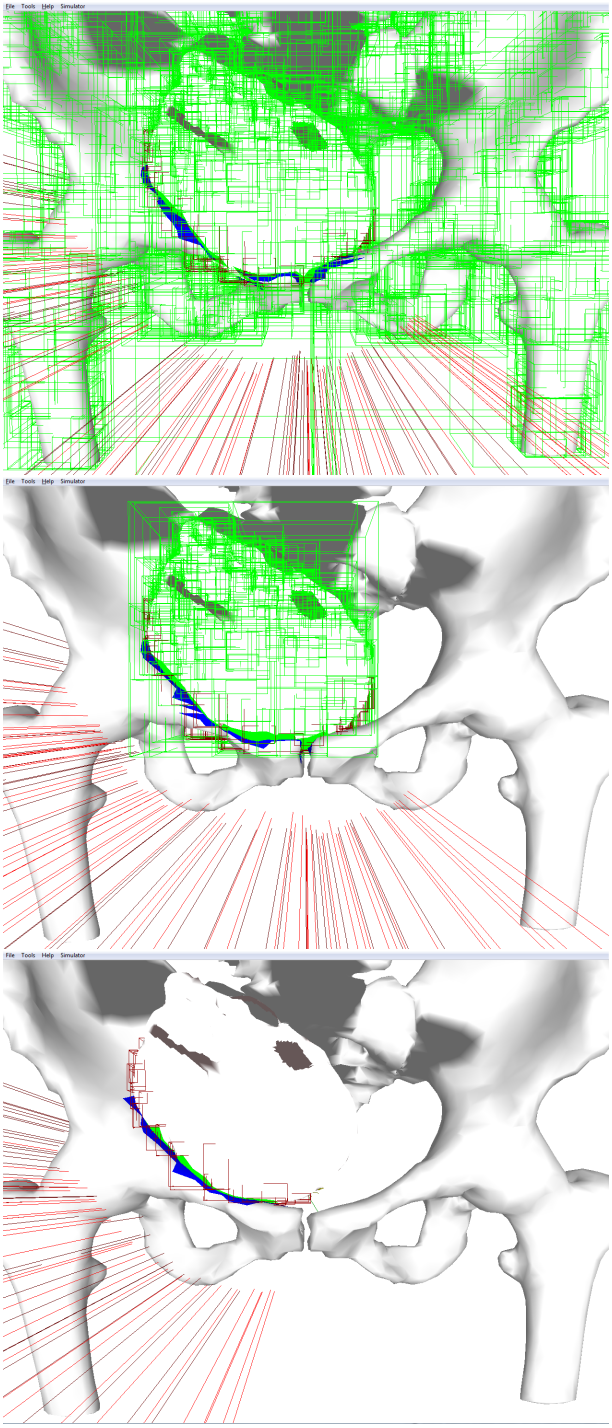

3.2.6 Further optimisation - a heuristic method for bounding volume tree creation

To further improve performance of the collision detection engine, a heuristic approach to AABB tree creation was developed. This heuristic method would adjust the creation process of the tree based on a number of specified conditions:

Parameters

The following parameters are used:

- Maximum depth of tree - this is the overriding condition which ensures that the depth of the tree does not exceed the specified value.
- Minimum number of triangles per tree leaf node - if the specified maximum tree depth has not been reached then check whether the current number of bounded triangles is not below a given value. This limit is imposed to ensure that the situation would not arise where there would be only a very small number of triangles per leaf node. Otherwise the advantages of AABB would be lost.
- Preferred number of triangles per tree leaf node - this value specifies the point at which the leaf node should be considered to be fully populated with its bounded elements. Unlike the previous conditions, this one is a guideline and will be dictated by the limitations imposed by those conditions.
- Acceptable deviation - preferred deviation for the number of elements a leaf node should hold. This directly relates to the previously outlined condition. If the preferred triangle count is set to 20 and the current number of triangles left to capture is 25, given an acceptable deviation of 6, the node will capture the set of 25 triangles. If the acceptable deviation

was 4 however, the algorithm would attempt a further split of the node unless the minimum triangle count was too high.

Experimental validation - experiments

The outlined heuristic method was then used to determine the optimal settings to obtain the best performance for a given simulation scene. This was achieved by repeating a set of simulations where a skull model comes into contact with a pelvic model. For each attempt the skull followed the exact same path for the same amount of time. The only change for each run would be one of the values within the heuristic parameters outlined above. The scenes were also tested on models with various degrees of mesh resolution to see whether the best heuristic definition for a lower quality model would still produce the best results for a model with more triangles.

Figures 61 - 66 show the framerate in frames rendered per second (FPS) when variations in maximum tree depth and minimum triangle count were altered. The collision detection tests during this analysis only included SAT and Tri-Tri, and were performed on a single thread. Note that the maximum framerate is typically observed at the start of the collision between skull and pelvis whilst the minimum framerate is observed at maximum contact between the models.

Experimental validation - discussion

From Figures 61 - 66 we observe that the optimum configuration ranges for all instances, apart from the 38,000 triangle test, were :

- Maximum tree depth of 10 - 12
- Minimum triangle count of 15 - 20

Figure 61: Top; Max framerate (FPS). Bottom; Min framerate (FPS) output when an approximately 7,000 triangle pelvis collides with a 7,000 triangle sphere model with variations in max tree depth and min triangle count.

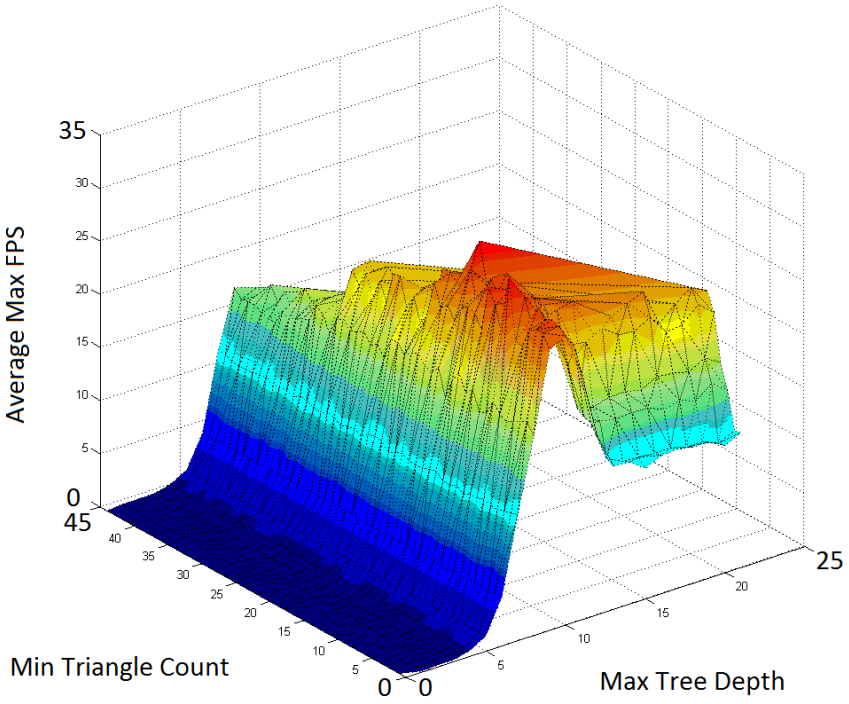

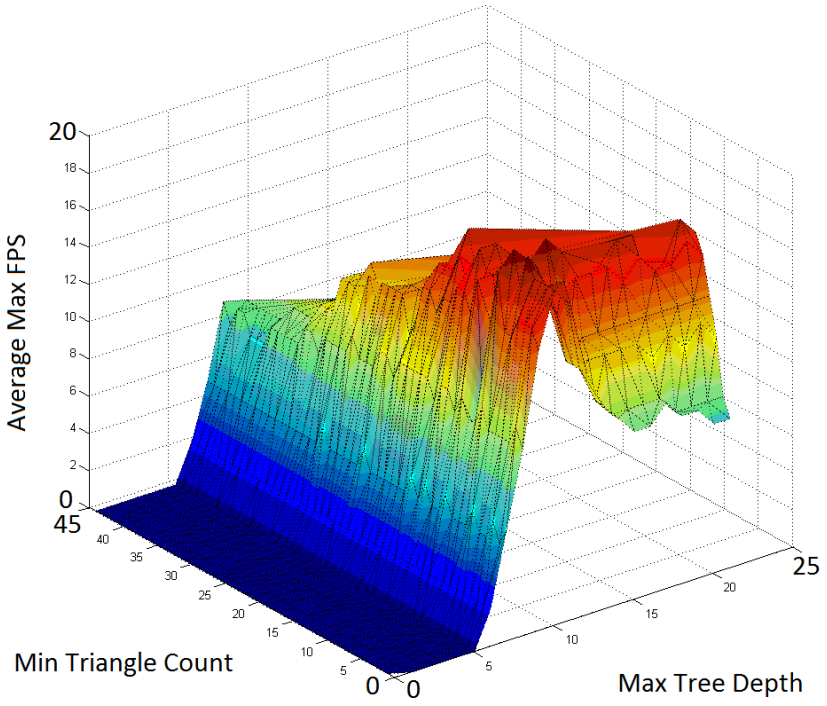

Figure 62: Top; Max framerate (FPS). Bottom; Min framerate (FPS) output when an approximately 9,000 triangle pelvis collides with a 7,000 triangle sphere model with variations in max tree depth and min triangle count.

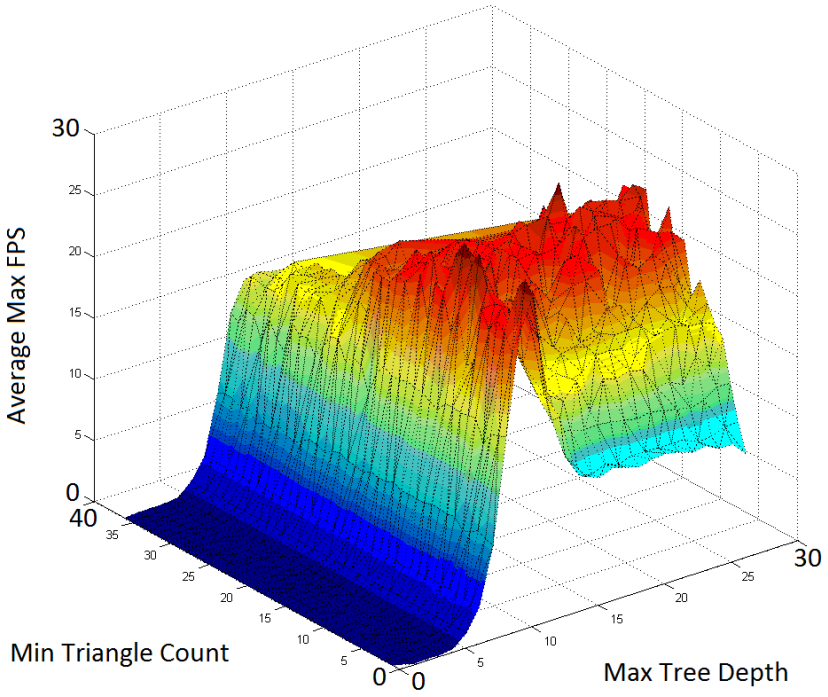

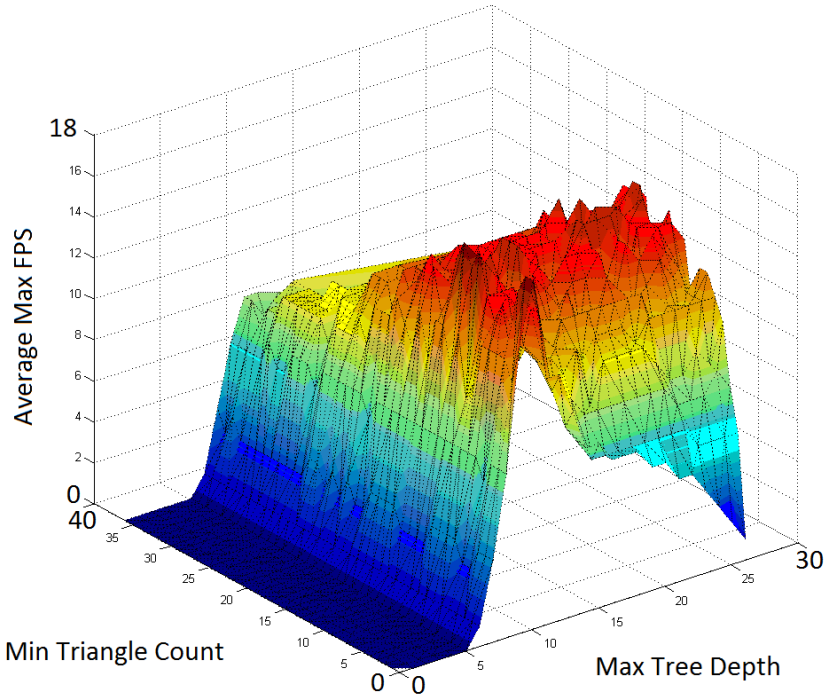

Figure 63: Top; Max framerate (FPS). Bottom; Min framerate (FPS) output when an approximately 13,000 triangle pelvis collides with a 7,000 triangle sphere model with variations in max tree depth and min triangle count.

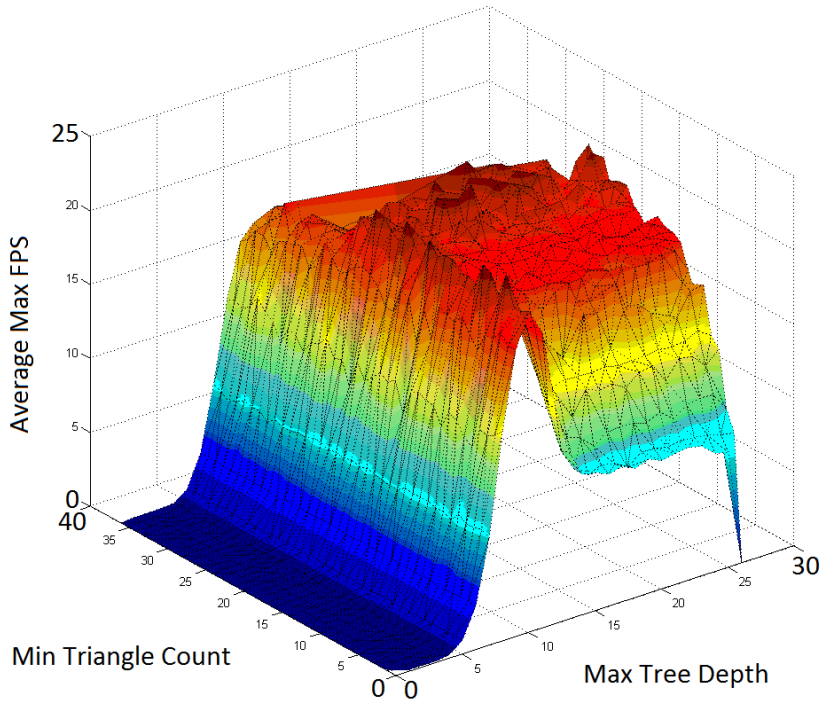

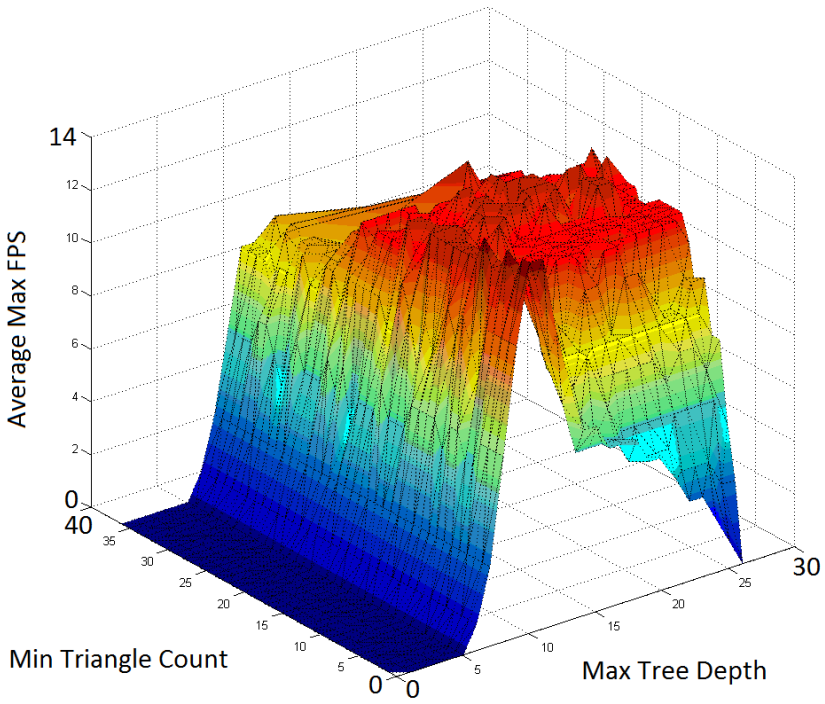

Figure 64: Top; Max framerate (FPS). Bottom; Min framerate (FPS) output when an approximately 15,000 triangle pelvis collides with a 7,000 triangle sphere model with variations in max tree depth and min triangle count.

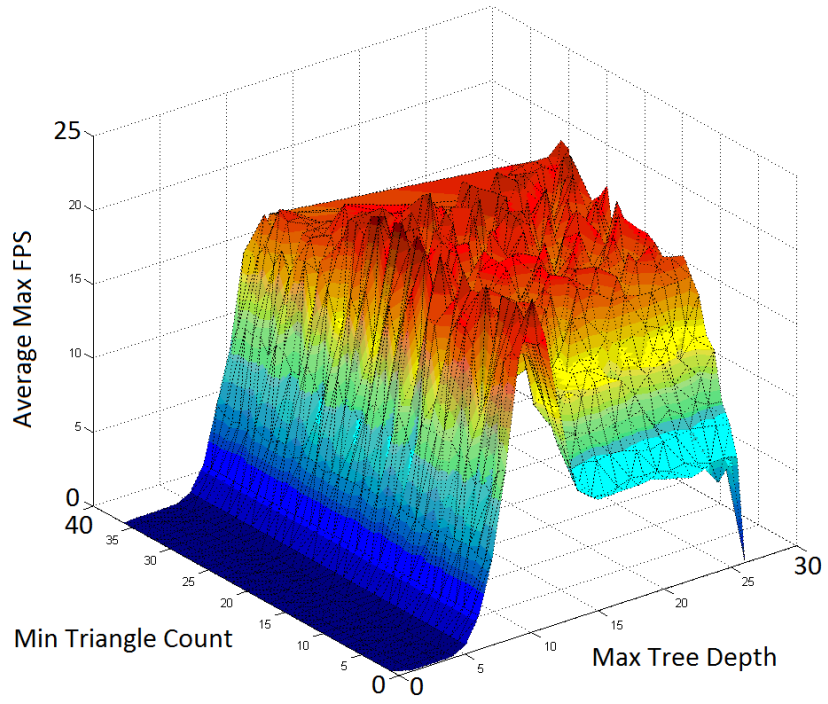

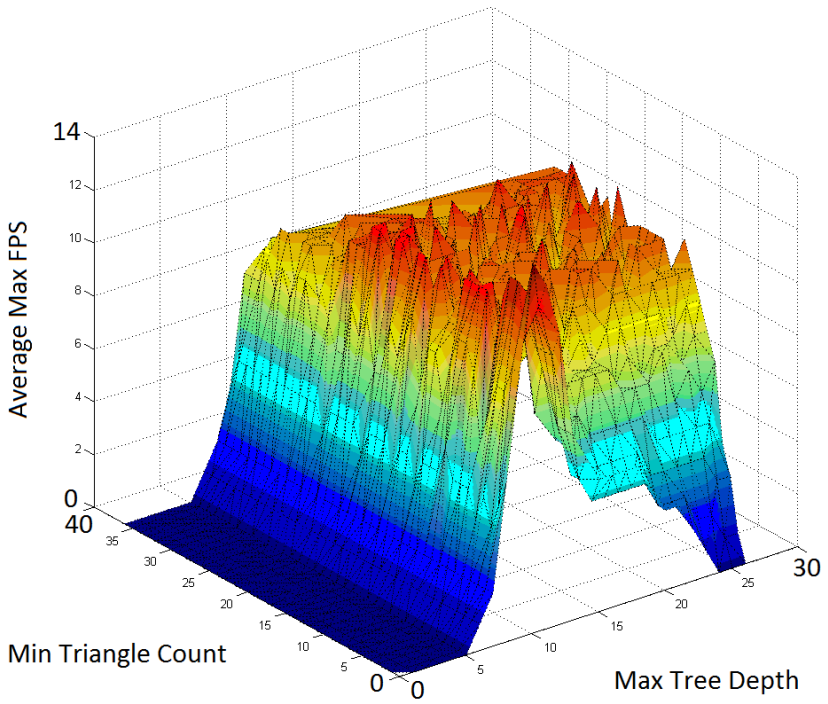

Figure 65: Top; Max framerate (FPS). Bottom; Min framerate (FPS) output when an approximately 27,000 triangle pelvis collides with a 7,000 triangle sphere model with variations in max tree depth and min triangle count.

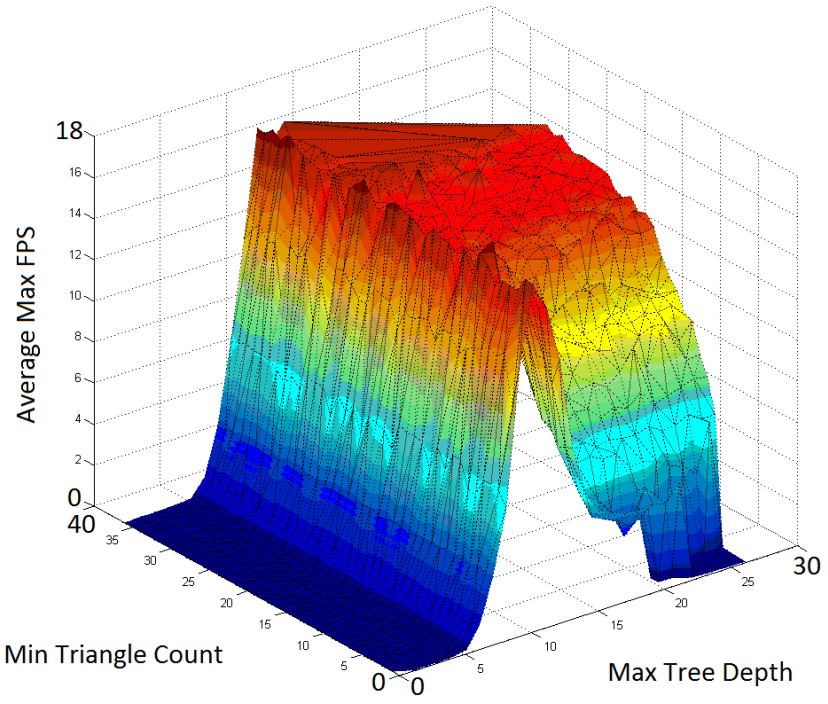

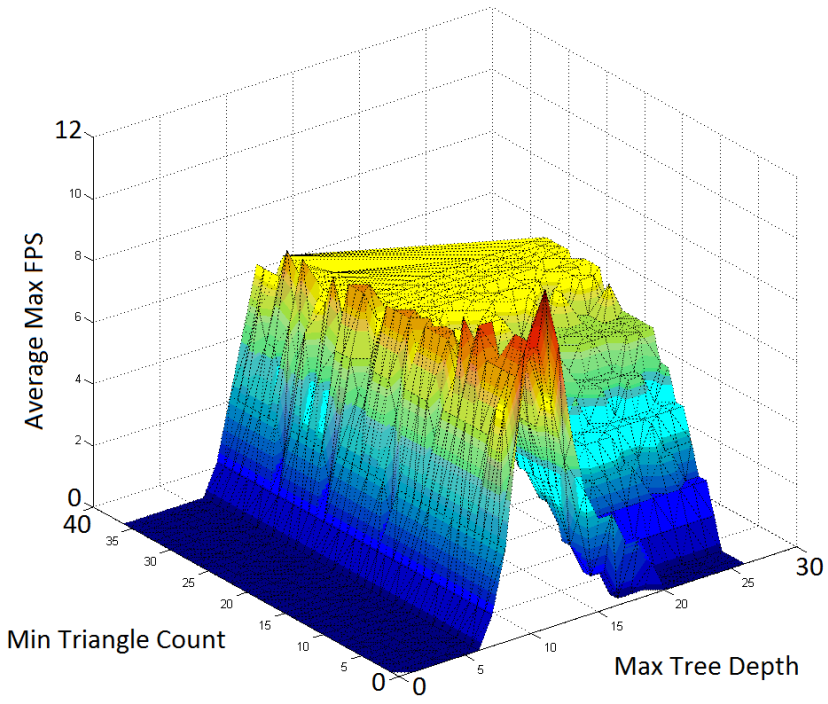

Figure 66: Top; Max framerate (FPS). Bottom; Min framerate (FPS) output when an approximately 38,000 triangle pelvis collides with a 7,000 triangle sphere model with variations in max tree depth and min triangle count.

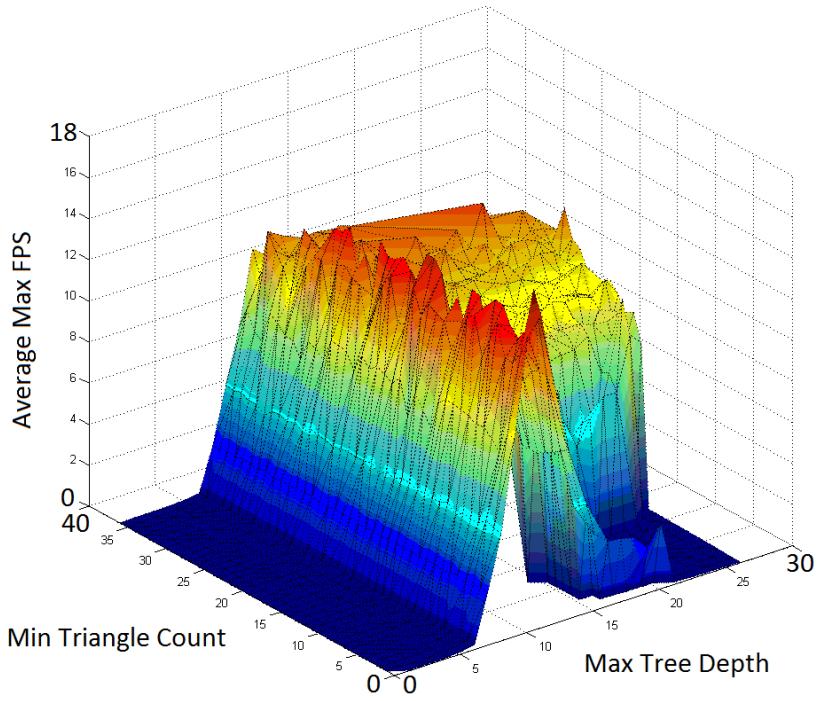

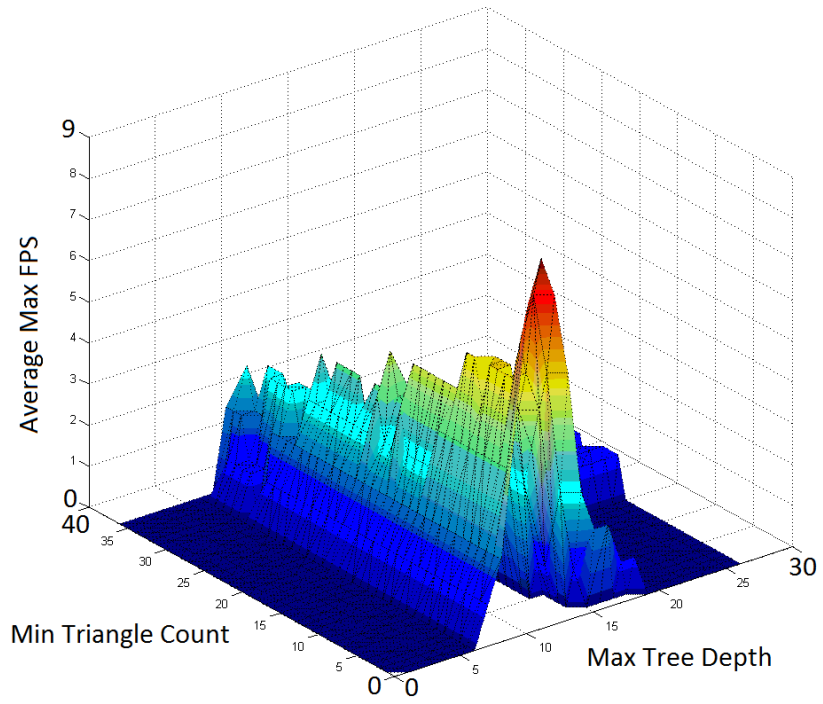

For the 38,000 triangle test the highest minimum (inf) framerate (FPS) was observed when the min. triangle count was in the range of 1-5.

This configuration produced the highest max. framerate (FPS) output and in most cases also the highest min. framerate (FPS).

Even though the 38,000 triangle model (and to some extent, the 27,000 triangle model) has better min. framerates (FPS) values at lower min. triangle count settings, its max. framerate (FPS) corresponds to similar min. triangle counts as those obtained from the other configurations. The reason for this optimal range seems to be a tradeoff between having to traverse down the levels of the tree whilst performing SAT tests at each level and the amount of time it takes to perform Tri-Tri tests once a leaf node has been reached.

3.2.7 Multiple collision detection threads

In order to further improve the performance, the process outlined above was then altered to run on multiple threads. This allowed for a gain in performance sufficient enough to allow for real-time interaction (considered to be >30 FPS) with models with much more than 30 thousand triangles.

3.3 Collision Response

Once collisions have been tested for and determined, the system required for an implementation of a response algorithm. The current implementation is based on two main complementary principles:

1. Interpenetration based repulsion.

2. Force based repulsion.

The combined approach allows the simulation to function based on the forces of interest and only worry about interpenetration when it needs to.

3.3.1 Interpenetration based repulsion

Interpenetration testing provides a rudimentary way of controlling response within a simulation scene. The nature of interpenetration means that this event does not truly happen in real life scenarios. To take this fact into account, interpenetration needs to be avoided. This is achieved by adopting a set of hierarchical rules:

- If interpenetration has occurred within the current time-step, adjust the scene until no more interpenetration is detected. During this event, all other forces are considered null to allow the fastest possible correction time. The adjustment vector and its magnitude are based on the number of penetrations and their depth.

- If interpenetration is going to occur within the next amount of predefined time-steps, alter the velocity vector of the incoming object. This alteration will allow the object to continue moving in its current direction but will ensure that it will slow down or stop before any interpenetration happens.

3.3.2 Force based repulsion

All objects within a given simulation scene can be affected by a large number of different forces which will dictate any movement before and after a collision has taken place. The simulator considers these by examining the movement vector direction and magnitude between any colliding objects. Material properties are then taken into consideration before a reaction force is calculated based on the number of impact points. The grouped size of the point area is also considered, this allows the simulation to react to multiple zones of impact at any one given time.

3.4 Fetal head presentation

Using the methods and models outlined in this Chapter an additional tool was developed to help determine and assess the fetal head station and orientation through palpation. As will become apparent from further explanation in the next Chapter knowing the orientation of the fetal head is very important if forceps or VE are to be used. This work which was undertaken by Audinis is described in detail in Appendix B.

4 Fetal head moulding: A new model

The research presented in this chapter follows on from the original research by Lapeer [19, 96] who developed a realistic model of fetal head moulding. The aim of the work presented in this thesis is to further improve this model in terms of speed and convergence, realism and accuracy. The underlying concepts of the various stages of the childbirth process were already discussed in Section 2.1 but the anatomy of the fetal head must also be outlined before a detailed account of these improvements can be provided.

4.1 The fetal head

Like any human head, the head of the fetus consists of many complex anatomical parts and fluids. The purpose of this section is to discuss those parts that are relevant to this study. Soft tissues such as skin and muscles which surround the fetal skull are beyond the scope of this study and will not be discussed. The following parts are considered:

- The fetal skull bones
- The fontanelles, sutures and dura mater
- Cerebrospinal fluid and blood flow

4.1.1 The fetal skull bones

The fetal skull bones are thin, single layered sections of bone which lay atop of a dura mater layer as shown in Figure 67. Unlike the ossified three-layered bone in an adult skull, these bones have not yet developed a spongy layer in the center making them less rigid and allowing some degree of flexion to be exhibited under

Figure 67: An exposed fetal skull with a lifted up parietal bone.

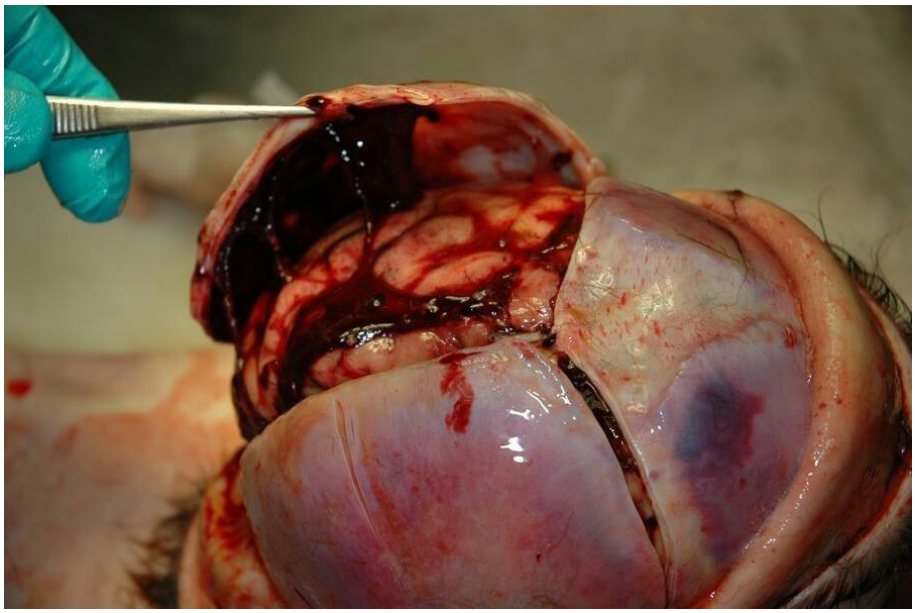

load. Fetal skull bones exhibit orthotropic material properties. The cranial bone sections (which are also outline in Figure 68) are:

- Frontal bone
- Parietal bone
- Occipital bone
- Sphenoid bone
- Temporal bone

4.1.2 Fontanelles, sutures and dura mater

The fontanelles and sutures are shown in Figure 68 as the red coloured sections. They exhibit the same material properties as the dura mater which connects to the outermost layer of the meninges which cover the brain and spinal cord. Figure 69 shows the largest 'anterior' fontanelle from an autopsy.

Figure 68: Fetal skull sections. Colours represent different material properties which are described in Figure 70.

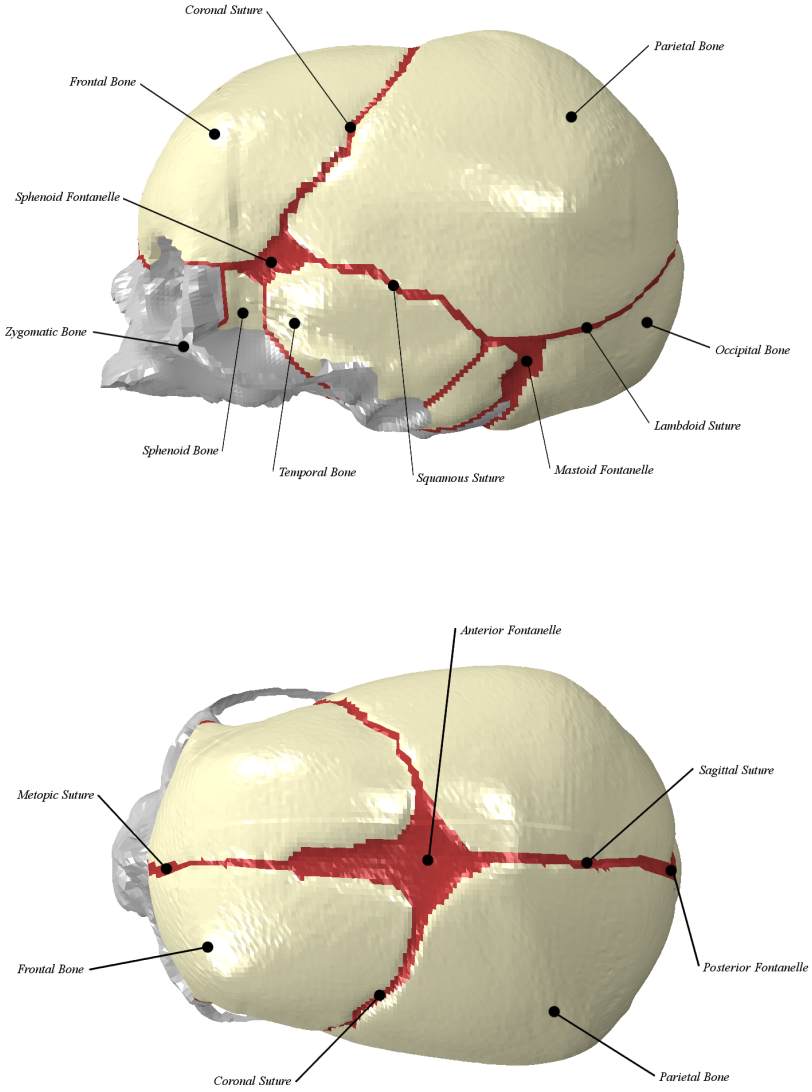

Figure 69: A cut and raised anterior fontanelle.

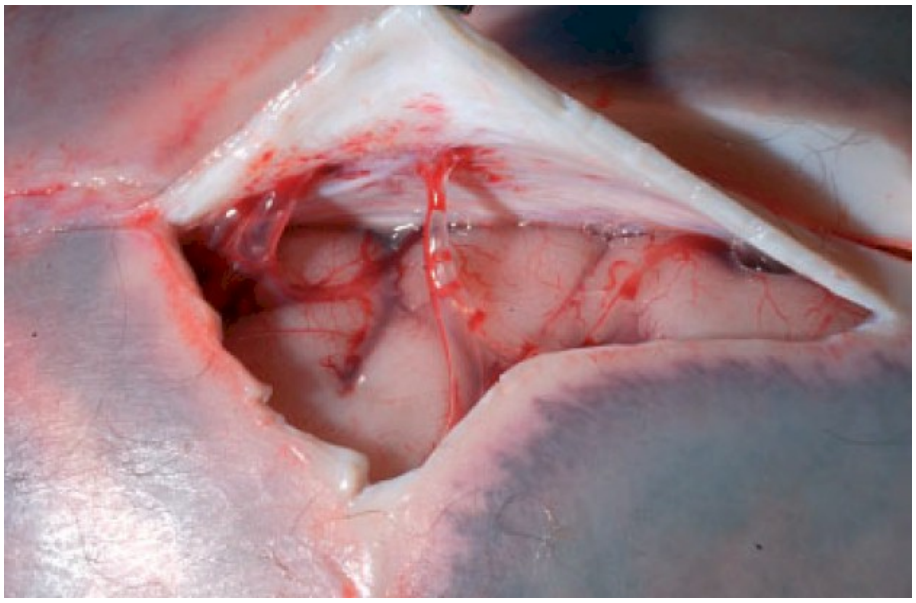

4.1.3 Material properties

The material properties were applied in the same manner as was described by Lapeer [19] and are specified in Figures 70 and 71. Material property definitions and coefficients are outlined in sections 4.3.2 and 4.3.3.

Figure 70: Fetal skull materials defined by coloured sections; Grey is bone, white is cartilage and red denotes the fontanelles.

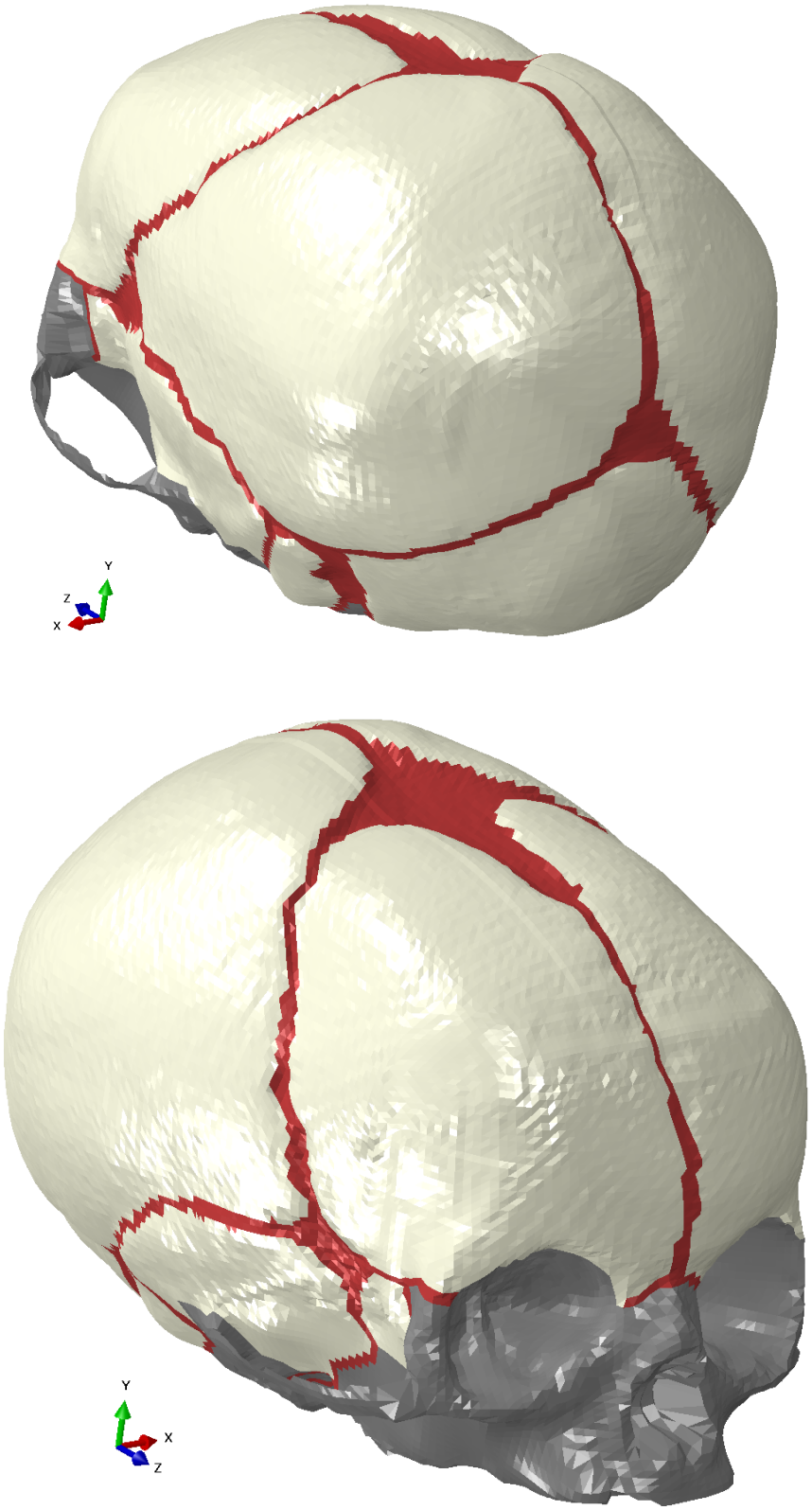

Figure 71: Material thickness zones of the fetal skull as used in the fetal head moulding experiments. The thickness measurements are in mm.

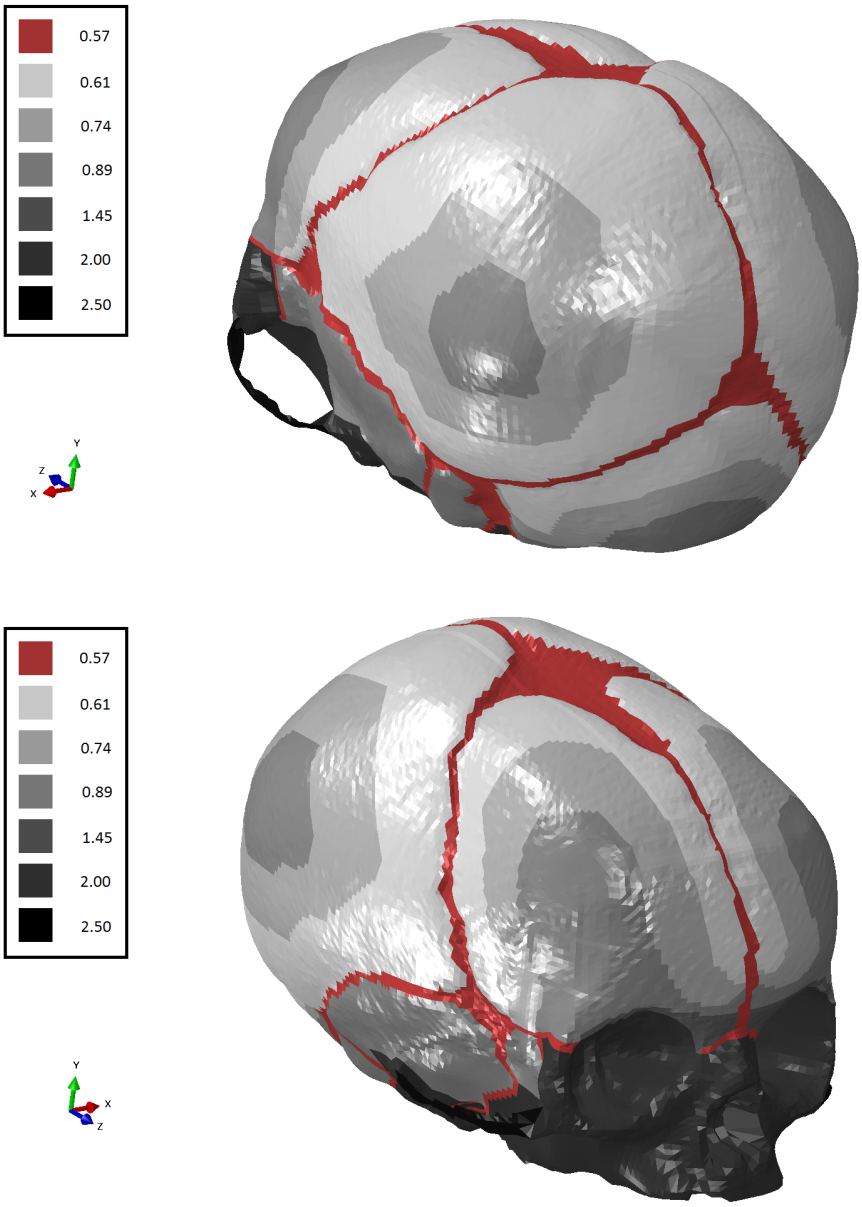

4.2 Fetal head moulding during the first stage of labour

4.2.1 Head-to-cervix pressure

The contact between the uterine cervix and the fetal head results in the head-to-cervix pressure (HCP). As such, the HCP varies with dilatation. Frank Bell [32] modelled the HCP using a hemi-spherical approximation of the spherical lower pole of the fetal head and is illustrated in Figure 72. The largest radius of the fetal head is defined as R and the radius of initial dilatation, r_i. The radius of the current dilatation is denoted by r_0.

Figure 72: A head-to-cervix contact model proposed by Bell [32]. The radial pressure (HCP) exerted by the cervix is denoted by P_r. P_a shows the amniotic pressure (IUP). R denotes the radius at full cervical dilatation. r_n is the radius at an arbitary dilatation . r_0 is the radius of the current dilatation. r_i represents the radius at the initial dilatation.

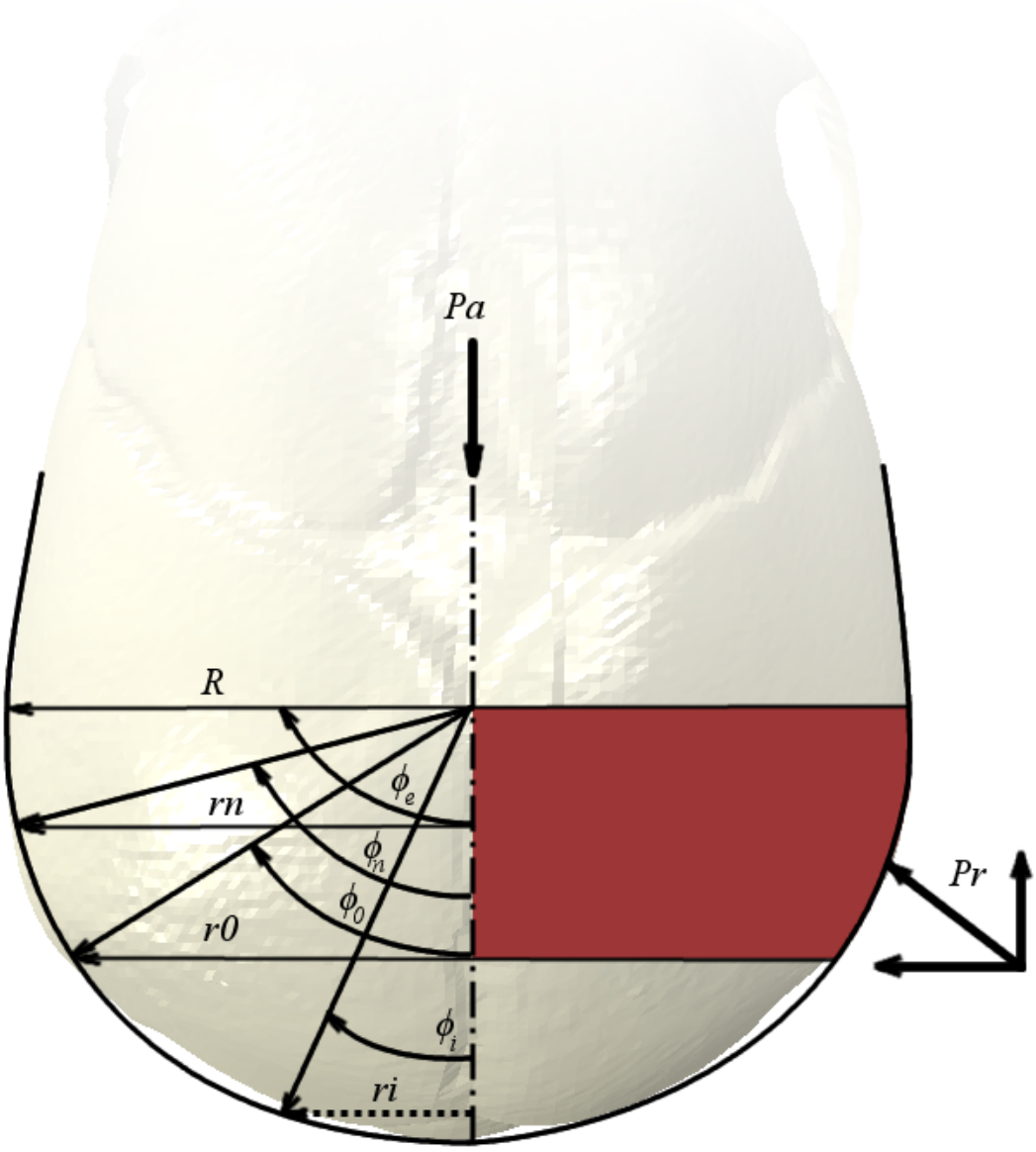

Given findings outlined by Lindgren [103, 104], Bell [32] proposed two possible

pressure distributions given an assumed hemi-spherical lower pole of the fetal head and a quadratic relation between pressure and radius, which were described in detail by Lapeer [19];

1. The radial pressure is proportional to the square of the radius of the head at all levels.

2. The radial pressure is proportional to the increase of the square of the radius of the fetal head at all levels.

Consider the pressure distribution ratio:

$$\Pi_i = \frac{P_r}{P_a} \tag{2}$$

where P_r denotes the radial head-to-cervix pressure (HCP) and the intra-uterine (amniotic) pressure (IUP) is denoted by P_a.

Given the head-to-cervix contact model shown in Figure 72 the equilibrium equation in the vertical direction is given by:

$$P_a \pi R^2 = \int_{\phi_0}^{\phi_e} P_r 2\pi r R \cos\phi \, d\phi \tag{3}$$

where R denotes the radius at full cervical dilatation, $r = R\sin\phi$ and d represents dilatation amount. The pressure ratio Π_i can be derived from working out the integral of Eq. 3 for different functions of P_r.

Pressure distribution 1: Π_1

Given a constant C, the first type of pressure distribution can be described as follows:

$$P_r = Cr^2 \tag{4}$$

With Figure 72 as a guide; Substituting Eq. 4 into Eq. 3, using the relation $r = R\sin\phi$ and integrating as shown by Lapeer [19] gives:

$$P_a \pi R^2 - 2\pi \int_{\phi_0}^{\phi_e} C r^2 R^2 \cos\phi \, \sin\phi \, d\phi = 0 \tag{5}$$

$$P_a - 2 \int_{\phi_0}^{\phi_e} C R^2 \cos\phi \, \sin^3\phi \, d\phi = 0 \tag{6}$$

$$P_a - \frac{CR^2}{2} \left[\sin^4\phi\right]_{\phi_0}^{\phi_e} = 0 \tag{7}$$

and after working out the integral limits:

$$P_a = \frac{CR^2}{2} \left(\sin^4\phi_e - \sin^4\phi_0\right) \tag{8}$$

Because:

$$\phi_e = \frac{\pi}{2} \Rightarrow \sin\phi_e = 1 \Rightarrow \sin^4\phi_e = 1 \tag{9}$$

And:

$$D = \sin\phi_0 = \frac{r_0}{R} \tag{10}$$

Eq. 8 becomes, after substituting Eq. 4 :

$$P_a = \frac{P_r R^2}{2r^2} \left(1 - D^4\right) \tag{11}$$

Finally, since:

$$\gamma = \frac{r}{R} \tag{12}$$

We obtain the pressure ratio:

$$\Pi_1 = \frac{P_r}{P_a} = \frac{2\gamma^2}{1 - D^4} \tag{13}$$

Pressure distribution 2: Π_2

Given a constant C, the second type of pressure distribution can be described as follows:

$$P_r = C\left(r - r_i\right)^2 \tag{14}$$

as shown by Lapeer [19], substituting this into Eq. 3 and after integration yields:

$$P_a - \frac{CR^2}{2}\left[\sin^4\phi\right]_{\phi_0}^{\phi_e} + \frac{4Cr_iR}{3}\left[\sin^3\phi\right]_{\phi_0}^{\phi_e} - Cr_i^2\left[\sin^2\phi\right]_{\phi_0}^{\phi_e} = 0 \tag{15}$$

Working out the integral limits and substituting Eqs. 9, 10 and 14 gives:

$$\frac{6P_a}{3R^2\left(1 - D^4\right) - 8Rr_i\left(1 - D^3\right) + 6r_i^2\left(1 - D^2\right)} = \frac{P_r}{\left(r - r_i\right)^2} \tag{16}$$

With the initial dilatation set to:

$$D_i = \frac{r_i}{R} \tag{17}$$

we obtain the pressure distribution:

$$\Pi_2 = \frac{P_r}{P_a} = \frac{6\left(\gamma - D_i\right)^2}{3\left(1 - D^4\right) - 8D_i\left(1 - D^3\right) + 6D_i^2\left(1 - D^2\right)} \tag{18}$$

Dilatation measurements

The dilatation in the idealised model of Bell can be calculated using the trivial Eq. 10. However, the lower pole of a real fetal skull is not quite hemi-spherical. As such radii at different dilatations will have a degree of variation as compared to the idealised model. This implies dilatation values have to be 'measured'

rather than calculated. The first task to be completed is to derive the position of the sub-occiput bregmatic (SOB) plane. The SOB diameter is defined as the line segment connecting the bregma (centre of the anterior fontanelle) and the tuberosity of the occipital bone - see Figure 73. The SOB plane is defined by the triangular plane with the bregma and the two distal (blue) landmarks as vertices. Of all possible positions of the fetal head near the end of the first stage of labour (full dilatation), the position by which the SOB plane is parallel to the pelvic floor implies that the head presents itself with the smallest possible diameter, i.e. the SOB diameter. As a consequence, the fetus will experience minimal resistance to descend into the birth canal during the second stage.

Figure 73: Definition of sub-occiput bregmatic (SOB) diameter landmarks. Left - Bregma: Centre of the anterior fontanelle marked by the black landmark. Right - Occipital tuberosity (black landmark) and SOB plane landmarks marked by blue dots. Bottom - Sagittal view along the x-axis of the fetal skull with an outlined orientation of the SOB plane and the locations of the bregma and occipital landmarks (here projecting to the same point).

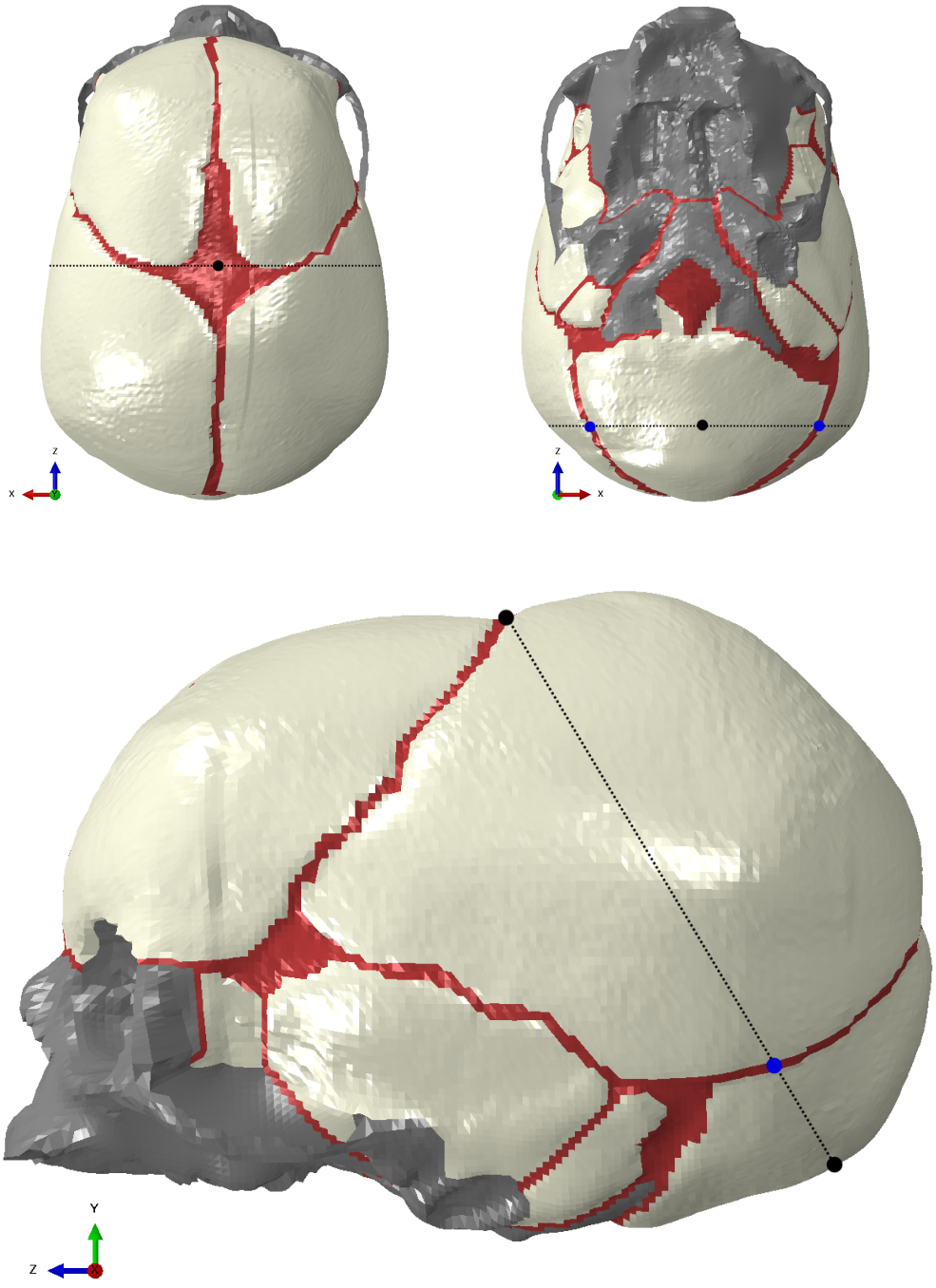

Mathematically, the SOB plane can be defined as:

$$A_1 x + A_2 y + A_3 z + A = 0 \tag{19}$$

The direction cosines $A_1 \ldots A_3$ can be derived from calculating the normal of the triangular plane with vertices $x_1 \ldots x_3$ described earlier:

$$\hat{n} = \frac{(x_3 - x_1) \times (x_2 - x_1)}{|(x_3 - x_1) \times (x_2 - x_1)|} \tag{20}$$

where the unit normal vector $\hat{n} = \begin{bmatrix} n_1 & n_2 & n_3 \end{bmatrix}$ and for $i = 1 \ldots 3$:

$$n_i = \frac{A_i}{\sqrt{A_1^2 + A_2^2 + A_3^2}} \tag{21}$$

The geometric (actual) distance p from the plane to the origin in the direction of the normal is given by:

$$p = \frac{A}{\sqrt{A_1^2 + A_2^2 + A_3^2}} \tag{22}$$

where A can be obtained from Eq. 19 by substituting any of the three vertices defining the plane.

The final position of the SOB plane on the fetal skull model is shown in Figure 74.

Dilatation intervals

Now that we have determined the position and orientation of the SOB plane, we will now determine subsequent parallel planes to bracket the region of cervical contact at a specific dilatation. Since these planes are parallel to the SOB plane we adopt the same plane parameters (direction cosines) $A_1 \ldots A_3$. However, the fourth parameter A which after normalisation gives the geometric distance p as defined in Eq. 22. As mentioned earlier, since the fetal head shape is not ideal, dilatations have to be derived experimentally. This can be done using a model editing software such as Blender [105] which also allows to write scripts in Python. The script to calculate different dilatations and their corresponding p parameter can be found in 6. Figure 74 shows the SOB plane and the plane at dilatation 0.3 which is the initial and smallest possible dilatation, i.e. the cervix is never completely closed.

The same Python script can be used to calculate any distance p for any dilatation D. If we have a sufficient number of sample points then we could create an equation through curve fitting. Figure 75 shows a series of $\begin{pmatrix} p & D \end{pmatrix}$ pairs. The distance measure p' shown on the graph is a translated version of p starting at 0 for dilatation 1.0 and ending at 59.8mm at dilatation 0.0. The interval of $[0 \ldots 59.8]$ was sub-divided into 100 p' values for which the corresponding dilatation D was calculated. Polynomials of increasing order were then fitted. The best fit, i.e. the curve with not just an acceptable RMS error but also capturing the extreme points within the interval well was a polynomial of order 6. This curve can also be seen in Figure 75. Lower order polynomial fits can be seen in Figure 76. Polynomial coefficients are outlined in Appendix C, Section 6.

Table 1 shows the calculated normalised distances p and the non-normalised plane distances by the author using the sixth order polynomial. They are com-

Figure 74: Final position of the sub-occiput bregmatic plane as defined by the outlined three landmarks $x_1 \ldots x_3$ using equations. 19 - 22 as demonstrated by the leftmost plane. And rightmost plane at the smallest dilatation of 0.3.

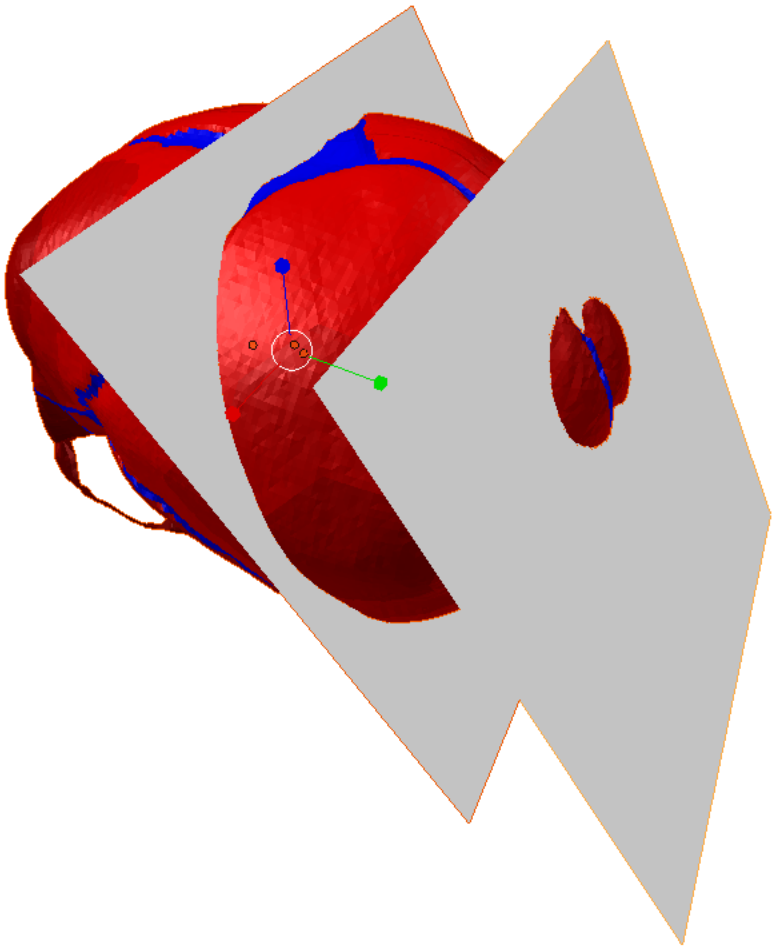

Figure 75: Sixth order polynomial fit shown in red of the dilatation data represented by circles. Polynomial values can be found in Appendix 6 section 6.

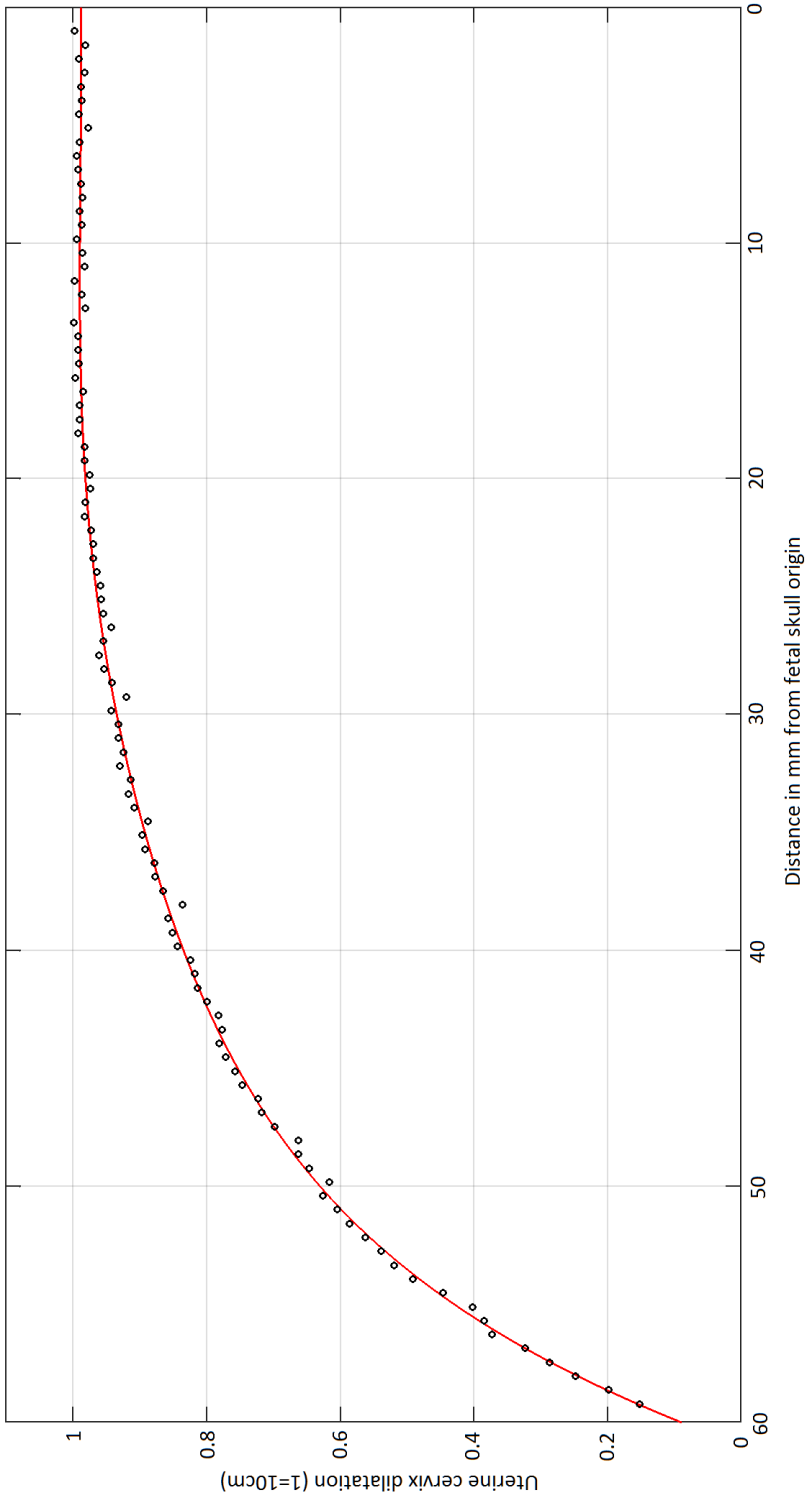

Figure 76: Polynomial fits of the dilatation data. Light blue; 2nd order. Green; 3rd order. Purple; 4th order. Dark blue; 5th order. Red; 6th order. Circles represent the data points and the the polynomial values can be found in Appendix 6 section 6.

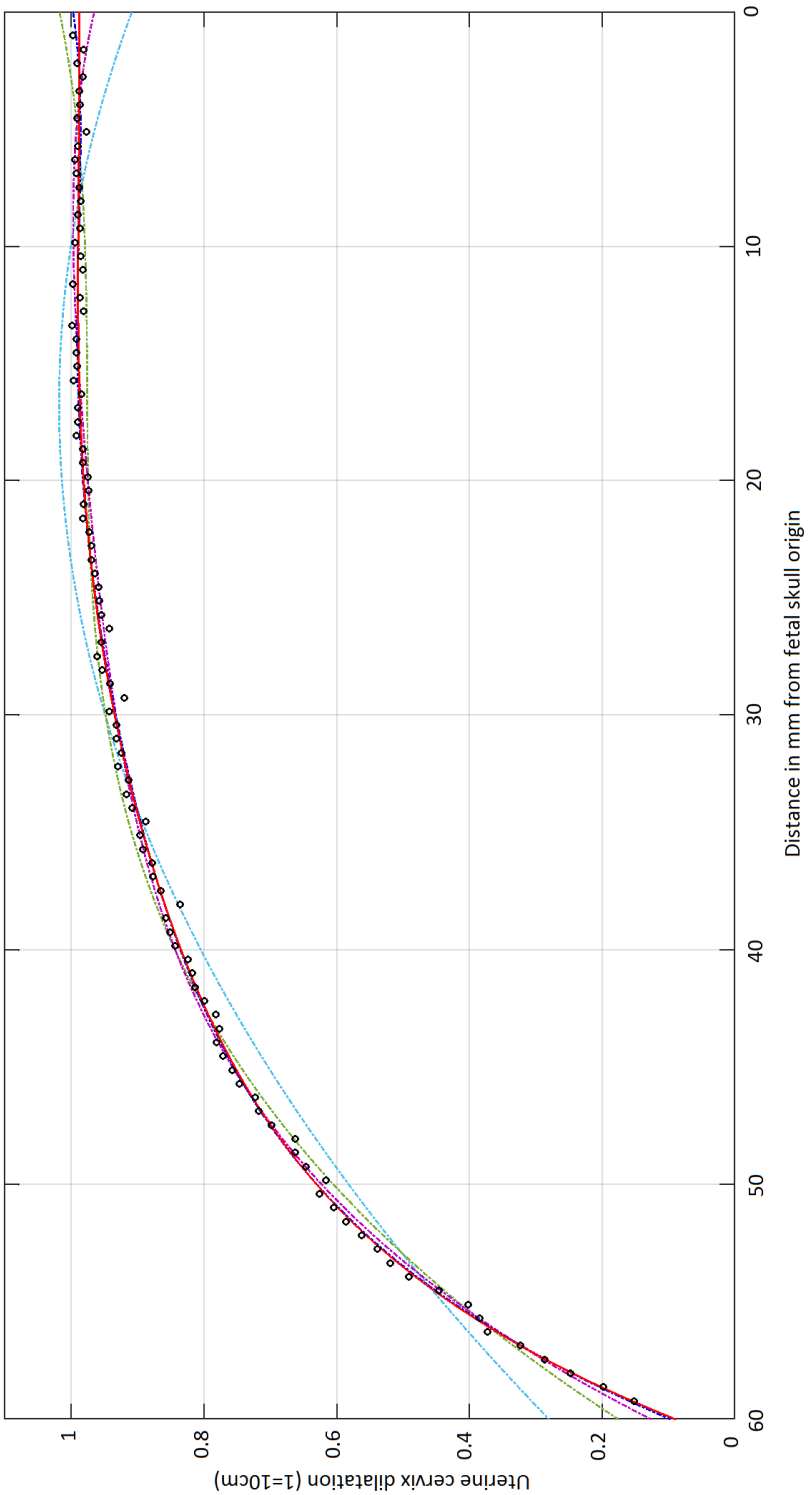

Table 1: Using the fitted sixth order polynomial, distances can be calculated from dilatations. Shown below are the calculated normalised distances p and the non-normalised plane distances A. They are compared to the distances experimentally derived by Lapeer at dilatations 0.3-0.9 in 0.2 intervals [19].

Dilatation	p in mm (Audinis)	A in mm (Audinis)	A in mm (Lapeer)
0.3	57.22	68.206	69.225
0.4	55.55	66.216	
0.5	53.51	63.784	65
0.6	50.92	60.697	
0.7	47.43	56.537	58.5
0.8	42.33	50.457	
0.9	34.14	40.695	48.75
0.95	27.53	32.816	
0.9893	12.75	15.198	

pared to the distances experimentally derived by Lapeer at dilatations 0.3 - 0.9 in 0.2 intervals [19]. It is observed that up to dilatation 0.7, the differences for A are negligible but not quite for dilatation 0.9. It will be shown next that dilatation of 0.9 and above correspond to substantially higher pressure bands than dilatations less than 0.9.

Pressure distribution as a function of dilatation

Now that we can find the plane distance parameter for each dilatation, the pressure distribution between the SOB plane and the plane determined by the dilatation can be calculated using Eq. 18. Lapeer calculated the pressure distributions at 4 discrete levels of dilatation, i.e. 0.3 (initial), 0.5, 0.7 and 0.9 as shown in Figures 77 and 78 [19]. It can be clearly seen that the pressure increases as the dilatation increases. Lapeer assumed that most of the fetal head moulding would be caused in the later part of the first stage, i.e. when the dilatation is as close as possible to its maximum of 1.0 at which stage the cervix would slip over the fetal head. Therefore the consideration of $D = 0.9$ is acceptable. However, since the cervix retracts over the fetal head at a speed of approximately

ΔD=0.1 over 1-2 hours (first stage of labor lasts between about 10-20 hours) and the fetal head anatomy displays time-dependent visco-elastic deformation, the effect of earlier dilatations on the overall deformation of the head should be considered. Therefore, we will recalculate the pressure distribution across the entire dilatation range. This overall distribution will consist of piecewise pressure distributions corresponding with each dilatation interval, ΔD_{int}.

Consider the main dilatation boundaries to be D_{min} and D_{max} then the following holds:

$$\{\forall j \in \mathbb{N}, \forall D_j, D_{j+1}, D_{min}, D_{max}, \triangle D_{int} \in [0.0 \ldots 1.0[\mid D_{max} \geq D_j, D_{j+1} \geq D_{min} \wedge D_{j+1} > D_j \wedge \Delta D_{int} = D_{j+1} - D_j\} \tag{23}$$

where $D_j$and $D_{j+1}$are consecutive interval boundaries.

The same relation holds for the positions of the plane in the direction from back to front of the fetal skull, which we previously denoted as p':

$$\{\forall j \in \mathbb{N}, \forall p'_j, p'_{j+1}, p_{min}, p_{max}, \triangle p_{int} \in \mathbb{R} \mid p'_{max} \geq p'_j, p'_{j+1} \geq p'_{min} \wedge p'_{j+1} > p'_j \wedge \Delta p'_{int} = p'_{j+1} - p'_j\} \tag{24}$$

The pressure distribution as described by Eq. 18 within the interval $j, j+1$ and any position p' of the plane then becomes:

IF $p' < p'_j$ THEN $P_j = P_{prev}$

ELSE IF $p'_{j+1} > p' \geq p'_j$ THEN $P_j = \frac{6(\gamma - D_{min})^2}{3\left(1-D_j^4\right)-8D_{min}\left(1-D_j^3\right)+6D_{min}^2\left(1-D_j^2\right)} P_a$

ELSE IF $p' \geq p'_{j+1}$THEN $P_j = P_{next}$

Where P_{prev} is the pressure, P_{next} is the pressure in the next interval and P_a

Figure 77: Pressure distribution in mmHg on the fetal skull as exerted by the uterine cervix as derived by Lapeer [19]. Left; at a dilatation of 0.3. Right; at a dilatation of 0.5. Figure adapted from [19] for clarity.

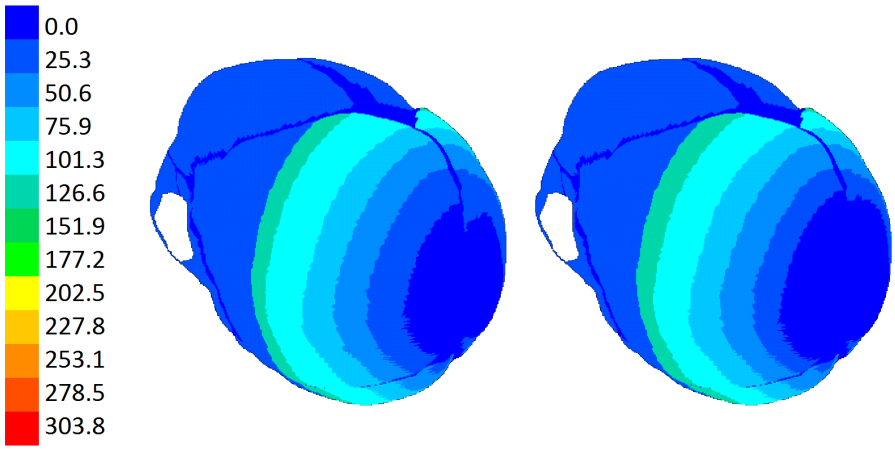

is the amniotic pressure.

Typically, $D_{min} = D_i = 0.3$, i.e. the initial (and smallest possible) dilatation. D_{max} has to be less than 1.0. Although the dilatation interval $\triangle D_{int}$ can be set to an arbitrarily small value, a value of 0.1 is sufficiently small.

Head-to-cervix pressure algorithm

The methodology outlined in the previous sections can be summarised in a step-by-step algorithm, as shown by Algorithm 1.

Intracranial pressure

The fetal skull model outlined in this chapter has so far been defined as an internally empty shell with only the outside topology considered. It is known that because the fetal skull is non-rigid, the shape of the skull is therefore kept due to the brain volume and the intracranial pressure that it exerts because of blood flow and cerebrospinal fluid content [106][107]. This relatively constant outward internal pressure known as the intracranial pressure (ICP) will therefore

Figure 78: Pressure distribution in mmHg on the fetal skull as exerted by the uterine cervix as derived by Lapeer [19]. Left; at a dilatation of 0.7. Right; at a dilatation of 0.9. Figure adapted from [19] for clarity.

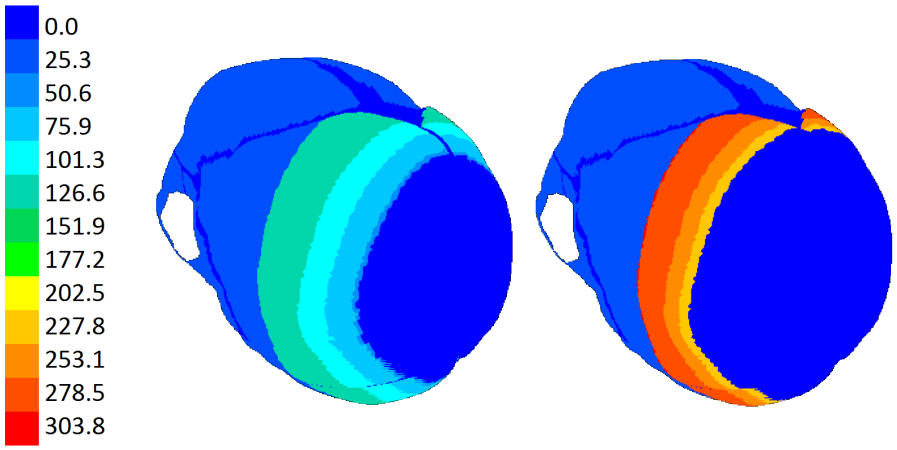

increase the overall rigidity of the skull and should be considered as a structural component of the overall skull. The fetal head moulding model proposed by Lapeer [19] does not consider the ICP which may imply that the reported degree of head moulding is overestimated by this model. Moreover, the model is bound to decrease in volume after deformation whereas the skull and its contents should be incompressible.

It may also be the reason as to why Lapeer's model fails to converge at higher loads (e.g.\ at dilation 0.9) due to buckling and/or excessive rotations of (anterior) fontanelle shell elements. Manual intervention, i.e.\ removal or alteration of the offending elements ameliorates this problem but is a cumbersome task. It is expected that the addition of hydrostatic fluid elements (HFEs) inside the fetal skull cavity will make the model more realistic whilst also reducing the risk of non-convergence at higher pressures exerted by the uterine cervix. To enable a successful application of hydrostatic elements, the fetal skull mesh model needs to be made fully enclosed. The currently used mesh has a hole in the area of the skull base where the spine attaches which needed to be fixed.

Algorithm 1: Application of cervical pressure on a fetal head for a single dilatation band between j and j_1.

```
// Calculate plane parameters following specification of 3 SOB
   landmarks
Input: A_1, A_2, A_3
// Provide the vertex position coordinates
Input: x, y, z
// Calculate the vertex position relative to the SOB plane
position = -A_1 x - A_2 y - A_3 z;
Input: D_i, D[], P_a, R
β = (position + D_j)/R;
α = sqrt(1 - β^2);
for each D_j in D[] do
    // Calculate the cervical pressure load
    headPressure =
     (6P_a(α - D_i)^2)/3(3(1 - D_j^4) - 8D0(1 - D_j^3) + 6D0^2(1 - D_j^2));
    // Only apply head pressure if in the correct range
    if D_j equals first array item and position > -D_j then
        force = P_a;
    else if position < or = -D_j and position > or = D_{j+1} then
        force = headPressure;
    else
        force = 0;
    end
end
```

The following procedure was used to adapt the current mesh into a fully enclosed mesh As shown in Figure 79:

- Define a geometric curve or 'wire' of discrete points (vertices) around the current hole;
- Create a geometric surface bounded by the curve:
  - Seed the new surface with a seed size comparable to the size of the average triangle element in the existing skull model
  - Create a new triangle mesh from the seeded geometry

- Merge the new triangle mesh to the existing skull mesh to produce an enclosed volume
- Finally the internal cavity and boundaries had to be defined using a reference point and face normals

Since the ICP is caused by fluids in the brain, the HFEs have to be incompressible. Therefore, the fluid volume V_f is a function of the temperature T and the fluid mass m but not of the ICP pressure denoted here as p.

$$V_f = f\,(T, m) \tag{25}$$

and

$$\frac{dV_f}{dp} = 0 \tag{26}$$

The volume of the cavity is denoted by V. Due to the incompressible nature of a fluid, the following relation holds:

$$V - V_f = 0 \tag{27}$$

The total mass m of the fluid inside the cavity is in its discrete form the summation of the masses of each of the HFEs:

$$m = \sum_n m^e \tag{28}$$

The mass of each HFE is calculated from its volume V and fluid density ρ (which is a function of T and p). At the initial stage at time i, we get:

$$m_e = \rho(p_i, T_i)V_i^e \tag{29}$$

The initial fluid density ρ_i is a function of the reference frame density ρ_r:

$$\rho(p_i, T_i) = \frac{\rho_r}{1 - p_i/K} \tag{30}$$

Where K is the bulk modulus of the fluid:

$$K = \rho \frac{dp}{d\rho} \tag{31}$$

and its SI unit is as such the same as for pressure, i.e. $\mathrm{N/m^2}$ or Pa. Finally, the fluid density at any arbitrary time t at temperature T and pressure p can be obtained [108] from:

$$\rho(p, T) = \frac{\rho_r}{1 + 3\alpha(T - T_r) - 3\alpha(T_i - T_r) - p/K} \tag{32}$$

Where α is the thermal expansion coefficient.

The experiments in section 4.3 assume the fluid in the brain to be similar to water for which $K = 2.15 \times 10^9$ $\mathrm{N/m^2}$. Considering the temperature T to be constant at all times ($T = T_r = T_i$) and K being several orders of magnitude larger than p (ICP), Eq. 32 can be simplified to:

$$\rho(p, T) = \rho_r \tag{33}$$

In the ABAQUS Standard FE software the HFEs do not appear as solid elements in the usual sense. HFEs will instead appear to be the shell elements that make up the surface of the enclosed skull volume, but due to a reference point typically at the centre of the internal cavity they are actually made up of 4-node hydrostatic fluid volume elements F3D4 which are tetrahedral in shape. A visual representation of htis is shown in Figure 80.

Figure 79: Corrected area of the fetal skull mesh. Light green; Bone. Dark green; Fontanelle.

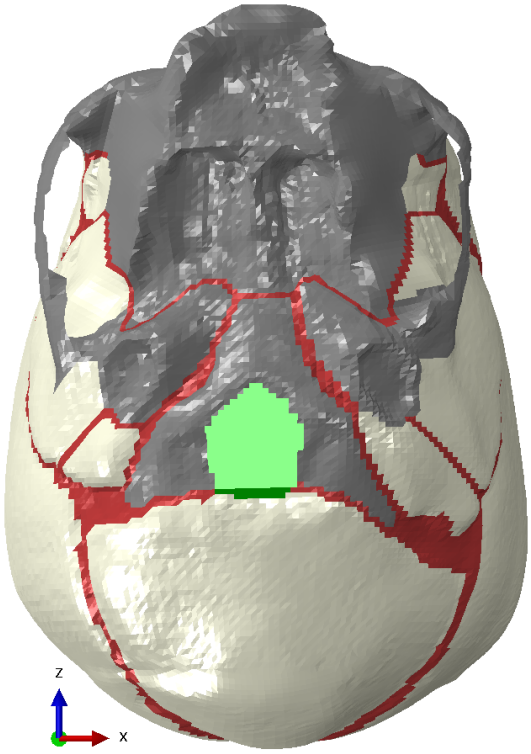

Figure 80: Fetal skull outlines before and after alterations. Left; Original skull outline as described by [19]. Right; Improved skull outline based on hydrostatic fluid elements. The blue shading represents (HFEs) the enclosed volume of the skull where pressure is defined and the RP is the reference point used to formulate HFEs.

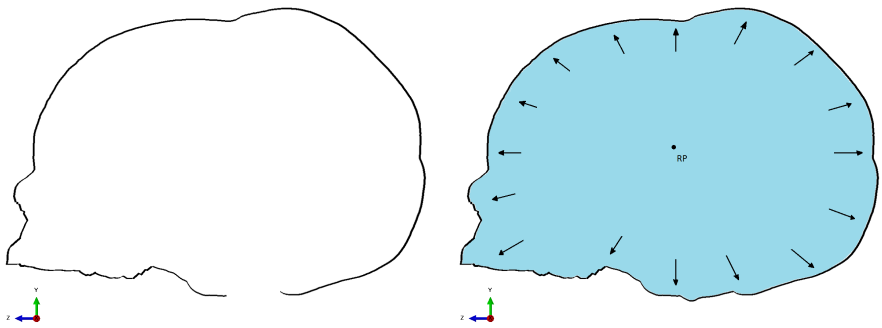

4.3 Experiments

In order to have a baseline result to compare the results obtained using the new methodology, the original experiments described by Lapeer will also be examined alongside the new experiments proposed by this study.

The experimental setup will take into consideration a number of variables:

- Material properties of the fontanelles - Initial experiments will make use of elastic and hyperelastic fontanelle material properties. This is to have a way of comparing the results with previously published work and to ensure that the setup and methodology was understood correctly. The number of experiments using the elastic material properties for the fontanelles will be limited as they define a fetal skull that is considered to be too stiff. It would therefore underestimate the amount of deformation.

- Variations in pressure distributions - A number of different dilatations and the resulting pressure distributions will be analysed.

The experiments in this chapter only consider the effects of the pressure exerted upon the fetal skull by the uterine cervix. Maternal features such as the pelvic bones or the pelvic floor muscles do not have any influence on the amount of Fetal Head Moulding experienced during the first stage of labour and are therefore omitted from the simulations.

4.3.1 Description of the experimental setups

All experiments will share the material definitions which were outlined in section 4.1.3.

Unless stated otherwise the dilatation values were defined by Audinis in Table 1. Dilatation configurations that will be analysed are:

- 0.9 dilatation. Some experiments will use values defined by Lapeer [19]

Table 2: Diameters in mm of the undeformed skull model as shown in Figure 81.

	Unmoulded fetal skull
SOBD	90.19
SOFD	114.63
OFD	119.42
OrVD	117.98
OrOD	119.45
MaVD	129.31
BPD	89.44
BTD	83.53
BFD	64.93

- 0.95 dilatation
- 0.95 and 0.9 combined
- 0.9 to 0.3 in 0.2 increments using values as described by Lapeer [19]
- 0.9 to 0.3 in 0.1 increments
- 0.95 to 0.3 in 0.1 increments for the range of 0.9 to 0.3 and and additional 0.05 increment to get from 0.9 to 0.95.

The pressure distributions were calculated using the algorithm outlined earlier - see Algorithm 1. The positions of the various fetal skull diameters used for validation are shown in Figure 81.

4.3.2 Skull moulding - linear elastic fontanelles

This section outlines results obtained using fontanelles with linear elastic properties. Although soft tissues such as fontanelles are visco/hyperelastic in nature (hyperelastic materials are covered in more depth in the next section) an elastic formulation of the fontanelle material still has validity and forms a sound basis for comparison of results with previous work and the more complex hyperelastic formulation covered in the next section.

Figure 81: Fetal head measurements. In both orientations, the measurements are taken along the centerline of the head.

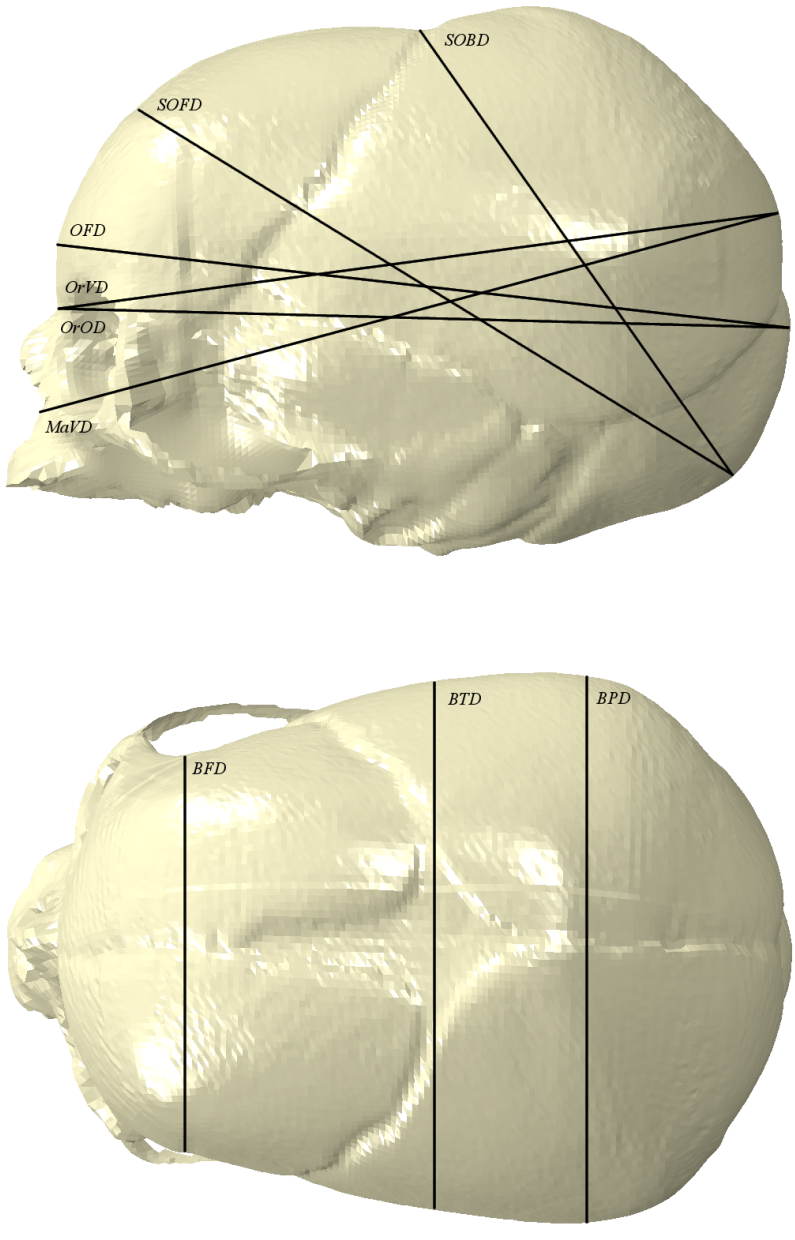

Table 3: Experimental results on a fetal skull with **linear elastic** fontanelle material properties at a dilatation **D = 0.9**. Deformation U is in mm, stresses are in N/mm^2. (Lapeer) denotes dilatation values used from [19]. (Audinis) implies newly calculated dilatations by the author. U; Magnitude of deformation. S; von Mises stress. S12; Shear stress.

Experiment description	Max U	Max S	Max S12	Min S12
Skull with ICP (Lapeer)	1.259	34.85	10.53	-14.57
Skull with ICP (Audinis)	0.896	12.42	5.325	-4.882
Skull without ICP (Lapeer)	1.425	56.37	13.99	-24.04
Skull without ICP (Audinis)	0.919	22.37	9.444	-9.485

Table 4: Experimental results on a fetal skull with **linear elastic** fontanelle properties at a **D = 0.95** and **D = 0.9 to 0.95**. Deformation U is in mm, stresses are in N/mm^2. U; Magnitude of deformation. S; von Mises stress. S12; Shear stress.

Experiment description	Max U	Max S	Max S12	Min S12
Skull with ICP where D = 0.95	0.544	8.816	3.409	-2.813
Skulll with ICP where D = 0.95 to 0.9	1.167	15.1	6.764	-5.928
Skull without ICP where D = 0.95	0.885	9.955	4.008	-4.372
Skull without ICP where D = 0.95 to 0.9	1.054	26.41	11.6	-11.12

The fontanelle material definition for the experiments in this section was defined to be an elastic isotropic material with a long-term moduli time scale.

Young's modulus in MPa was set to 31.5 with a Poisson's ratio at 0.45.

The bone material definition for the experiments was defined to be an elastic isotropic material with a long-term moduli time scale.

Young's modulus in MPa was set to 4460 with a Poisson's ratio at 0.21.

The cartilage material definition for the experiments was defined to be an elastic lamina material with a long-term moduli time scale.

Material coefficients in MPa were defined as; E1: 3934, E2: 984, Nu12: 0.08, G12: 1480, G13: 1833 and G23: 1833.

Figure 82: Differences in deformation magnitude (mm) between dilatation pressure distribution methods proposed by Lapeer [19] against those proposed by this research on a skull model with **linear elastic** fontanelles, **without ICP** and $\mathbf{D = 0.9}$. Top row: Lapeer method. Bottom row: Audinis method.

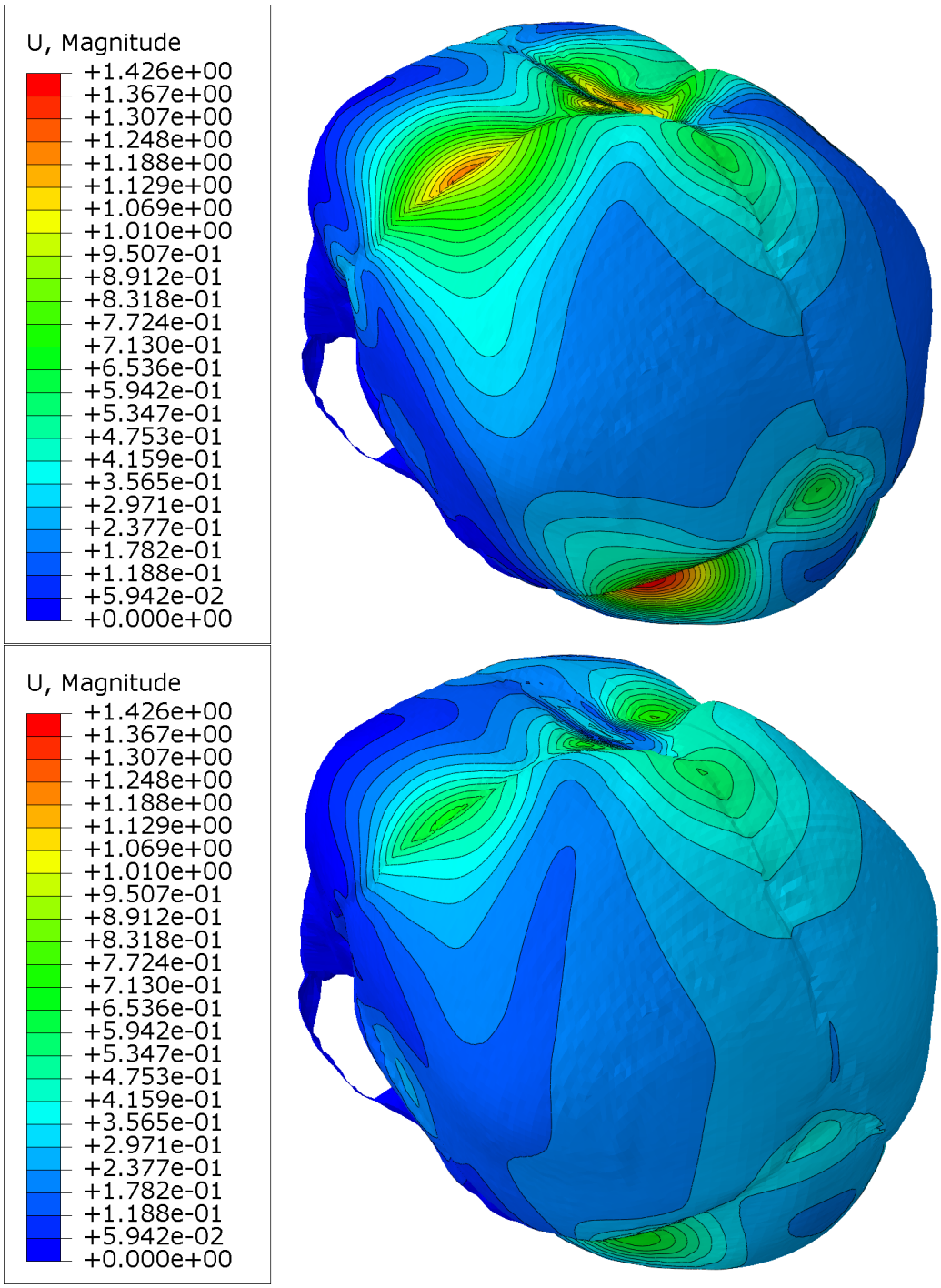

Table 5: Changes in fetal skull diameters (mm) after moulding under a cervical dilatation **D = 0.9**. Fontanelles were defined as **linear elastic**.

Experiment description	SOBD	SOFD	OFD	OrVD	OrOD	MaVD	BPD	BTD	BFD
Skull with ICP (Lapeer)	0.37	-0.07	0.39	0.12	0.37	0.13	-0.03	0.14	0.09
Skull with ICP (Audinis)	0.44	-0.05	0.26	0.06	0.27	0.08	-0.16	0	-0.05
Skull without ICP (Lapeer)	-0.14	-0.18	0.27	0.07	0.29	0.09	-0.08	0.07	-0.026
Skull without ICP (Audinis)	0.22	-0.13	0.15	0.01	0.19	0.01	-0.25	-0.28	-0.18

Table 6: Changes in fetal skull diameters (mm) after moulding under a cervical dilatation **D = 0.95** and **D = 0.9 to 0.95**. Fontanelles were defined as **linear elastic**.

Experiment description	SOBD	SOFD	OFD	OrVD	OrOD	MaVD	BPD	BTD	BFD
Skull with ICP where D = 0.95	0.24	-0.02	0.01	0.05	0.13	0.08	-0.19	-0.27	-0.13
Skull with ICP where D = 0.95 to 0.9	0.56	-0.06	0.29	0.06	0.3	0.08	-0.18	-0.11	-0.03
Skull with no ICP where D = 0.95	0.13	-0.08	0	0.02	0.05	0.06	-0.28	-0.45	-0.27
Skull without ICP where D = 0.95 to 0.9	0.35	-0.15	0.19	0	0.22	0.04	-0.28	-0.26	-0.17

4.3.3 Skull moulding - hyperelastic fontanelles

This section outlines results obtained using fontanelles with linear hyperelastic properties. Hyperelastic material theory is briefly outlined in Appendix D.

Because soft tissues in reality have nonlinear material properties using a linear elastic formulation to model them as was outlined in the previous section will underestimate the deformation that would be seen in reality. A number of authors provide details on hyperelastic fontanelle materials [19, 109]. Given that this research aims to improve upon the work done by Lapeer [19] the same hyperelastic material definition will be used.

This was originally based on findings by Bylski et al.[109] who, given principal stretch ratios λ_1 and λ_2, report the constitutive relations to be:

$$T_1 = \left[2hC_1\left(\lambda_1^2 - \lambda_1^{-2}\lambda_2^{-2}\right)\left(1 + \alpha\lambda_2^2\right)\right]/\lambda_1\lambda_2 \tag{34}$$

$$T_2 = \left[2hC_1\left(\lambda_2^2 - \lambda_1^{-2}\lambda_2^{-2}\right)\left(1 + \alpha\lambda_1^2\right)\right]/\lambda_1\lambda_2 \tag{35}$$

where the T_1 and T_2 represent constitutive relations in a Mooney-Rivlin material model formulation. h is the initial, uniform thickness of the membrane, $\alpha = C_1/C_2$, and C_1 and C_2 are the material constants with dimensions of stress.

The principal stretch ratios λ_1 and λ_2 are described as:

$$\lambda_1 = dS/ds \tag{36}$$

$$\lambda_2 = p/r \tag{37}$$

where dS and ds are the meridional arc lengths in the deformed and undeformed configurations of the material, and p and r are the circumferential lengths in the

Table 7: Experimental results on a fetal skull with **hyperelastic** fontanelle material properties at $\mathbf{D = 0.9}$. Deformation U is in mm, stresses are in N/mm^2. (Lapeer) denotes dilatation values used from [19]. (Audinis) implies newly calculated dilatations by the author. * Only converged up to 0.636 of total load. ** Only converged up to 0.74 of total load. U; Magnitude of deformation. S; von Mises stress. S12; Shear stress.

Experiment description	Max U	Max S	Max S12	Min S12
Skull with ICP (Lapeer)	3.238	29.72	11.72	-8.688
Skull with ICP (Audinis)	1.911	16.69	7.314	-5.566
Skull without ICP (Lapeer)*	2.399	28.33	13.91	-6.239
Skull without ICP (Audinis)**	1.591	22.67	10.59	-9.248

Table 8: Experimental results on a fetal skull with **hyperelastic** fontanelle material properties at a dilatation $\mathbf{D = 0.95}$ and $\mathbf{D = 0.9}$ **to** $\mathbf{0.95}$. Deformation U is in mm, stresses are in N/mm^2.* Only converged up to 0.76 of the total load. U; Magnitude of deformation. S; von Mises stress. S12; Shear stress.

Experiment description	Max U	Max S	Max S12	Min S12
Skull with ICP where D = 0.95	1.013	13.99	5.466	-4.612
Skull with ICP where D = 0.9 to 0.95	2.317	21.52	8.761	-6.791
Skull without ICP where D = 0.95	2.022	14.89	5.627	-5.613
Skull without ICP where D = 0.95 to 0.9 *	2.635	28.06	13.11	-10.08

deformed and undeformed configurations as described by Bylski et al.[109].

The fontanelle material definition was therefore defined to be a hyperelastic isotropic material with a polynomial strain energy potential and a long-term moduli time scale.

Material coefficients in N/mm^2 were defined as; C10: 1.18, C01: 0.295 and D1: 0 where, in the context of this section, $C_1 = C10$ and $C_2 = C01$.

Bone and cartilage material definitions remained unchanged from the ones outlined in the previous section.

Figure 83: Differences in deformation magnitude (mm) between dilatation pressure distribution methods proposed by Lapeer [19] against those proposed by this research on a skull model **hyperelastic** fontanelles, **with ICP** and **D = 0.9**. Top row; Lapeer method. Bottom row; Audinis method.

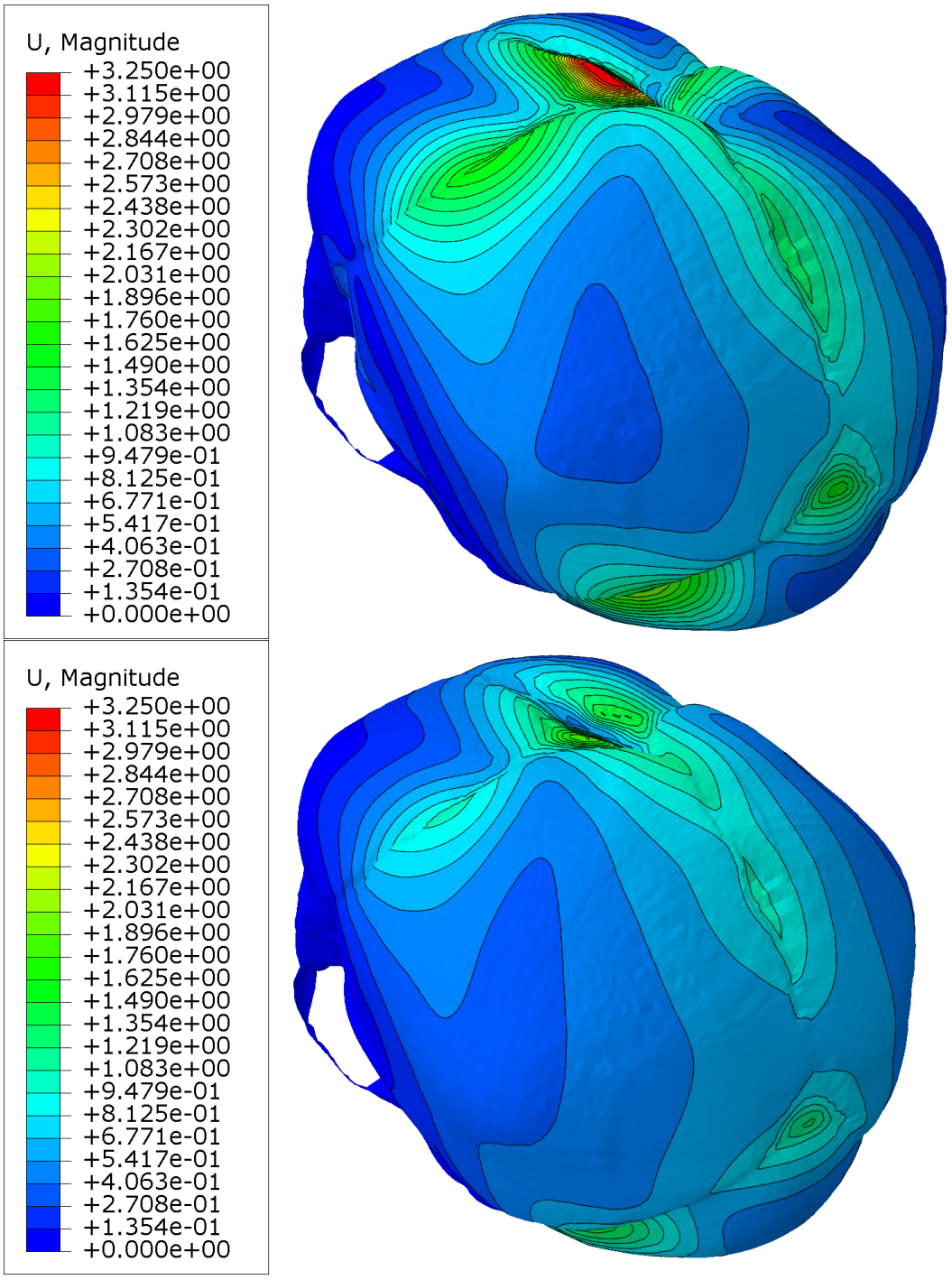

Table 9: Changes in fetal skull diameters (mm) after moulding under a cervical dilatation **D = 0.9**, **D = 0.95** and **D = 0.9 to 0.95**. Fontanelles were defined as **hyperelastic**.

Experiment description	SOBD	SOFD	OFD	OrVD	OrOD	MaVD	BPD	BTD	BFD
Skull with ICP (Lapeer) where D = 0.9	0.52	-0.18	0.7	0.57	0.67	0.62	-0.18	0.21	0.23
Skull with ICP (Audinis) where D = 0.9	0.74	-0.12	0.59	0.32	0.61	0.39	-0.44	-0.37	-0.1
Skull with ICP (Audinis) where D = 0.95	0.43	-0.04	0.26	0.20	0.32	0.26	-0.39	-0.59	-0.28
Skull with ICP where D = 0.95 to 0.9	0.8935	-0.168	0.711	0.358	0.722	0.438	-0.4781	-0.3592	-0.0646

Table 10: Changes in fetal skull diameters (mm) after moulding under a cervical dilatation ranges of **D = 0.9 to 0.3** and **D = 0.95 to 0.3**. Fontanelles were defined as **hyperelastic**.

Experiment description	SOBD	SOFD	OFD	OrVD	OrOD	MaVD	BPD	BTD	BFD
Skull with ICP (Lapeer) where D = 0.9 to 0.3	0.12	-0.12	0	0.46	-0.11	0.41	0.4	1.07	0.59
Skull with ICP (Audinis) where D = 0.9 to 0.3	0.29	-0.13	0.12	0.48	0.01	0.46	0.26	0.9	0.53
Skull with ICP (Audinis) where D = 0.95 to 0.3	0.29	-0.13	0.12	0.48	0.01	0.46	0.26	0.9	0.53

Table 11: Changes in fetal skull diameters (mm) after moulding under a cervical dilatation **D = 0.9**. Fontanelles were defined as **hyperelastic**.

Experiment description	SOBD	SOFD	OFD	OrVD	OrOD	MaVD	BPD	BTD	BFD
Skull without ICP (Lapeer)	-0.58	-0.17	0.25	0.33	0.31	0.37	-0.29	-0.03	0.01
Skull without ICP (Audinis)	0.13	-0.17	0.31	0.1	0.38	0.17	-0.58	-0.7	-0.33

Table 12: Changes in fetal skull diameters (mm) after moulding under a cervical dilatation **D = 0.95** and a range of **0.9 to 0.95**. Fontanelles were defined as **hyperelastic**.

Experiment description	SOBD	SOFD	OFD	OrVD	OrOD	MaVD	BPD	BTD	BFD
Skull without ICP (Audinis) where D = 0.95	0.28	-0.15	0.07	0.08	0.19	0.15	-0.73	-1.22	-0.67
Skull without ICP (Audinis) where D = 0.95 to 0.9	0.17	-0.22	0.47	0.11	0.55	0.2	-0.76	-0.86	-0.4

4.3.4 Discussion of results

The newly developed model by the author differs in two ways to the original model developed by Lapeer [19], i.e. the addition of the ICP by using hydrostatic fluid elements (HFEs) and the more precise calculation of the dilatation and boundary plane distances for different dilatation bands. From the results presented in the previous sections it can be seen that only three models fail to converge due to excessive rotations of fontanelle elements. This is when hyperelastic fontanelles are used and no ICP is present ('hollow' model). The first one of these is the original model by Lapeer at D = 0.9 which converges to 0.636 (this value has been observed many times over, following numerous simulation attempts when using this model) - see Table 7. The other two are by the author at D = 0.9 and D = 0.9 - 0.95 (Tables 7 and 8. This does not happen when linear elastic fontanelles are used or when the HFE elements are added to simulate the ICP. Indeed, linear elastic fontanelles exhibit stiffer behaviour than hyperelastic fontanelles and are bound to underestimate the degree of moulding. The ICP stabilises the deformation and minimises the chance of the hyperelastic fontanelle elements warping due to excessive rotations and which make the FE calculations unstable. Numerical stability is one thing but is the addition of the ICP also more realistic? The interesting phenomenon that is observed is the change of the SOBD (which is a crucial diameter to assess fetal head moulding). Lapeer [19] observed a decrease of the SOBD at D = 0.9 - see Table 11. This was confirmed through clinical evaluations by Sorbe and Dahlgren [110]. Sorbe and Dahlgren measured the principal diameters of the fetal head (see Figure 81) of 319 babies shortly after birth and up to three days later when the elastic component of the moulding effect has vanished. When the ICP is applied using HFEs in the model, the SOBD increases when the fetal head moulds - see Tables 9 and 10. Without ICP but at D = 0.95, the SOBD also increases - see Tables 11 (Audinis)

and 12. It can also be observed that for D = 0.95 less deformation (moulding) happens than for D = 0.9. This is the same effect as applying the ICP which also results in less deformation. This may imply that when the overall deformation of the fetal skull (moulding) is slightly less, the SOBD increases, whereas when additional moulding is observed the SOBD decreases. Further experiments are needed to verify this statement. It should also be noted that the measurement of the SOBD is nontrivial since one of the landmarks defining the SOBD, i.e. the bregma, lies inside the highly deformable anterior fontanelle. Measuring the bregma coordinates at this location would give nonsensical values for the SOBD so instead two neighbouring points lying on the frontal bones and lateral to the 'real' bregma location are used and the point in the middle is then used as the 'virtual' bregma. Although this approach was consistently used across all experiments there is a degree of uncertainty in the reported values of the SOBD changes due to using a 'virtual' bregma landmark.

Despite differences in diameter changes, it can be seen in Figures 83 and 82 that the author's and Lapeer's models exhibit the same fetal head shapes after moulding though the former's degree of deformation is less due to the addition of the ICP. However, the latter improvement makes the model more realistic and also makes the FE calculations more stable. Both of these improvements are crucial for the next experiments which will assess further deformation on the already moulded skull which require stable analyses and incompressible (non volume changing) models.

5 Fetal head moulding during assisted labour

The analysis of the fetal head moulding during the first stage of labour was an important step for developing a more robust and versatile model of the fetal head. These fetal skull model improvements that were outlined, described and tested in the previous chapters will now be used to simulate the effects of instrumental interventions. Chapter 2 provided an in-depth look at the background of the vacuum extraction and forceps procedures. The purpose of this chapter is to attempt to provide some understanding on what applications of these instruments could lead to possible harm to the fetal head and in turn the mother.

This chapter will further outline the software tools that were developed for the purposes of setting up the various scenarios that will be analysed and discussed in detail.

Modelling the forceps blades

The forceps models used for the experiments were modelled after the Neville-Barnes forceps as shown in Figure 13. Because computer aided design drawings were not available manual modelling of the blades had to be undertaken. This was achieved using pictures of real forceps as templates for each axis and then modelled by hand using computer model editing software Blender [105]. The resulting model of the forceps blades is shown in Figure 90.

5.1 Forceps placement

The lack of rigid constraints to govern the motion of the fetal head means that deciding the optimal forceps placement orientations and positions is a challenge. Overcoming this difficulty was one of the challenges that was tackled by the study.

Figure 84: Fetal skull in the occiput anterior vertex presentation

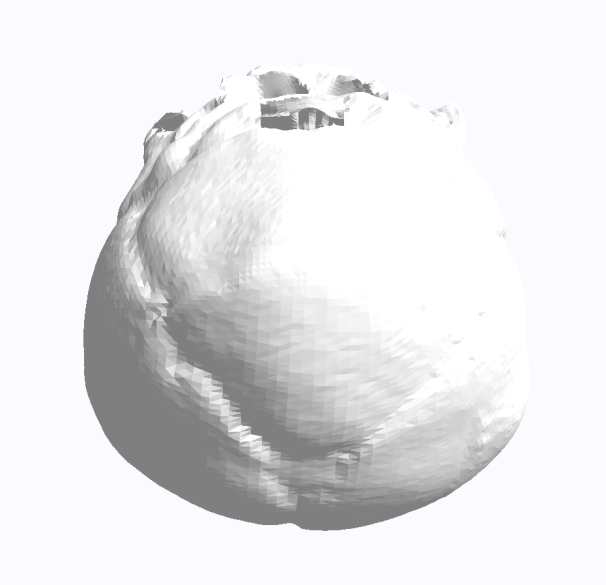

Before describing the process of how the forceps placement positions and orientations were chosen, we first must define a set of ground truths:

- As shown in Figure 84 the occiput anterior vertex presentation will be considered to be default placement and orientation of a fetal head going through the normal stages of labour.
- The correct placement of the blades will be described as being symmetrically placed around the fetal head along the longest axis of the head as shown by Figure 85 and Figure 86.
- All other placement positions and fetal head orientations will be considered to be a deviation from the "correct" and most desired configuration.

As outlined earlier the initial placement of the forceps as shown in Figure 85 is considered to be the most desired configuration. This application and orientation of the forceps was then independently verified and demonstrated by Dr Edward Morris as shown in Figure 86. For the purposes of this study, this position was

Figure 85: Initial forceps placement on the fetal skull

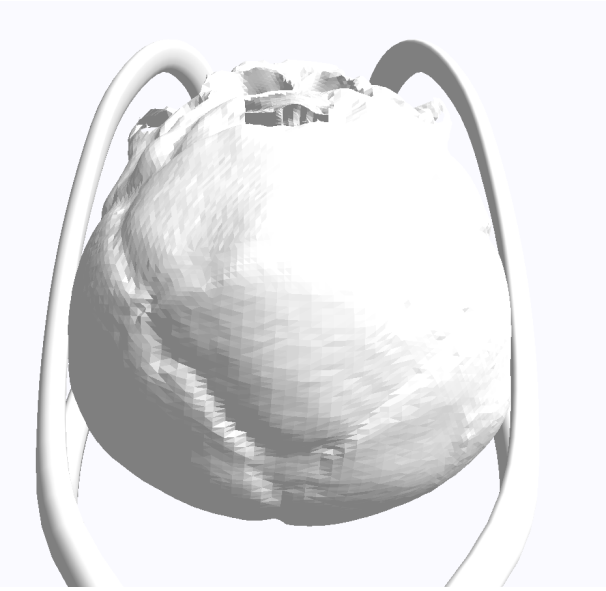

Figure 86: Demonstration of correct placement of the forceps blades. Demonstrated by Dr. Edward Morris.

Figure 87: Demonstration of alternative symmetric placement of the forceps blades. Demonstrated by Dr. Edward Morris.

considered to be "correctly placed" and also an example of the ideal symmetrical placement. There are other types of symmetric placement such as that shown in Figure 87, but these were not considered to be an ideal placement scenario.

The differences in head alignment shown in Figure 86 and Figure 87, indicate that variations around the x-axis of the fetal head (this is the axis orientation relative to the skull model used in this thesis) should be considered as a variable used to define a number of possible positions that can be analysed.

The head orientations and forceps placement positions as described and demon-

Figure 88: Demonstration of forceps placement on a fetal head in a right occiput transverse presentation. Demonstrated by Dr. Edward Morris.

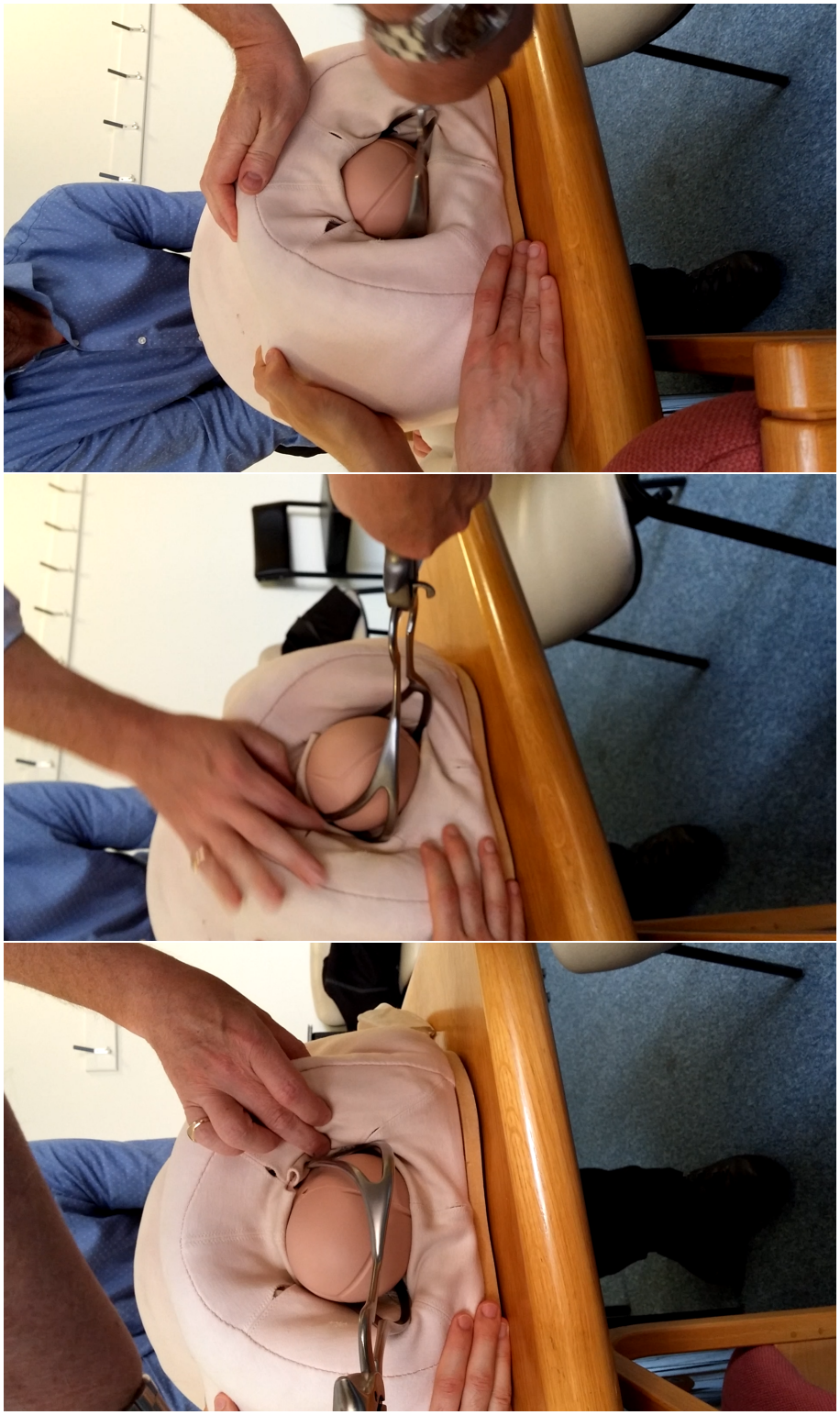

Figure 89: Simulation environment setup used for intial analysis of the head orientation for forceps placement.

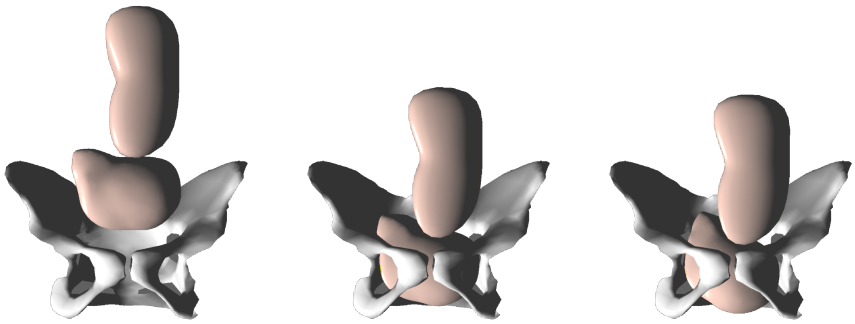

strated by Dr. Morris; a small subset of which were shown in Figure 87 and Figure 88, were also further validated in a simulation environment.

The validation environment consisted of:

- A model of the maternal pelvis - this was a low fidelity model of the pelvic model described in section 3.1.1
- A simplified model of the fetal head - this was scaled to match the size of the fetal skull that will be used for the in depth experiments and analysis
- A basic model of the fetal body
- Body and head were connected with a link element simulating the presence of the neck - the neck model was developed in such a way as to limit certain degrees of freedom.

Once the fetal head was in a position and orientation that was similar to that which was demonstrated by Dr. Morris, the angular orientation of the fetal head was noted. This orientation was then used when applying the forceps to the skull in the BirthEngine simulation environment.

5.1.1 Analysis of applied force

The in-depth overview of obstetric forceps in Chapter 2 provided a sound basis on which to formulate the method of forceps application to the fetal skull model. The formulation of the loading model had to consider the limitations of the skull model to be used for analysis, namely the fact that:

- The skull model only considers the bone and lacks any layers of soft tissue that would be present on a real fetal head

The outlined limitation is an important one to consider, as this will impact greatly on how accurate the results of the loading model are going to be. Given the fact that computer simulations are an approximation already, adding the additional soft layers may in fact produce less accurate results than the simpler model without soft skull tissues. Following the investigation into the fetal anatomy in Chapter 3, an important assumption was therefore made:

- Omitting the soft tissues of the skull from the simulation will still produce results with adequate accuracy

Although the soft tissues will no longer be modelled, they cannot be ignored completely, as they still provide an important skull-to-forceps interface. To this end, a uniform buffer of skin 5mm thick will be assumed to surround the fetal skull. For the thickness, 5mm is the approximate order of magnitude of skin thickness at full gestation [111]. This approximation of the skin thickness is actually an oversimplified approximation of what real skin thickness variations would be like, but given that this is only meant to represent a boundary between two very rigid bodies, this approximation is acceptable.

Now that the assumptions have been outlined, it is time to consider the traction forces in effect. Reported values state that traction forces applied to

forceps can vary and generally range from 30-45 pounds [112]. This corresponds to forces of 133-200N and is lower than the proposed upper limit of no greater than 50 pounds of traction force per forceps application. The level of traction force is covered in depth in literature, but it is not the only force that will have an effect on the fetal skull. There is also the compression force of the forceps blades against the fetal head. Given the shape of most forceps (see Chapter 2), this compressive force will be comparatively low when the forceps have been correctly (symmetrically) applied. The compressive force will become substantially larger given incorrect (asymmetric) placement of the forceps.

To calculate the compression force on the experimental skull the aforementioned skin buffer will be used, with a forceps clearance value range of -2.5mm to 2.5mm used for calculating the compression force per skull element. The maximum compression force was considered to be 120N[113] and this corresponded to the lowest clearance range value of -2.5mm.

The magnitude of the clearance force can then be defined by the following empirical equation as described in [61]:

$$||\mathbf{F}_{Cl}|| = \frac{120 \times (2.5 - Cl)^2}{5^2} \tag{38}$$

Where Cl is the clearance and $||\mathbf{F}_{Cl}||$ is the magnitude. The quadratic term in this case is to provide more weight to any negative clearances which would correspond to proportionally higher compression forces when compared to positive values.

Using the collision detection engine outlined in Chapter 3 and the method for defining interactions between the fetal skull and the obstetric forceps, the variations in head positions could then be defined as shown in Figure 90.

Figure 90: Forceps to fetal skull placement definitions. Top; Symmetric, with visualised forceps. Bottom; Skull only with visualised forces resulting from the application of the forceps. All visualised forces are in N.

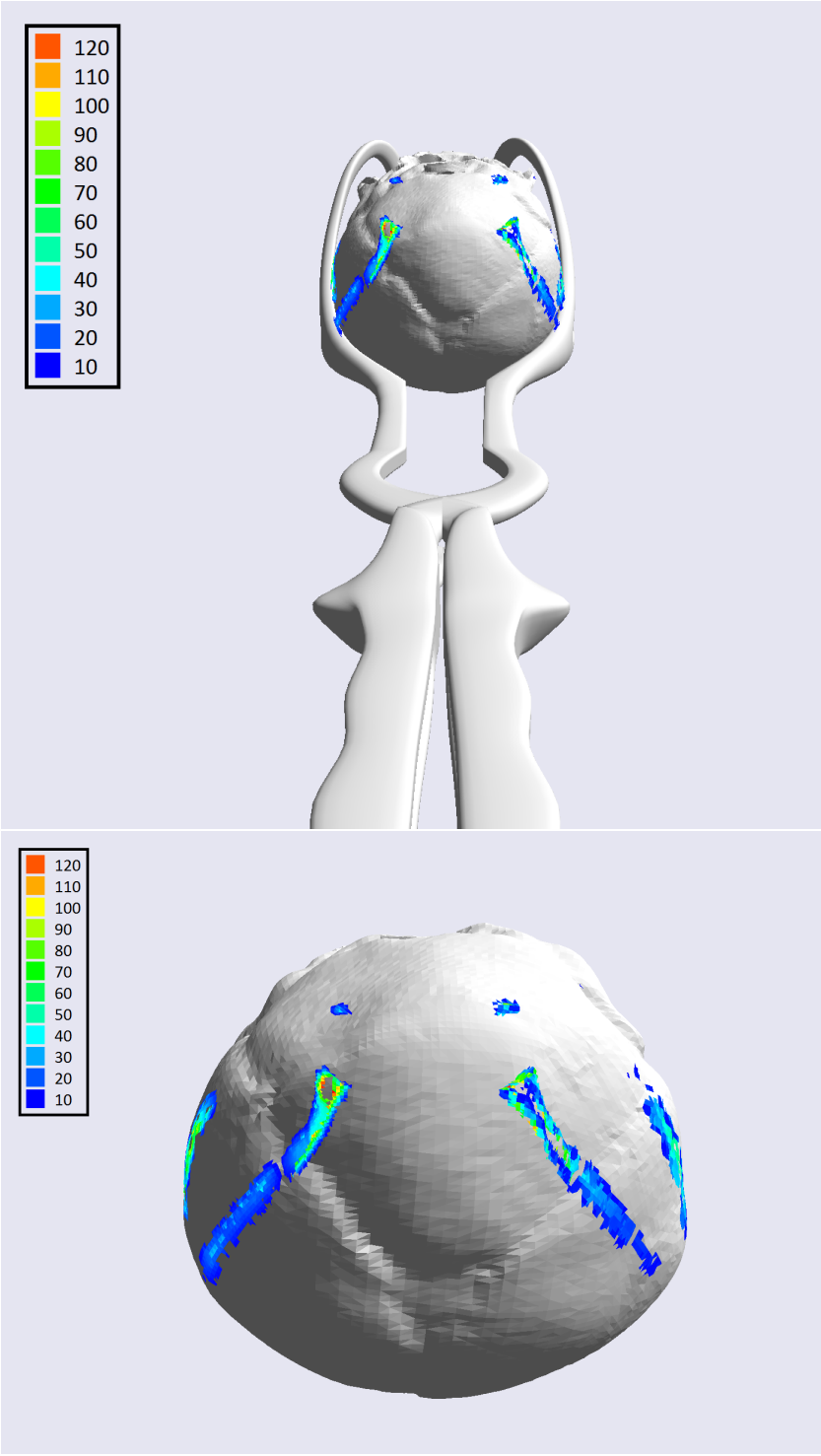

Figure 91: Examples of forceps to fetal skull placement definitions with changing states of forceps blade visibility. All visualised forces are in N.

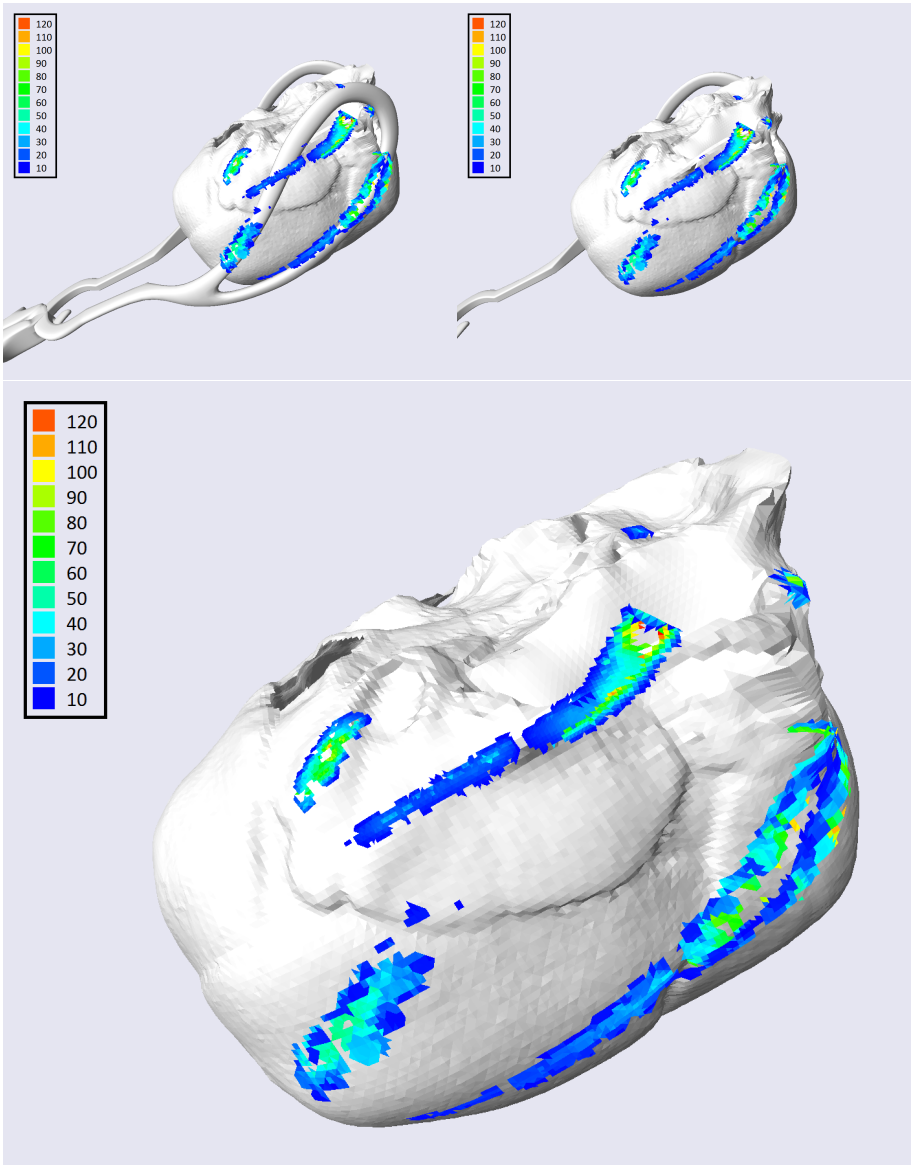

The resultant forces as shown in Figure 90 and Figure 91 were then used within a FEM simulation as shown in Figure 92 to analyse the effects of the forceps placement. The pre-calculation of forces caused by the application of forceps to the fetal skull allows for a simpler FEM simulation in which a static analysis of forces can be performed. This means that only the skull model had to be included in the FEM simulation without the need of a geometric model of the instrument (forceps or ventouse). Indeed the use of the latter would require a substantially more complex Finite Element Analysis (FEA), including collision detection between instrument and skull followed by a dynamic non-linear mechanical contact analysis. It is doubtful that the added complexity would result in more realistic simulation outcomes.

5.1.2 Experiments and results

As described in the previous section, analysing every possible position and forceps placement variation is beyond the scope of this study. The method described, developed and used would however be sufficient to model a significant number of possible variations.

The following variations will be reported on in this study;

- Symmetric placement of forceps as outlined in Figure 90.
- Asymmetric placement of forceps defined by a 20 degree rotation around y-axis of the fetal head.
- Two alternative symmetric placements which present the fetal head in positions varied by rotations around the x-axis of the skull in its occiput anterior vertex presentation. The variations were limited to a single rotation of +/- 20 degrees around the x axis of the skull as shown in Figure 93.

Figure 92: Forceps induced forces on the fetal skull within an Finite Element Model analysis environment. The bright yellow marks on the skull correspond to the coloured marks visualised in Figures 90 and 91.

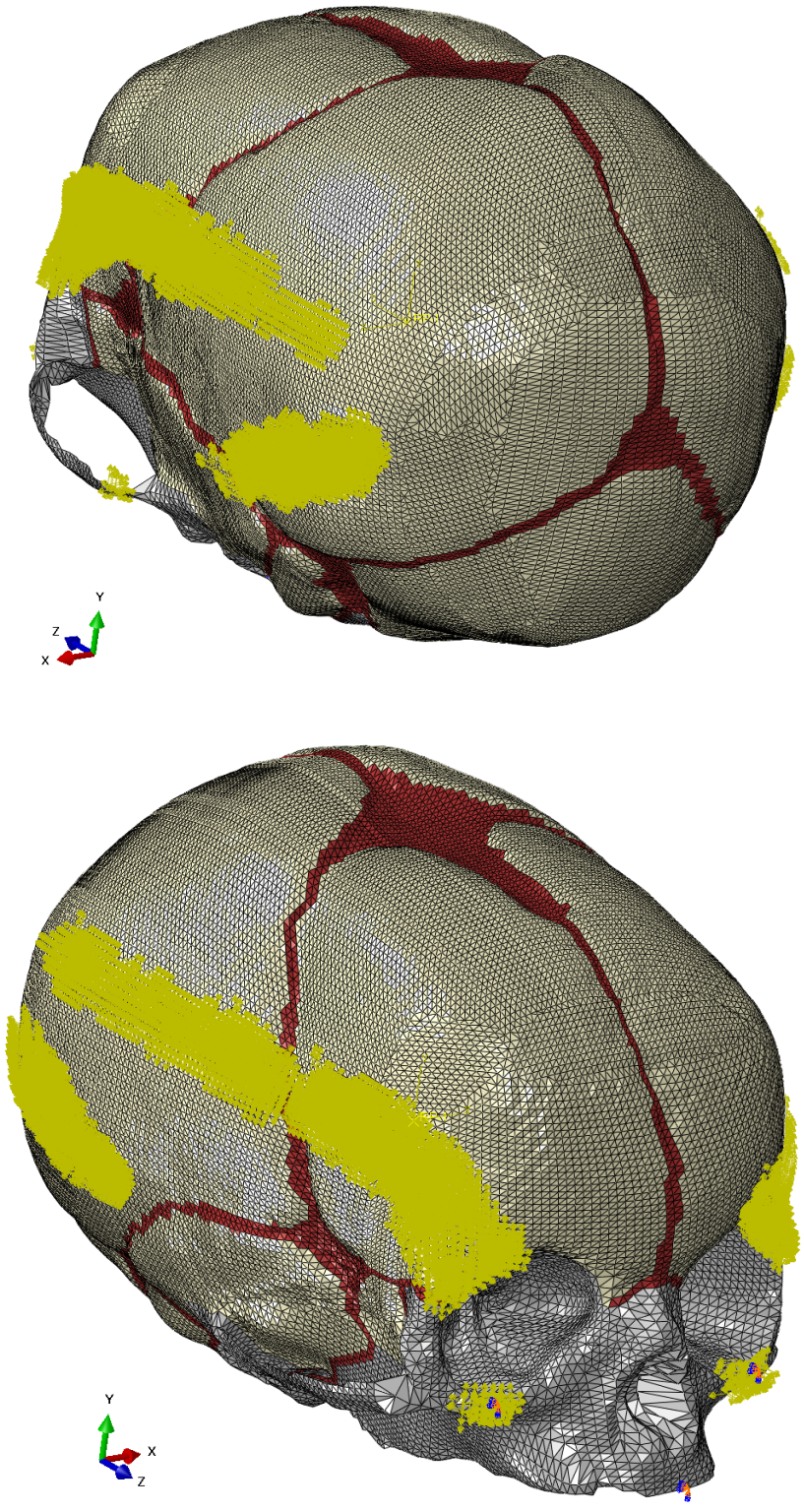

Figure 93: Variations of the fetal head around the central x-axis when undergoing the application of forceps. Left; Over-rotated. Middle; Correct. Right; Under-rotated. Contact forces are visualised in N using the same scale as noted in Figure 90.

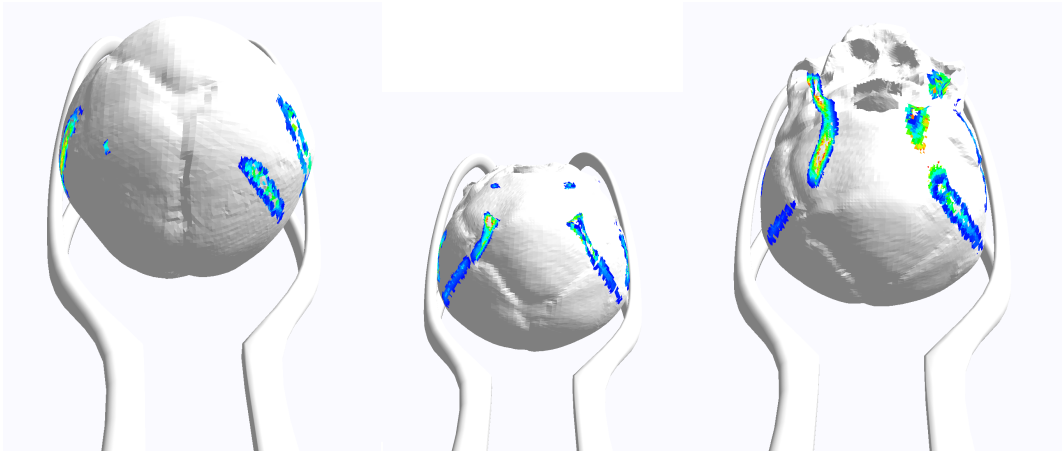

Table 13: Outcomes of the application of forceps to the fetal skull. U; Magnitude of deformation. S; von Mises stress. S12; Shear stress. Deformation U is in mm, stresses are in N/mm^2.

Experiment dscription	U	S	S12
"Correct" Symmetric placement	2.635	21.2	5.366
Symmetric placement, over-rotated skull	3.917	24.65	10.22
Symmetric placement under-rotated head	5.227	26.5	12.01
Asymmetric placement	3.653	32.84	17.8
Slightly under-rotated ROT	2.839	22.61	6.083
Slightly over-rotated ROT	2.802	23.19	5.998

- Head presentations of right occipital transverse variations as shown in Figure 94.

5.1.3 Discussion of results

The six specified forceps placement variations were carefully chosen to represent realistic scenarios that may occur during an intervention. Of these placement variations "correct" symmetric placement and asymmetric placement provide the clearest empirical evidence of the implications of bad forceps blade orientations.

Figure 94: Right occipital transverse presentations of the fetal skull upon which the forceps were placed. Contact forces are visualised in N using the same scale as noted in Figure 90.

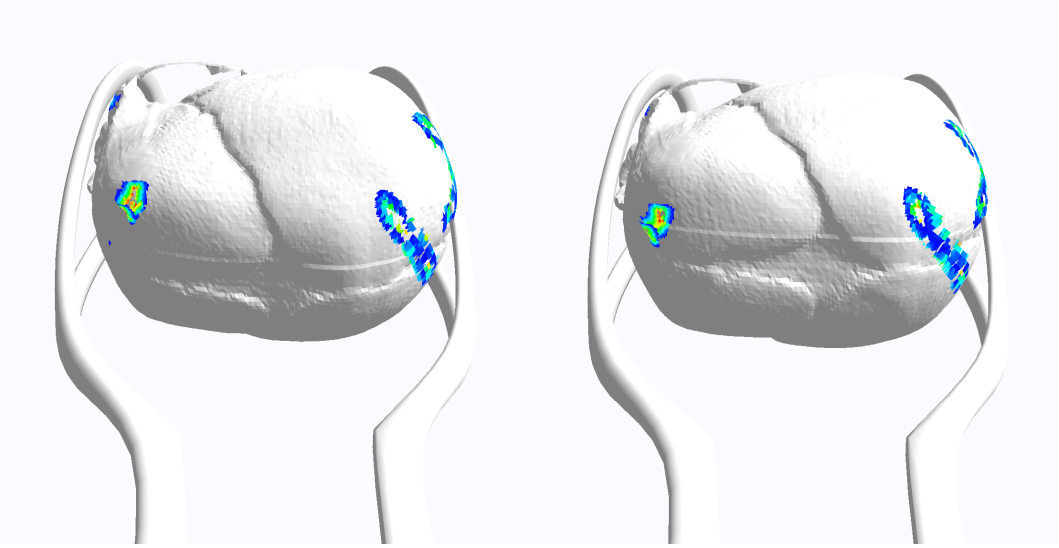

The first clear implication of incorrect placement is the increase in deformation magnitude. In the case of pure asymmetric placement the deformation magnitude evaluated to over 38% more than what was seen in the correct symmetrical case. It is important at this stage to bring attention to all "incorrect" variations as they all show deformation magnitude values that are higher than what is considered in this study to be the best case. Another interesting point of note is that the asymmetrical placement does not result in the highest U values. Symmetric placement on an under or over rotated skull both result in more deformation and in the case of under-rotation of the fetal skull the magnitude of deformation is over 98% more than that seen in a correct symmetrical case. It is at this stage that attention must be brought to the von Mises and shear stress values observed during the placement variations. It is in the opinion of the author that it is in fact the increase in these values that shows the real danger of incorrect forceps placement. The anatomy of the fetal skull as was outlined previously has clear indications that large deformations can be tolerated by the fetal skull

structure. However what the stress values obtained by these experiments show is that deformations forced upon the skull following the incorrect application of forceps greatly increases the stress that the thin and fragile sections of skull bone have to withstand.

The implications of greatly increased stress values as obtained by this study are clear and serious; In the case of hard structures such as the fetal skull bone there is increased risk of fracture. The skull model outlined has no "soft" components such as skin, but the consequences of this increase in stress can be assumed to have serious implications on those aspects of the fetal head. Risk of permanent scarring and haematomas is certain to be higher than if the forceps blades were applied correctly. It is however the internal structures such as the blood vessels attached to the inner parts of the skull that may be at an increased risk of being damaged. Unfortunately, analysing this is beyond the scope of this study.

5.2 Ventouse

Unlike the forceps placements, the positional placement of the ventouse cup is more restricted due to its topology and the need to retain a strong seal to the fetal head. The application of these variant are discussed in detail here.

5.2.1 Analysis of applied force

The ventouse interaction with a fetal head can be described in two separate processes:

1. Static - The pressure within a suction cup must decrease sufficiently in order to form a vacuum, creating a "negative" pressure on the internal area of the suction cup. This change in pressure also results in an area of positive contact pressure around the edge/rim of the suction cup.

2. Quasi-Static - Once the suction cup has been attached, assuming an idealised seal which stops any pressure reduction (in reality the seal is imperfect and has to be maintained by the operator with additional air reduction), the system could be considered to be in equilibrium. This state changes the moment the operator pulls the ventouse handle and applies traction to the fetal head via the attached suction cup. The application of this traction force is slow (low velocity, to avoid unplanned de-cupping and potential injury) and therefore can be considered to be static.

Calculating the extent of pressure within the suction cup and the resulting contact pressure exerted by the cup rim on the fetal head is heavily dependant on the size and topology of the suction cup and the materials used for it. In cases where a rigid (plastic/metal) suction cup is used, the edge area can be calculated by the following equation (and visualised in Figure 95):

$$A = \frac{\pi}{4}\left(d_0^2 - d_i^2\right) \tag{39}$$

where d_0 denotes the external diameter of the VE suction cup and d_i is the internal diameter of the VE suction cup as shown in Figure 95.

For this study, the ventouse dimensions and topology were modelled after the Clinical Innovations Kiwi hard plastic cup ventouse (KVE) as shown in Figure 11. The dimensions of the suction cup in this case measures as $d_0 = 55mm$ and $d_i = 50mm$. Substituting the variables in the above equation yields $A = 4.12cm^2$.

The area A of the cup rim can then be used to represent the distributed downwards (towards the fetal head) force F_p, which would be aligned opposite to the normals of the topology in contact with the cup. In this study the normals would be that of the triangles that make up the fetal skull model. The suction

Figure 95: Rigid suction cup to fetal head contact area. d_0; External diameter of the VE suction cup in mm. d_i; Internal diameter of the VE suction cup in mm.

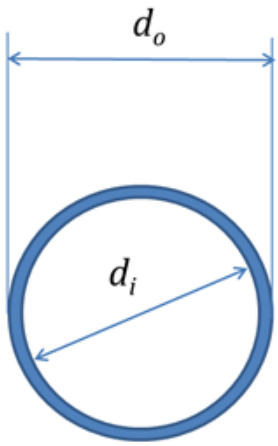

pressure p, will influence all of the topology within d_i of the suction cup rim contact. As stated earlier, the resulting state at this stage will be that of an equilibrium, with F_p depressing the underlying triangle topology with the same force as the total exerted force in the opposite direction by p as shown in Figure 96. As discussed in Section 2.2.2, the vacuum pressure used for the experiments was set to 500 mmHg which corresponds to $p = 66.7kPa$.

The traction force, F_T (as shown in Figure 97), exerted by the operator using a Kiwi vacuum extractor under 66.7kPa of vacuum pressure is 131N when considering the internal cup area of $19.6cm^2$. The force is limited to 131N, because any force bigger than this will pull the suction cup off the fetal head. As discussed in Chapter 2, the typical traction forces applied to a VE extraction do not generally exceed 100N and this is the value adopted for the F_T in the experiments as the maximum traction force [63].

Figure 96: Rigid suction cup applied to a fetal head, resting in a state of vacuum induced equilibrium. p; Suction pressure in kPa. F_p; Distributed downwards force in N.

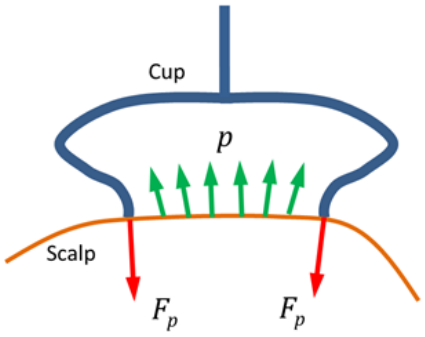

Figure 97: Rigid suction cup applied to a fetal head whilst influenced by a traction force p; Suction pressure in kPa. F_p; Distributed downwards force in N. F_T; Traction force in N

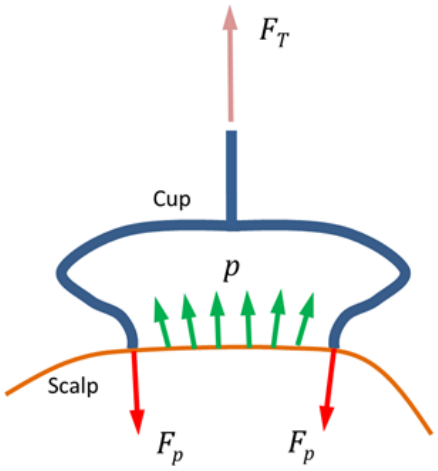

Figure 98: Correct placement of the vacuum extraction suction cup upon the fetal head. The shaded area indicates where the VE suction cup will have an influence on the skull. Red; Effect on cartilage. Black; Effect on fontanelles.

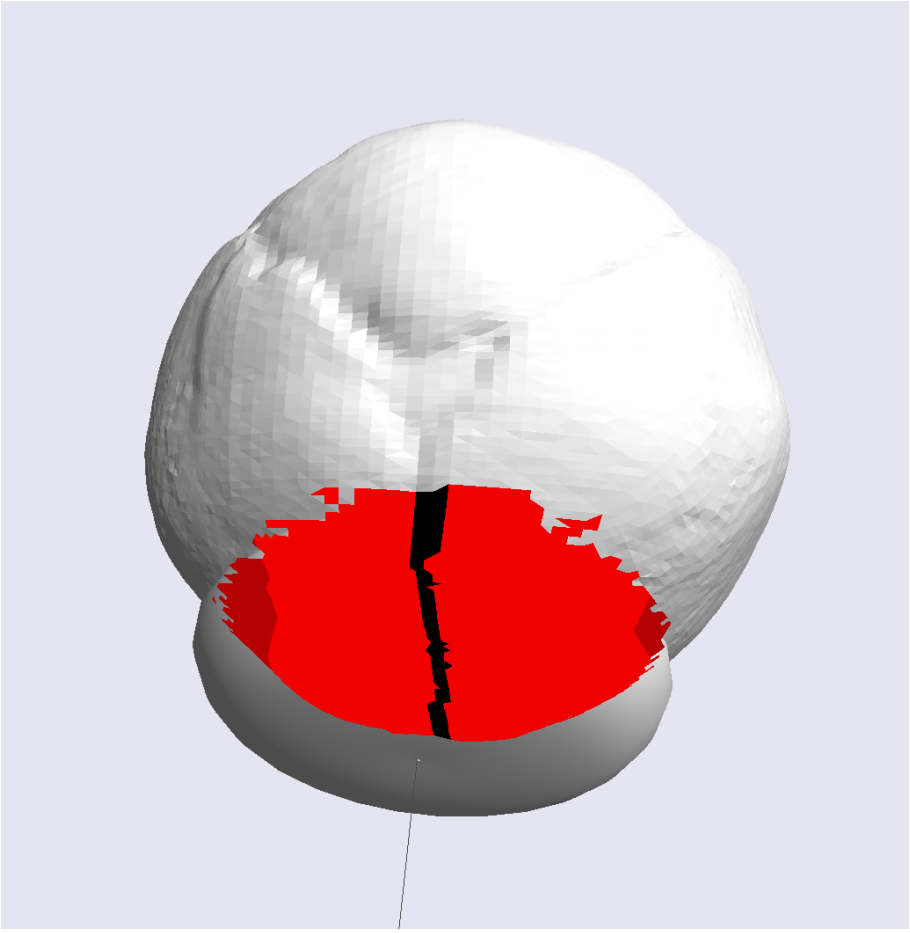

5.2.2 Placement variations

The experiments involving VE placement were defined as follows:

- One correct position as demonstrated by Figure 98.
- Two incorrectly positioned suction cups with a likelihood of causing damage to the fetal head as shown in Figure 99.

Figure 99: Incorrect placement of the vacuum extraction suction cup upon the fetal head.. Top; Suction cup placement upon the anterior fontanelle. Bottom; Suction cup placement upon the posterior fontanelle. The shaded area indicates where the VE suction cup will have an influence on the skull. Red; Effect on cartilage. Black; Effect on fontanelles.

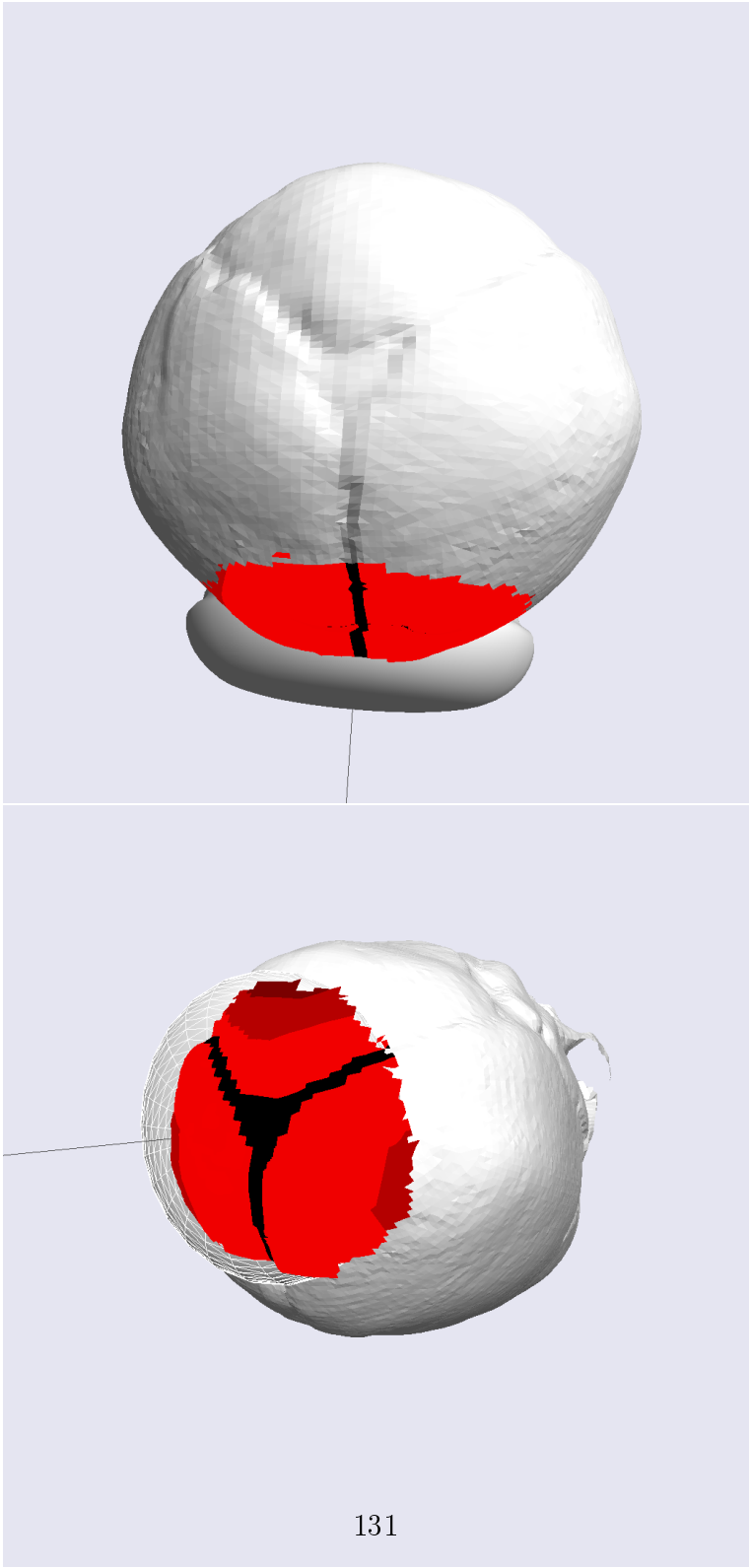

Table 14: Effects of ventouse application to the fetal head. U; Magnitude of deformation. S; von Mises stress. S12; Shear stress. Deformation U is in mm, stresses are in N/mm^2.

Experiments	U	S	S12
Well placed	3.061	26.93	10.75
Incorrect placement on posterior fontanelle	6.243	95.1	34.59
Incorrect placement on anterior fontanelle	11.27	113.4	42.87

Experiment outcomes

5.2.3 Discussion of results

The first very interesting outcome of analysing ventouse placement is the relatively comparable values of deformation magnitude, von Mises stress and shear stress. This seems to confirm the "correctness" of the symmetrical forceps placement outlined in this chapter. The similarities between the deformation and stress values end there however as incorrect placement of the suction cup shows major increases of the respective measures which far exceed those demonstrated during forceps applications. The fact that these values are so high makes it difficult to compare directly to those obtained for the forceps case. One major factor in this case is that an incorrect placement in the VE case means that a lot of pressure will be applied to the relatively soft anterior and posterior fontanelles which will far more readily deform than the bony structures of the skull that the forceps interact with.

The lack of a direct comparison with the effects on the skull by forceps as opposed to VE does not make these results less relevant. In fact this enforces what is generally understood within Obstetrics; vacuum cup placement over the anterior and posterior fontanelles should be avoided.

6 Conclusions and future work

The first main contribution of the research presented in this thesis was the development of an improved model of fetal head moulding. The model was based on previous work by Lapeer [19]. Improvements included the addition of hydrostatic fluid elements (HFEs) to model the intra-cranial pressure (ICP). The latter makes the model more realistic as compared to the 'hollow' model by Lapeer since it makes the inner volume of the skull cavity incompressible. In reality this is due to the presence of the brain (which is also incompressible) and fluids such as the CSF (cerebrospinal fluid) and blood flow. Additionally, the model is numerically more stable due to the hyperelastic fontanelle elements being supported by the ICP and as such do not undergo excessive rotations which are at the cause of instabilities.

The second contribution of the research is the assessment of the effect that incorrect placement of obstetric instruments has on fetal head moulding in general and more specifically on certain critical areas of the fetal scalp. Two instruments were tested:

- Obstetric forceps: symmetric or correct placement was compared to various degrees of incorrect (asymmetric) placement.
- Ventouse: correct placement (between anterior and posterior fontanelle) was compared to incorrect placements such as on top of the large anterior fontanelle and lateral placement on the fetal scalp (rather than symmetric).

The general findings were that incorrect placement of either instruments causes significantly larger deformations as compared to correct placements. For the obstetric forceps, it was also observed that significantly higher shear stresses occurred in the case of asymmetric placement. In summary, the work presented in this thesis is a step forwards in the effect of normal childbirth and instrumental

intervention on the fetal skull. The developed models can be used in a clinical context for various applications:

- Training in the application of obstetric forceps and ventouse
- Assessment of damage after incorrect application in a real scenario
- The fetal head moulding model can also be used as part of a larger childbirth simulation (to predict adverse outcomes) to add realism.

The former applications need further work and as such fall under the umbrella of future work. From a purely technical point of view, there are still a number of improvements that can be made to the proposed models:

- Although a more stable model of fetal head moulding has been developed, there are still a number of issues with respect to this phenomenon that remain unclear. One of these is the effect on the different diameters, e.g. the SOBD which showed contradictions under different conditions. Perhaps a more robust metric of quantifying fetal head moulding should be considered which goes beyond assessing diameters but includes curvature and 3D shape deformation.
- Dynamic contact FE analysis would be bound to provide more realistic results for either the fetal head moulding model and instrument analyses as this is what happens in reality, i.e. the fetal head in contact with the uterine cervix and obstetric forceps blades in contact with the fetal head. However, care has to be taken as more complex models are bound to be less stable and also more sensitive to small deviations in input data potentially yielding less reliable results.

Appendix A

```
import bpy import bmesh import math from mathutils import Vector, Matrix
   def cross(v1, v2):  return [ v1[1]*v2[2] - v1[2]*v2[1], \ v1[2]*v2[0] - v1[0]*v2[2],
\ v1[0]*v2[1] - v1[1]*v2[0] ]
   def dot(v1, v2):  return v1[0] * v2[0] + v1[1] * v2[1] + v1[2] * v2[2] def length(v):
return math.sqrt(dot(v, v))
   def distance(v1, v2):  return length([v1[0] - v2[0], v1[1] - v2[1], v1[2] -
v2[2]])
   def normalize(v):  l = length(v) return [v[0] / l, v[1] / l, v[2] / l]
   def mul(v, s):  return [v[0] * s, v[1] * s, v[2] * s]
   def div(v, s):  return mul(v, 1/s)
   def createPlane(normal, d):  bpy.ops.mesh.primitive_plane_add(enter_editmode=False,
radius = 100.0) #rotation=(angles[0], angles[1], angles[2]) ob = bpy.context.object
ob.name = 'Plane' initial = [0, 0, 1]
   initial_dot = dot(initial, normal)
   angle = math.acos(initial_dot) axis = cross(initial, normal) ob.matrix_world
= Matrix.Rotation(angle, 4, axis) * \ Matrix.Translation([0, 0, d]) ob.select =
False return ob
   def abs(val):  return val if val >= 0 else -val
   #createMeshFromPrimitive()
   normal = normalize([0, 0.65, -1])
   threshold = 0.1
   verts = bpy.context.active_object.data.vertices
   def find_diameter(d):
   onplane = []
   for idx, vert in enumerate(verts):  v_dot = dot(normal, vert.co) dist = abs(v_dot
- d)
   vert.select = False
   if dist < threshold:  onplane.append(vert)
   # trigger viewport update bpy.context.scene.objects.active = bpy.context.scene.objects.activ
   center = [0, 0, 0]
```

```
    for vert in onplane:  center[0] += vert.co[0] center[1] += vert.co[1] center[2]
+= vert.co[2]
    center = div(center, len(onplane))
    avgDist = 0
    for vert in onplane:  vert.select = True dist = distance(vert.co, center) avgDist
+= dist
    avgDist /= len(onplane)
    diameter = avgDist * 2 return diameter
    bpy.ops.object.mode_set(mode='EDIT') bpy.context.tool_settings.mesh_select_mode
= (True, False, False) # force verts
    bpy.ops.object.mode_set(mode='OBJECT')
    plane = createPlane(normal, 50)
    def dial_ratio(diameter):  return diameter / 91.9
    min_d = 1 max_d = 59.8 steps = 100
    #for i in range(0, steps):  # d = min_d + (max_d-min_d) * i / steps # diameter
= find_diameter(d) # dial = dial_ratio(diameter) # # print("%f, %f, %f" % (d, diameter,
dial)) # max_diam = -9999999
    def handler(scene = None):  global max_diam global plane d = length(plane.location)
diameter = find_diameter(d) if max_diam < diameter:  max_diam = diameter print(diameter)
print(d) if handler not in bpy.app.handlers.scene_update_pre:  bpy.app.handlers.scene_update_pre
```

Appendix B

Internal Vaginal Examination Trainer

An Internal Vaginal Examination (IVE) trainer prototype has been developed. This has undergone clinical trials at Southmead Hospital in Bristol for a year. The prototype had to address a number of issues that would allow for clinical use and rapid development:

- It had to be easy to set-up and use.
- It had to "feel" correctly in a clinical context.
- It had to provide a way of easily adjusting the material properties and changing whole objects within any given simulation scene.
- It had to provide a way of leaving feedback regarding system settings and general comments without detracting from the use of the trainer.

Haptic interface

The main aspect of the IVET prototype was the interaction between the physical and virtual environments. To achieve this interaction, a Phantom Omni haptics device produced by SensAble technologies (see Figure 100) was used for the development of the prototype.

The Phantom Omni device was chosen for a number of reasons:

- Price - The per unit cost was considered to be low given the level of performance provided by the device. Alternative haptics devices that were marginally better (more force, higher frequency of feedback) were many times more expensive, making the price point for the prototype prohibitive.

Figure 100: A SensAble Phantom Omni haptics device

- Programmable - The Omni comes with 3 different APIs that allow various degrees of control over the haptic feedback.
- Multiple Degrees of Freedom - Motion can be resisted in multiple directions, making haptic feedback more realistic.
- Robust build - This is an important factor in the context of Obstetric simulators/trainers, because at times there may be a lot of force exerted on the device by the operator. The ability to withstand such use was deemed an important consideration.

In its standard configuration, the Omni comes with a pen like handle that is held by the end user and is then used to interact with the virtual environment. For the general use case the device is aimed for, this type of interaction is sufficient. In the case of simulating an internal vaginal examination, the act of holding the hand in the same way as it would be held whist using a pen caused issues with the perceived feel of an object. In reality the hand could never be held in such a position due to the restricted amount of space provided by the vaginal canal.

In most cases, two fingers would be inserted and used to feel the current cervix dilatation and fetal head orientation (the orientation is judged by the ridges of the anterior or posterior fontanelles). A similar issue has been resolved in the psat by a bovine simulator called the "Haptic Cow" [114]. In that case it was found that provided the user cannot see their own hand, attaching the middle finger of the hand to a haptic device was enough in most cases to trick the user into thinking that they are "feeling" with their whole hand. To attempt this approach, the Omni had to be modified. The pen like handle can be removed exposing a 3.5mm jack (without making permanent alterations to the device) and this was the first method of alteration that was attempted. An additional attachment in to which two fingers could be inserted was created to attach to the exposed jack (see Figure 101).

This approach was an improvement over the original pen handle interface, but was deemed insufficient for the purposes of the trainer. The were a number of reasons for this:

- Materials - The device was made largely of a clay like material which was very rigid and heavy once set. This meant that users with different sized fingers would have issue using the interface, but more importantly, the rigidity meant that the tips of the fingers did not "feel" like they were touching anything. This was an important shortcoming as the examination depends on the ability to discern small details with the tip of a finger.

- Center of gravity - the size and weight of the new interface meant that it was offset as far from the hinge as the pen handle was. The problem with this became apparent very quickly, as interacting with anything that had resistance to touch was very awkward due to the handle rotating around the hinge. This rotation made resisting any haptic force very difficult.

Figure 101: An alternative physical Omni device interface used to hold two fingers

The limitations of the interface outlined above made it very clear that the Omni device would need to be altered further (in irreversible ways) if the correct user interaction was to be achieved. The biggest problem was the jack to which the pen handle was attached; With it in place, there was no way to resolve the centre of rotation problem. Removing the jack resolved this problem and also provided a simple solution to the interface problem. By removing the jack, the tip of the "pen" which was directly under the hinge provided a hollow orifice in to which a finger could be placed (Figure 102 shows the modified Omni device).

To allow for multiple users of the device, rubber thimbles were used to provide direct contact with the device. This allowed for better traction and grip, whilst also using differently sized thimbles as an easy way to adjust for different finger sizes.

Physical constraints

The haptic interface described earlier is one of the most important aspects of the trainer, but after some testing and feedback from clinical staff, it became clear that a standalone haptics device would not be sufficient. This was due to the lack of constraints that could be placed upon the haptic device. In the Haptic Cow, the constraints placed upon the user were very limited due to the amount of physical movement the environment allowed. In fact most of the limits were imposed by the shoulder dexterity of the operator and most of the interaction involved relatively large sweeping motions to try and determine which organ was being felt. This could not be the case in the IVE trainer due to the lack of such space and the fact that in reality only the clinician's finger movements are constrained. To resolve this issue, a physical model of a vagina used for episiotomy training was employed. Figure 103 shows the vaginal model in situ within a box and reinforced by structural foam (the foam can be seen in Figure

Figure 102: A SensAble Phantom Omni haptics device after physical modifications

Figure 103: Haptics device in situ behind the vaginal model

105).

This setup resolves the lack of finger and hand constraints and allows the virtual haptics space to match that of a real working area that a clinician would have. The haptics device could then be placed behind the vaginal model and secured into place after adjustment and calibration so that the physical properties of the user could be matched. Figure 105 shows the interaction that a user would expect to have.

Virtual topology

Once the physical interface and constraints were finalised, the virtual interface and body part representations had to be developed. The IVE problem domain is fairly limited, so the number of things that could be interacted with was limited to:

Figure 104: Another view of a haptics device in situ behind the vaginal model

- Fetal head
- Cervix
- Vaginal wall

Unlike the fetal head model described in Chapter 3, the models outlined above had to instead "feel" anatomically correct. This effect had to be achieved with the use of various material settings (friction, hardness, etc.) and a topology that would trick the user into thinking that they are touching the correct part of the anatomy. The models were developed using an iterative process over a period of 3 days and nights within the Gynaecology and Obstetrics ward at the Southmead Hospital in Bristol. Models were first created and then constantly adjusted following feedback from clinical staff within the department and ward. The resulting models of the vaginal canal and the cervix can be seen in Figure 106 and Figure 107.

Figure 105: User interaction with the haptics interface through the vaginal model

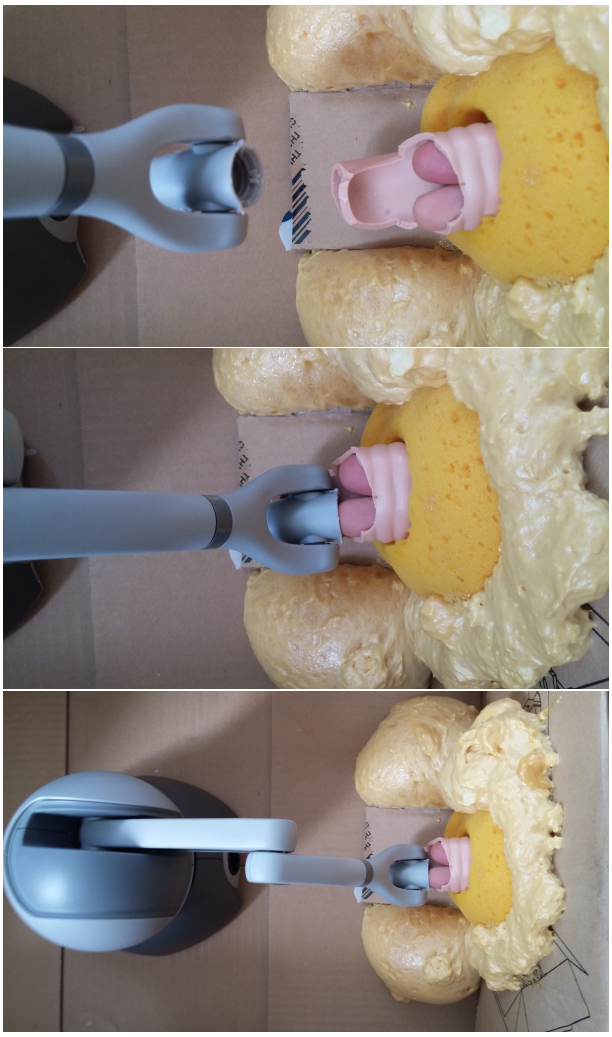

Figure 106: Virtual haptic model of the vaginal wall

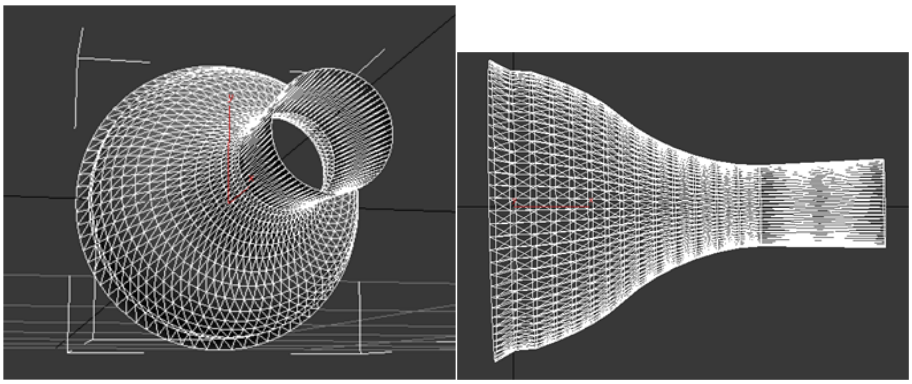

Figure 107: Virtual haptic model of the uterine cervix

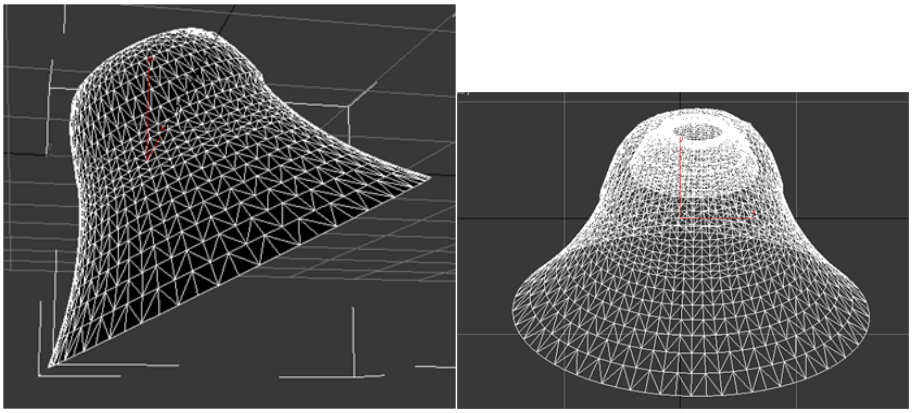

The initial model of the fetal skull was the same as that used in Chapter 4, but it was determined that for use in a haptic environment, the topology was not sufficient. The biggest problem was the lack of definition (depression) of the fontanelles, making it very difficult to judge the orientation of the head when using only touch. The final representation of the skull was in fact a sphere with very deep valleys used to represent the anterior and posterior fontanelles and sutures. The sphere was also of a much higher resolution than the original fetal skull. This increase in resolution was largely driven by the fact that users could sometimes feel the edges of individual triangle elements and would mistake them for the sutures.

Ease of set-up and use

The system was set up in a simulation room within the Bristol Southmead Hospital's Gynaecology department. It included a dedicated PC and haptics device within a custom made enclosure. A step by step user manual was provided to assist users. This allowed the system to be accessed and used by anyone who was allowed within the department (Doctors, Midwives, etc.).

Correct "Feel"

In order to achieve the right feel of the objects within a scene, a number of approaches have been used:

- Physically inaccurate models were developed (as shown in section 2.1.1). These were created within the University of East Anglia (UEA) and then altered over a number of days and visits within the Southmead Hospital with a lot of input from medical staff.
- A way of adjusting material properties of objects has been developed. This allows for quick and easy adjustment in haptic properties of any object currently loaded by the system.

Material and Object adjustments

The adjustment of material properties could be done in one of two ways. The image shown above was the simple quick access way. The other method was to manually edit an xml file to change and hard code material properties there. An xml scene file system was implemented for this project to aid in rapid prototyping and development. The scene file would contain information on the models within a scene, the materials and their haptic properties. This approach allowed for new scenes and models to be developed at the UEA campus and then simply sent over the internet to Bristol for use by the medical staff there.

Easy Feedback

To allow users to leave their feedback on the system without resulting to questionnaires every time they wanted to use the system, a feedback element was incorporated into the user interface. This allowed the user to enter some basic information about themselves (occupation, years of experience, etc.) and then

simply click the submit button which would store that information alongside the current system and material settings for analysis later.

Appendix C

Polynomial Coefficient Values

The polynomial coefficients outlined in Table 15 are used to produce the graphs shown in Figure 75 and 76.

Fetal skull - Material and model properties

Additional views of the application of different materials to the fetal skull as shown in Figure 108 and section thicknesses as shown in Figure 109.

First stage of labor - Hyperelastic fontanelle moulding

Table 15: Polynomial coefficients used during curve fitting

Order of polynomial							
2	-3.9323e-04	0.0131	0.9084				
3	-9.3317e-06	0.0005	-0.0074	1.0174			
4	-2.4448e-07	2.0109e-05	-0.0007	0.0084	0.965		
5	-8.1981e-09	9.8958e-07	-4.6328e-05	0.0008	-0.0054	0.9969	
6	-1.2826e-10	1.497e-08	-6.0316e-07	5.4823e-06	2.4864e-05	-0.0002	0.9878

Figure 108: Coloured sections of different materials defined on the fetal skull. X, Y and Z-axis oriented views (front and back) with orthographic projection. Grey is bone, white is cartilage and red denotes the fontanelles.

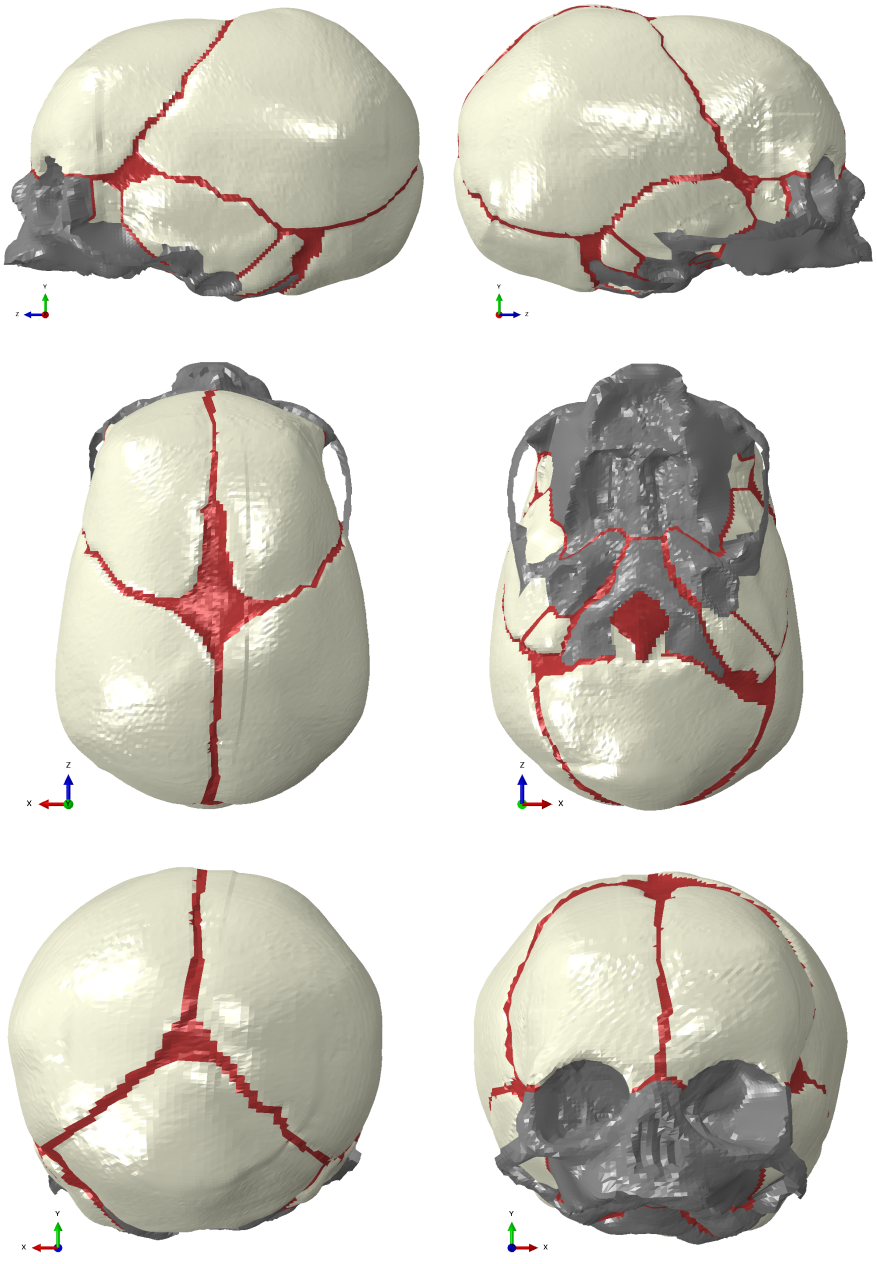

Figure 109: Coloured sections of different shell thicknesses in mm defined on the fetal skull. X, Y and Z-axis oriented views (front and back) with orthographic projection.

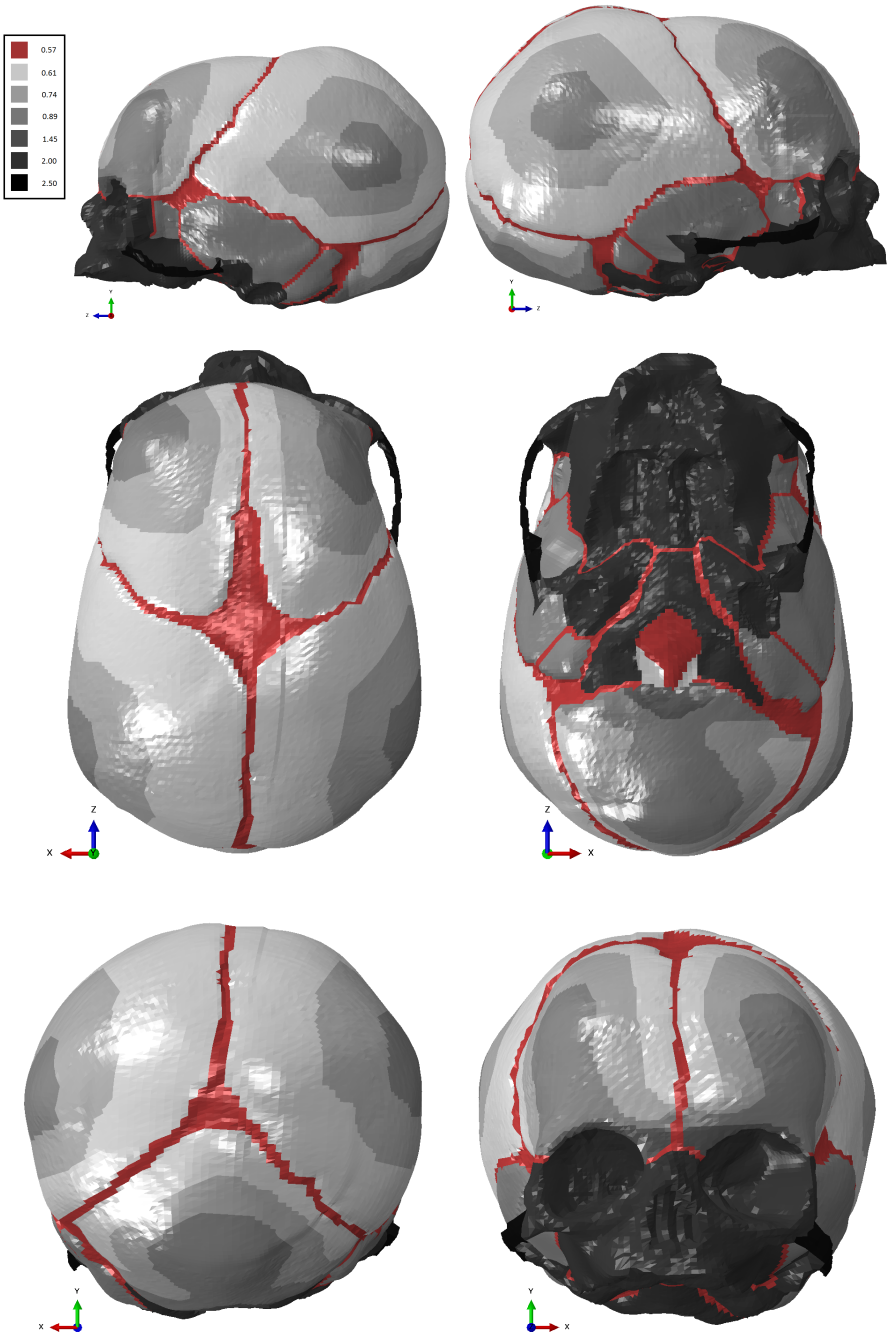

Figure 110: Fetal skull deformation when the fontanelles are defined to have hyperelastic material properties. Front and back edge oriented views in orthographic projection. Convergence completion at 63.5584% with the uterine cervix dilatation defined to be as 9cm with D1 and D2 values as defined by Lapeer [19]. U; Magnitude of deformation. S; von Mises stress. S12; Shear stress. Deformation U is in mm, stresses are in N/mm^2.

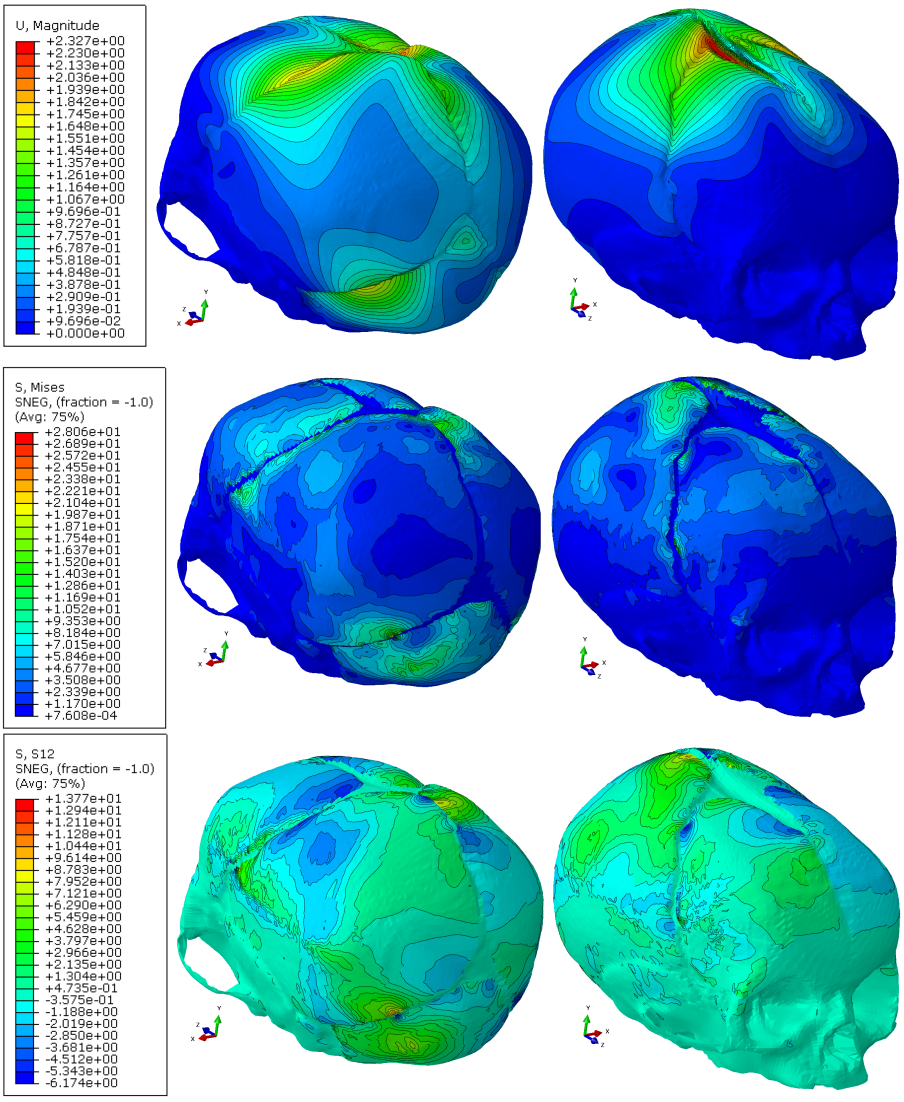

Figure 111: Fetal skull deformation when the fontanelles are defined to have hyperelastic material properties. Front and back edge oriented views in orthographic projection. Convergence completion at 95.7476% with the uterine cervix dilatation defined to be as 9cm with D1 and D2 values as defined by the study described in this thesis. U; Magnitude of deformation. S; von Mises stress. S12; Shear stress. Deformation U is in mm, stresses are in N/mm^2.

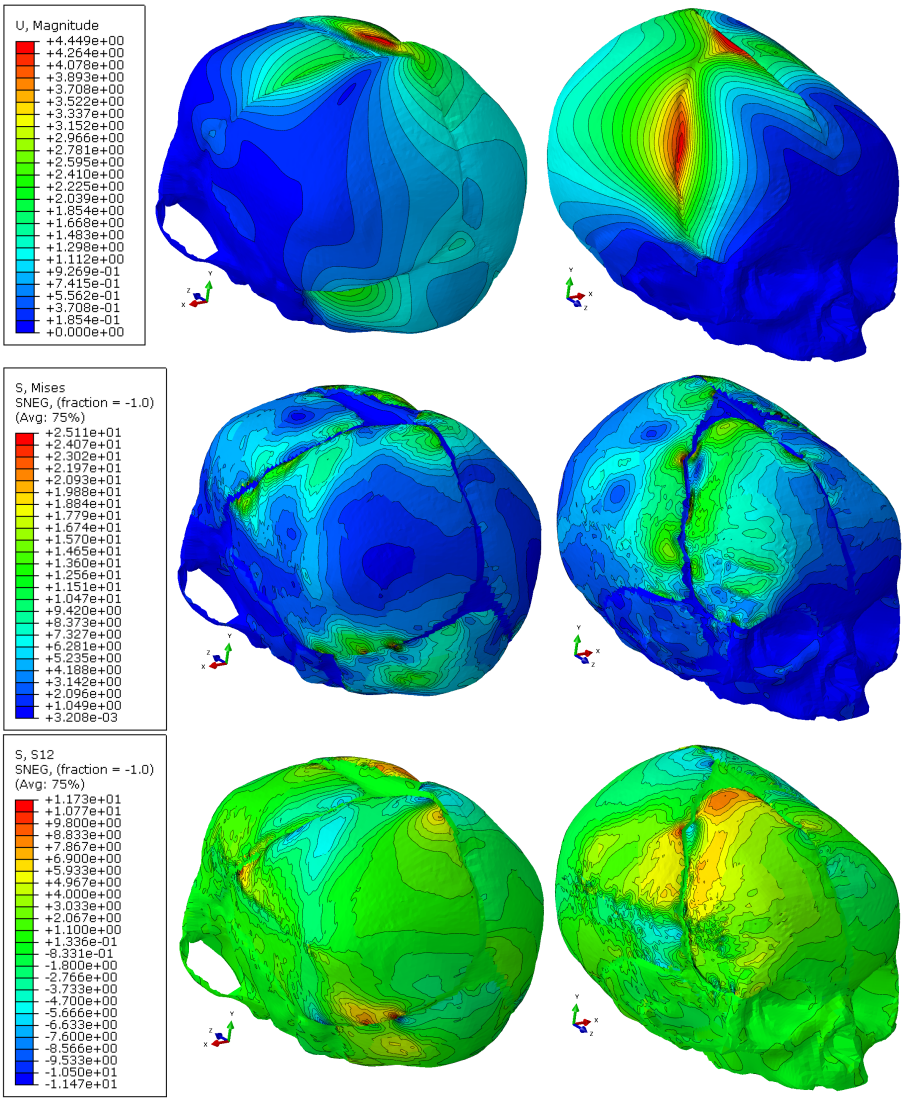

Appendix D

An introduction to Finite Element Analysis concepts

Time-dependent and space-dependent problems that need to be described in terms of the laws of physics are generally expressed using partial differential equations (PDEs). There are many problems and geometries that are very difficult to solve with analytical methods. Geometrical complexity often makes the use of analytical methods sub-optimal as approximations of the equations must be constructed and this can lead to inadequate solutions. Finite Element Analysis (FEM) is a very convenient tool for such geometrically complex problems. This chapter aims to provide a simple introduction into some aspects of FEM, but stops short of going into the full theory which is vast and a detailed explanation of which is beyond the scope of this thesis. Please consult FEM literature [115, 116, 108] to further any concepts mentioned in this appendix.

The use of FEM can be generalised into three categories:

1. Preprocessing
2. Solution
3. Postprocessing

Preprocessing

This stage is critical to the overall accuracy of the end result because this is the point where all properties are defined. The category can be broken down as follows:

- Define the geometry of the problem domain. This may involve defining element properties such as length or area and creating a well ordered mesh to ensure the most accurate results.
- Select appropriate element types such as those shown in Figure 112 and Figure 113.
- Define material properties. This can be entering the material constants or creating subroutines that define such constants programmatically.
- Define physical constraints such as boundary conditions and loads.

Solution

Compute unknown values of the primary field variables and then use them by substitution to compute other derived variables such as reaction forces, stresses, etc.

Postprocessing

This stage is all about sorting, plotting and visualizing the results of the solution. The results can then be validated against other data.

The primary characteristics of an element in FEM are expressed with a stiffness matrix. This is because for any structural element this matrix contains the geometric and material behaviour information that defines the element resistance to deformation when subjected to any type of loading. This idea can be best explained by a simple example:

FEM example: Linear spring as a finite element

This example has been adapted from a lecture in Finite Element Analysis (FEA) theory presented at the engineering department of the University of Victoria [34].

Figure 112: Examples of types of first-order 2D and 3D linear elements used in Finite Element Analysis. Source: COMSOL [33]

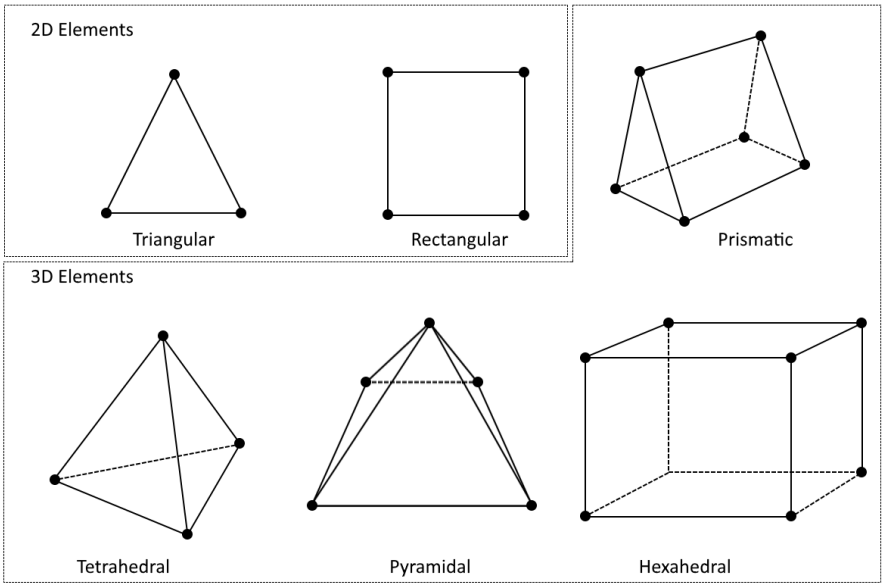

Figure 113: Examples of types of second-order 2D and 3D quadratic elements used in Finite Element Analysis. All points are present in Lagrangian elements but removal of the grey points would produce serendipity elements. Source: COMSOL [33]

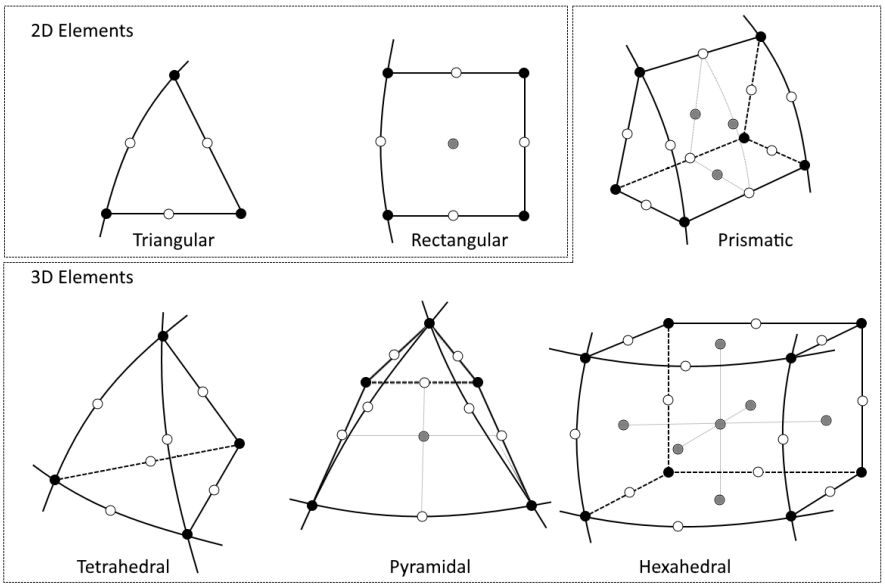

Figure 114: Top; A linear spring element with nodes, their displacements and forces. Bottom; Load-deflection curve. Source: UVic [34]

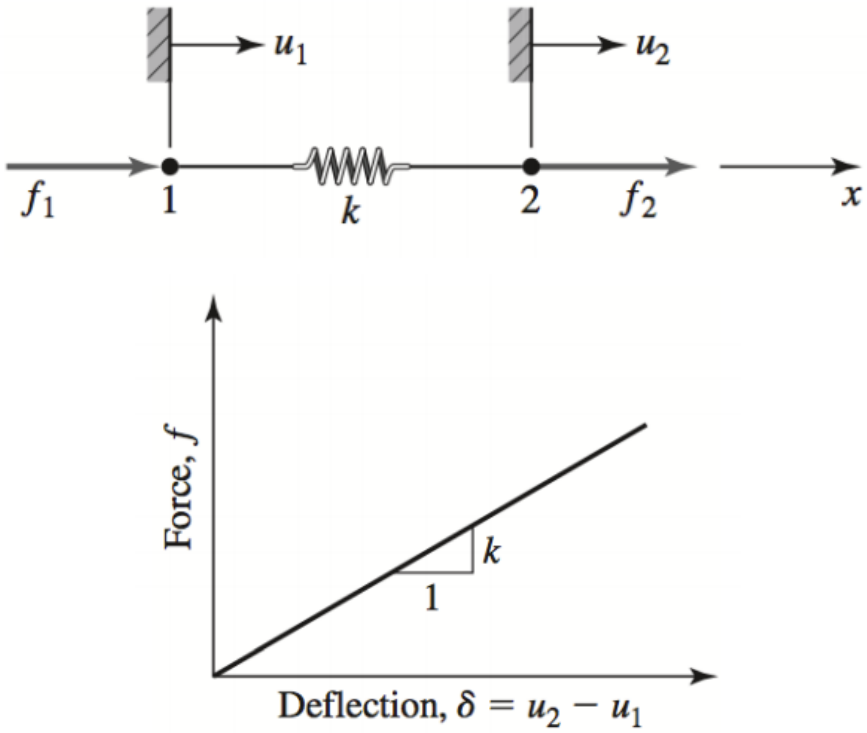

Consider a linear elastic spring (as shown in Figure 114) capable of supporting axial loading only, with the elongation and contraction of the spring being directly proportional to the applied load.

Assuming that both of the nodal displacements as shown in Figure 114 are zero when the spring is undeformed, then the net spring deformation is given by

$$\delta = u_2 - u_1 \tag{40}$$

and the resultant axial force in the spring is

$$f = k\delta = k\left(u_2 - u_1\right) \tag{41}$$

For equilibrium:

$$f_1 + f_2 = 0 \tag{42}$$

The applied nodal forces are

$$f_1 = -k\left(u_2 - u_1\right) \tag{43}$$

$$f_2 = k\left(u_2 - u_1\right) \tag{44}$$

Which can then be expressed in matrix form as

$$\begin{bmatrix} k & -k \\ -k & k \end{bmatrix} \begin{Bmatrix} u_1 \\ u_2 \end{Bmatrix} = \begin{Bmatrix} f_1 \\ f_2 \end{Bmatrix} \tag{45}$$

or

$$[k_e]\{u\} = \{f\} \tag{46}$$

meaning that the stiffness matrix for one spring element is

$$[k_e] = \begin{bmatrix} k & -k \\ -k & k \end{bmatrix} \tag{47}$$

where it is defined as the element stiffness matrix in the element or local coordinate system. $\{u\}$ is the column matrix (vector) of nodal displacements and $\{f\}$ is the column matrix (vector) of element nodal forces.

Equation 45 shows that the element stiffness matrix for the linear spring element is a 2x2 matrix, which corresponds to the fact that only two degrees of freedom are exhibited by the element and that they are not independent (the

body is continuous and elastic).

The matrix is symmetrical as a consequence of the symmetry in the forces and singular, thus not invertible because the problem definition lacks any boundary conditions making it incomplete.

The individual element stiffness matrices (described earlier) are summed into an overall stiffness matrix K which covers the entire geometry. So given

$$F = K.U \tag{48}$$

it can then be stated that

$$\rightarrow U = K^{-1}F \tag{49}$$

Where U is the vector of displacements over all vertices in the mesh, K is the overall stiffness matrix which is non-singular and invertible and F is the vector of applied forces to the mesh representing the object.

Above summary of mathematical steps used in FEM

- Using properties of Hilbert spaces convert the problem into a vector problem
- In order for the problem to be posed as an inner product a weak formulation must be created
- Discretize the domain
- Choose basis functions that do not overlap elements
- Convert the inner product into a set of linear equations and solve to get the solution

FEM approximation issues

As with any mathematical model of a real-world there are bound to be inherent flaws and FEM is also susceptible to this:

- Modelling errors - When arriving at a mathematical model of a real problem, some assumptions must be made. These assumptions may not always exactly reflect the true behaviour of the problem it is trying to model.
- Numerical errors - These are general small rounding errors and truncations, but can become significant over the course of the analysis if incorrect practices are undertaken.
- Discretisation errors - The physical model which is modelled will have an infinite number of degrees of freedom (dof), but the very nature of the simplified mathematical model means that FEM analysis of the problem will have a finite number of dof. This issue becomes less pronounced with increasing numbers of elements, but there will always be an inherent limitation.

Anisotropic materials

Unlike isotropic materials like glass and metals which have identical values of a property in all directions, anisotropic material's properties change with direction along the object.

In the case of a general, linearly elastic, anisotropic material, using tensor notation the constitutive equation is given by [19]:

$$\epsilon_{ij} = S_{ijkl}\sigma_{kl} \tag{50}$$

where ϵ_{ij} represents the second-rank strain tensor, σ_{kl} is the second-rank stress tensor and S_{ijkl} is the fourth-rank compliance matrix.

Given a fourth-rank elasticity tensor C_{ijkl} where:

$$C_{ijkl} = S_{ijkl}^{-1} \tag{51}$$

gives:

$$\sigma_{ij} = C_{ijkl}\epsilon_{kl} \tag{52}$$

For general 3D anisotropic bodies, i, j, k and l range from 1 to 3 [19]. After accounting for symmetry, there are 21 independent material constants needed to describe full anisotropy.

Hyperelasticity

A hyperelastic material is one that is described using a strain-energy density function. This is unlike a linearly elastic material which would generally be described using two material constants such as Young's Modulus and Poisson ratio. All hyperelastic materials possess an elastic potential function. The hyperelastic strain-energy density function is used to derive a non-linear constitutive model. There are a number of proposed models such as Neo-Hookean, Ogden and Mooney-Rivlin (MR). The MR constitutive equation for rubber is:

$$W = C_1 (I_1 - 3) + C_2 (I_2 - 3) \tag{53}$$

where material-dependent constants C_1 and C_2 must be determined through tests on an actual material. C_1 by uniaxial tension or compression tests and C_2 by performing a biaxial test such as inflation of a circular membrane. I_1 and I_2 represent the first and second deviatoric strain invariants written in terms of the principal stretch ratios λ_1, λ_2 and λ_3.

The strain-energy function for an MR material can therefore be stated as

$$W = C_1 (I_1 - 3) + C_2 (I_2 - 3) = C_1 [(I_1 - 3) + \alpha (I_2 - 3)] \quad (54)$$

where $\alpha = C_2/C_1$. The strain invariants are expressed as

$$I_1 = \lambda_1^2 + \lambda_2^2 + \lambda_3^2 \quad (55)$$

$$I_2 = \lambda_1^2\lambda_2^2 + \lambda_2^2\lambda_3^2 + \lambda_3^2\lambda_1^2 \quad (56)$$

with the assumption of incompressibility it can then be stated that

$$\lambda_1\lambda_2\lambda_3 = 1 \quad (57)$$

Hydrostatic Fluid Elements - Volume Calculation

The information contained in this section is an adaptation of the volume calculation description within the Abaqus Theory Manual [108]. The purpose of this section is to provide a basic explanation on how the internal volume of the skull was calculated and modelled. For a more in depth and detailed explanation of HFE please consult the Abaqus theory manual [108] and other relevant FEM literature.

Figure 115: An example of a tetrahedral F3D4 element, the integration point for which is located at the centre.

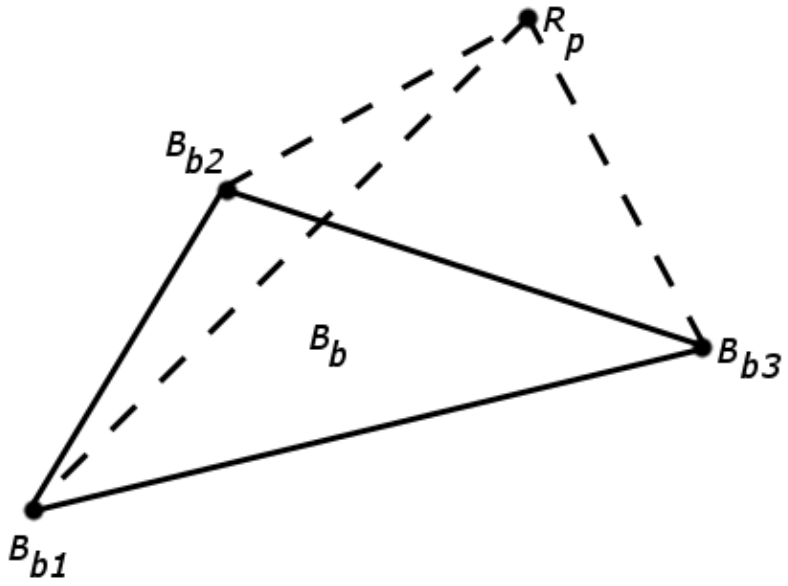

F3D4 is a fluid element representation of the equivalent general purpose tetrahedral C3D4 element which has 1 integration point (see Figure 115 for a visual representation). In the context of this section the element will be defined by four sections; The cavity reference node, R_p, the solid element base representing a part of the enclosed volume space, B_b with the individual points that make up the base B_{bn}. The calculated boundaries of the element, B_v, and the volume as denoted by V^e.

Any of the base plate coordinates can be found by:

$$x = \sum_i N^i (g, h)\, x^i \tag{58}$$

where N^i denotes the interpolation functions of B_b when expressed in terms of parametric coordinates g and h. x^i are the nodal coordinates. As shown, the

summation extends over all nodes of B_b. In the case of F3D4 $i = 4$ and therefore Eq. 58 can be rewritten as

$$x = \sum_{i=1}^{4} N^i (g, h) x^i \tag{59}$$

For three-dimensional elements the Jacobian matrix on the surface is calculated as

$$\frac{\partial x}{\partial g} = \sum_{i=1}^{4} \frac{\partial N^i}{\partial g} x^i \tag{60}$$

and

$$\frac{\partial x}{\partial h} = \sum_{i=1}^{4} \frac{\partial N^i}{\partial h} x^i \tag{61}$$

an inward facing normal to the element face, n, multiplied by an infinitesimal area , dA, of the same element face can be defined as

$$\mathbf{n} dA = \left(\frac{\partial x}{\partial g} \times \frac{\partial x}{\partial h} \right) dg dh \tag{62}$$

given $\mathbf{n}dA$, the infintesimal volume dV associated with dA can be described as

$$dV = \frac{1}{3} (R_P - x) \cdot \mathbf{n} dA \tag{63}$$

where R_P is the position of R_p.

For a triangular representation of B_b, providing the relative position of $\overline{x} =$

$x - R_P$, V^e can be obtained with the following integral;

$$V^e = \int_{-1}^{+1} \int_{-1}^{+1} -\frac{1}{3}\overline{x} \cdot \mathbf{n} dA \tag{64}$$

The element volume variations can be obtained by:

$$\delta V^e = \int_{-1}^{+1} \int_{-1}^{+1} -\frac{1}{3}\left[\delta\overline{x} \cdot \left(\frac{\partial x}{\partial g} \times \frac{\partial x}{\partial h}\right) + \overline{x} \cdot \left(\frac{\partial \delta\overline{x}}{\partial g} \times \frac{\partial \overline{x}}{\partial h} + \frac{\partial \overline{x}}{\partial g} \times \frac{\partial \delta\overline{x}}{\partial h}\right)\right] dgdh \tag{65}$$

therefore, the resulting expression is

$$\delta V_b^e = \int_{-1}^{+1} \int_{-1}^{+1} -\delta\overline{x} \cdot \left(\frac{\partial \overline{x}}{\partial g} \times \frac{\partial \overline{x}}{\partial h}\right) dgdh \tag{66}$$

References

[1] Nan G OConnel and Elizabeth Munter. Intrauterine pressure catheter placement. Medscape, 2015.

[2] Family Education. What happens during the first stage of labor. familyeducation.com. http://pregnancy.familyeducation.com/signs-and-stages-of-labor/slideshow/66291.html?page=1.

[3] Gale Encyclopedia of Medicine. Caesarean section. http://medical-dictionary.thefreedictionary.com/cesarean+section, 2008.

[4] D. L. S. Eustace. James young simpson: the controversy surrounding the presentation of his air tractor (1848-1849). *Journal of the Royal Society of Medicine*, 86:660–663, November 1993.

[5] Science Museum London. Malmström's obstetrical vacuum extractor, gothenburg, sweden, 1979.

[6] Clinical Innovations. Kiwi - complete vacuum delivery system.

[7] ESP Educational and Scientific Products Ltd. ESP ZKK-240K fetal head model. http://esp-models.co.uk/.

[8] AUSTOS. Surgical instruments and endoscopes. austos.com.

[9] *International Maternal and Child Healthcare Textbook.* Maternal and Childhealth Advocacy International MCAI, June 2015.

[10] Sam Thomas. Newborn skin findings. quizlet.com. /121938681/newborn-skin-findings-flash-cards/.

[11] Guido Currarino. Neonatal subperiosteal cephalohematoma crossing a synostosed sagittal suture. *Pediatric Radiology*, 37(12):1283–1285, September 2007.

[12] Sydney Pelvic Floor Health. Obstetric anal sphincter injury (oasi): Third or fourth degree perineal tear. http://sydney.edu.au/.

[13] Lennox Hoyte, Margot S. Damaser, Simon K. Warfield, Giridhar Chukkapalli, Amitava Majumdar, Dong Ju Choi, Abhishek Trivedi, and Petr Krysl. Quantity and distribution of levator ani strectch during simulated vaginal childbirth. *American Journal of Obstetrics and Gynecology*, 199:198.e1–5, 2008.

[14] M. Scudder and Y. Liu. CAD modeling of the birth process. In *Proceedings of Medicine Meets Virtual Reality IV Conference*, 1996.

[15] Melchert F, Forster C, and Bechtold I. Clinical use of the birth simulation program "anapelvis 2.0" for prediction of feto-maternal disproportion. *Zentralbl Gynakol*, 123(8):465–468, 2001.

[16] Ning Zhang, Bernard Gonik, and Michele J. Grimm. Defining forces that are associated with shoulder dystocia: The use of a mathematic dynamic computer model. *American Journal of Obstetrics and Gynecology*, 188(4):1068–1072, April 2003.

[17] M. Brunnel, A. Kheddar, C. Devine, and O. Sibony. Interactive childbirth simulator with haptic feedback: Preliminary design. In *Proceedings of EuroHaptics*, 2004.

[18] Buttin R, Zara F, Shariat B, Redarce T, and Grangé G. Biomechanical simulation of the fetal descent without imposed theoretical trajectory. *Computer methods and programs in biomedicine*, 111(2):389–401, 2013.

[19] Rudy Jacques Augusta Lapeer. *A biomechanical model of foetal head moulding*. PhD thesis, Queens' College Cambridge and Department of Engineering, University of Cambridge, August 1999.

[20] John o. l. Delancey, James A. Ashton-Miller, Kuo-Cheng Lien, and Daniel M. Morgan. Pudendal nerve stretch during vaginal birth: A 3d computer simulation. *American Journal of Obstetrics and Gynecology*, 192:1669–1676, 2005.

[21] T. Mascarenhas, A. A. Fernandes-J., A. C. Martins, M. P. L. Parente, and R. M. Natal Jorge. Deformation of the pelvic floor muscles during a vaginal delivery. *International Urogynecology Journal*, 19:65–71, 2008.

[22] T. Mascarenhas, A. A. Fernandes-J., A. C. Martins, M. P. L. Parente, and R. M. Natal Jorge. The influence of an occipito-posterior malposition on the biomechanical behaviour of the pelvic floor. *European Journal of Obstetrics, Gynecology, and Reproductive Biology*, 144:166–169, 2009.

[23] Bernard Gonik, Robert Allen, and Jagadish Sorab. Objective evaluation of the shoulder dystocia phenomenon: Effect of maternal pelvic orientation on force reduction. *Obstetrics & Gynecology*, 74(1):44–48, 1989.

[24] B. R. Bankoski, R. H. Allen, and D. A. Nagey. Simulating birth to investigate clinician-applied loads to newborns. *Medical Engineering and Physics*, 17(5):380–384, 1995.

[25] Mary K. McDonald, Edith D. Gurewitsch, Esther J. Kim, Parnduangjai Theprungsirikul, and Robert H. Allen. A biofidelic birthing simulator. *IEEE Engineering in Medicine and Biology Magazine*, pages 34–39, November/December 2005.

[26] R. C. Silveira. *Modelisation et conception d'un nuoveou simulateur d'accouchement (BIRTHSIM) pour l'entrainement et l'enseignement des jeunes obstetriciens et des sages-femmes.* PhD thesis, INSA de Lyon, 2004.

[27] Dupuis O, Moreau R, Silveira R, Pham MT, Zentner A, Cucherat M, Rudigoz RC, and Redarce T. A new obstetric forceps for the training of junior doctors: A comparison of the spatial dispersion of forceps blade trajectories between junior and senior obstetricians. *American Journal of Obstetrics and Gynecology*, 194:1524–31, 2006.

[28] Lapeer R.J., Rowland R.S, and Chen M-S. Pc-based volume rendering for medical visualisation and augmented reality based surgical navigation. In *MediViz/IV04 Conference Proceedings*, pages 67–72. IEEE Computer Society, IEEE Computer Society, 2004.

[29] Vincenzo Loia, Stefano Ricciardi, Andrea F. Abate, Giovanni Acampora, and Athanasios V. Vasilakos. A pervasive visual-haptic framework for virtual delivery training. *IEEE Transactions on Information Technology in Biomedicine*, 14(2):326–334, March 2010.

[30] U.S. National Library of Medicine. The visible human project.

[31] William E. Lorensen and Harvey E. Cline. Marching cubes: A high resolution 3d surface construction algorithm. In *SIGGRAPH '87 Proceedings of the 14th annual conference on Computer graphics and interactive techniques*, volume 21, pages 163–169. ACM, 1987.

[32] F. Bell. *Biomechanics of human parturition: A fundamental approach to the mechanics of the first stage of labour.* PhD thesis, University of Strathclyde - Glasgow, March 1972.

[33] *COMSOL Multiphysics.* www.comsol.com/multiphysics/finite-element-method.

[34] Armando Tura and Zuomin Dong. *Lecture in Introduction to Finite Element Analysis (FEA) or Finite Element Method (FEM).* University of Victoria - Department of Engineering, 2014.

[35] Thomas McCracken. *New Atlas of Human Anatomy.* Metro Books, 1999.

[36] Blasiak T, Czubak W, Ignaciak A, and Lewandowski MH. A new approach to detection of the bregma point on the rat skull. *Journal of Neuroscience Methods*, 185(2):199–203, January 2010.

[37] Bofill JA, Rust OA, Devidas M, Roberts WE, Morrison JC, and Martin JN Jr. Neonatal cephalohematoma from vacuum extraction. *The Journal of Reproductive Medicine*, 42(9):565–569, 1997.

[38] Hubert B. Liselele, Michel Boulvain, Kalala C. Tshibangu, and Sylvain Meuris. Maternal height and external pelvimetry to predict cephalopelvic disproportion in nulliparous african women: a cohort study. *BJOG: An International Journal of Obstetrics and Gynaecology*, 107(8):947–952, August 2000.

[39] Arthur C Guyton and John Edward Hall. *Textbook of medical physiology.* W.B. Saunders, 11th edition, 2005.

[40] NHS. CT scan. Website, July 2015.

[41] Katherine L. Williams and Joseph G. Pastorek II. Postpartum endomyometritis. *Infectious Diseases in Obstetrics and Gynecology*, 3(5):210–216, 1995.

[42] F H Netter. *The Ciba Collection of Medical Illustrations: Part I: Anatomy, Physiology and Metabolic Disorders: The Musculoskeletal System Vol 8*, volume 8. Novartis Medical Education Program, 1987.

[43] Peleg D, Hasnin J, and Shalev E. Fractured clavicle and erb's palsy unrelated to birth trauma. *American Journal of Obstetrics and Gynecology*, 177(5):1038–1040, 1997.

[44] J.N Reddy. *An Introduction to the Finite Element Method*. McGraw-Hill, third edition, 2006.

[45] Dalley K, Moore A, and Agur F. *Clinically oriented anatomy*. Lippincott Williams & Wilkins, 6th edition edition, 2010.

[46] Grigorescu BA, Lazarou G, Olson TR, Downie SA, Powers K, Greston WM, and Mikail MS. Innervation of the levator ani muscles: description of the nerve branches to the pubococcygeus, iliococcygeus, and puborectalis muscles. *International Urogynecology Journal and Pelvic Floor Dysfunction*, 19(1):107–116, 2008.

[47] P. J. Kearns. The lower uterine segment: Anatomical changes during pregnancy and labour. *Canadian Medical Association Journal*, 46(1):19–22, 1942.

[48] NHS. MRI scan. Website, October 2015.

[49] M. Gardberg and M. Tuppurainen. Persistent occiput posterior presentation - a clinical problem. *Acta Obstetricia et Gynecologica Scandinavica*, 198(4):117–119, 1994.

[50] Longo D, Fauci A, Kasper D, Hauser S, Jameson J, and Loscalzo J. *Harrison's Principles of Internal Medicine*. McGraw-Hill, 18th edition edition, 2012.

[51] P Tank. *Grant's Dissector*. Lippincott Williams and Wilkins, 15th edition edition, 2012.

[52] Rie Usui, Shigeki Matsubara, Akihide Ohkuchi, Tomoyuki Kuwata, Takashi Watanabe, Akio Izumi, and Mitsuaki Suzuki. Fetal heart rate pattern reflecting the severity of placental abruption. *Archives of Gynecology and Obstetrics*, 277(3):249–253, 2007.

[53] Royal College of Obstetricians and Gynaecologists. Placenta praevia, placenta praevia accreta and vasa praevia: diagnosis and management. Pdf, January 2011.

[54] Medscape. Rectus sheath hematoma. Website, November 2014.

[55] Royal College of Obstetricians and Gynaecologists. Shoulder dystocia. Pdf, March 2013.

[56] Ronald S Gibbs, David N. Danforth, Beth Y Karlan, and Arthur F Haney. *Danforth's obstetrics and gynecology*. Lippincott Williams and Wilkins, 2008.

[57] Hiralal Konar. *D C Dutta's Textbook of Obstetrics*. Jaypee Brothers Medical Publishers, 7th edition edition, 2014.

[58] Courtney Crawford and Robert Mazzoli. Subperiosteal hematoma in multiple settings. *Digital Journal of Opthamology*, 19(1):1–10, 2013.

[59] NHS. Craniosynostosis - symptoms. Website, November 2014.

[60] Royal College of Obstetricians and Gynaecologists. Umbilical cord prolapse. Pdf, November 2014.

[61] Rudy Lapeer, Vilius Audinis, Zelimkhan Gerikhanov, and Olivier Dupuis. A computer-based simulation of obstetric forceps placement. *Lecture Notes in Computer Science*, 8674:57–64, 2014.

[62] Rudy Lapeer, Vilius Audinis, Zelimkhan Gerikhanov, and Olivier Dupuis. A computer-based simulation of obstetric forceps placement. In *MICCAI*, 2014.

[63] Rudy J. Lapeer, Zelimkhan Gerikhanov, and Vilius Audinis. Simulation of vacuum extraction during childbirth using finite element analysis. In *SIMULIA UK Regional User Meeting*, 2014.

[64] Z. Gerikhanov, V. Audinis, and R. Lapeer. Towards a forward engineered simulation of the cardinal movements of human childbirth. In *E-Health and Bioengineering Conference (EHB), 2013*, pages 1–4, November 2013.

[65] Leah L. Albers, Melissa Schiff, and Julie G. Gorwoda. The length of active labor in normal pregnancies. *Obstetrics & Gynecology*, 87(3):355–359, 1996.

[66] AC Allman, ES Genevier, MR Johnson, and PJ Steer. Head-to-cervix force: an important physiological variable in labour. 2. peak active force, peak active pressure and mode of delivery. *British Jounal of Obstetrics and Gynaecology*, 103(8):769–775, 1996.

[67] O. Dupuis, R Silveira, A Zentner, A Dittmar, P Gaucherand, M Cucherat, T Redarce, and RC Rudigoz. Birth simulator: reliability of transvaginal assessment of fetal head station as defined by the american college of obstetricians and gynecologists classification. *Americal Journal of Obstetrics and Gynecology*, 192(3):868–874, March 2005.

[68] Royal College of Obstetricians and Gynaecologists. Overative vaginal delivery, January 2011.

[69] https://www.rcog.org.uk/en/news/rcog-statement-on-emergency-caesarean-section-rates/.

[70] Carolyn Gardella, Melanie Taylor, Thomas Benedetti, Jane Hitti, and Cathy Critchlow. The effect of sequential use of vacuum and forceps for assisted vaginal delivery on neonatal and maternal outcomes. *American Journal of Obstetrics and Gynecology*, 185:896–902, 2001.

[71] C.C.T. Chan and G.S.H. Yeo. Is the vacuum extractor really the instrument of first choice? *ANZJOG*, 39(3):305–309, August 1999.

[72] J. A. Chalmers and I. Chalmers. The obstetric vacuum extractor is the instrument of first choice for operative vaginal delivery. *BJOG*, 96(5):505–506, May 1989.

[73] Unzila A Ali and Errol R Norwitz. Vacuum-assisted vaginal delivery. *Review in Obstetrics and Gynecology*, 2(1):5–17, 2009.

[74] Jane Eliot Sewell. Caeserean section – a brief history. National Library of Medicine Booklet, April 1993.

[75] Royal College of Obstetricians and Gynaecologists. Royal college of obstetricians and gynaecologists q&a article. *The Obstetrician and Gynaecologist*, 8:129–134, 2006.

[76] https://stratog.rcog.org.uk/tutorial/obstetrics/instrumental-delivery-5810.

[77] Roshni R Patel and Deirdre J Murphy. Forceps delivery in modern obstetric practice. *The BMJ*, 328(7451):1302–1305, May 2004.

[78] Aliya Islam, Ambreen Ehsan, Saadia Arif, Javeria Murtaza, and Ayesha Hanif. Evaluating trial of scar in patients with a history of caesarean section. *North Americal Journal of Medical Sciences*, 3(4):201–205, 2011.

[79] E. N. Gofton, V. Capewell, R. Natale, and R. J. Gratton. Obstetrical intervention rates and maternal and neonatal outcomes of women with gestational hypertension. *American Journal of Obstetrics and Gynecology*, 185:798–803, 2001.

[80] Sally K. Tracy, Elizabeth Sullivan, Yueping Alex Wang, Deborah Black, and Mark Tracy. Birth outcomes associated with interventions in labour amongst low risk women: A population-based study. *Women and Birth*, 20:41–48, 2007.

[81] Deborah J. Davis. Neonatal subgaleal hemorrhage: diagnosis and management. *CMAJ*, 164(10):1452–1453, May 2001.

[82] Tia P. Andrighetti, Joyce M. Knestrick, Amy Marowitz, Cheryl Martin, and Janet L. Engstrom. Shoulder dystocia and postpartum hemorrhage simulations: Student confidence in managing these complications. *Journal of Midwifery and Women's Health*, 57(1):55–60, 2012.

[83] Ylenia Fonti, Rosalba Giordano, Alessandra Cacciatore, Mattea Romano, and Beatrice La Rosa. Post partum pelvic floor changes. *Journal of Parental Medicine*, 3(4):57–59, 2009.

[84] SA Baydock, C Flood, JA Schulz, D MacDonald, D Esau, S Jones, and CB Hiltz. Prevalence and risk factors for urinary and fecal incontinence four months after vaginal delivery. *Journal of Obstetrics and Gynaecology Canada*, 31(1):36–41, 2009.

[85] Mary Lindemann. *Medicine and Society in Early Modern Europe*. Cambridge University Press, 2010.

[86] Jonathon Hodor, Andrew J. Satin, Shad Deering, and Jill Brown. Simulation training and resident performance of singleton vaginal breech delivery. *Obstetrics and Gynecology*, 107(1):86–89, January 2006.

[87] Emil R. Petrusa, William C. McGaghie, S. Barry Issenberg, and Ross J. Scalese. A critical review of simulation-based medical education research: 2003-2009. *Medical Education*, 44:50–63, 2010.

[88] Jo Porter, Fiona Bogossian, Lisa McKenna, Susannah Brady, Stephanie Fox-Young, Simon Cooper, and Robyn Cant. Simulation based learning in midwifery education: A systematic review. *Women and Birth*, 25:64–78, 2012.

[89] B. Geiger. *Construction et utilisation des modeles d'organes en vue de l'assistance au diagnostic et aux interventions chirurgicales*. Phd thesis, Travaux Universitaires, 1993.

[90] B. Geiger and J. D. Boissonnat. 3d simulation of delivery. In *Proceedings in IEEE Conference on Visualization*, 1993.

[91] K. Lehmann, K. Wentz, M. Georgi, F. Melchert, A. Wischnik, and E. Nalep. Zur prävention des menschlichen geburtstraumas i. mitteilung: Die computergestützte simulation des geburtsvorganges mit hilfe der kernspintomographie und der finiten-element-analys. *Geburtshilfe und Frauenheilkunde*, 53(1):35 – 41, 1993.

[92] Bernard Gonik, Ning Zhang, and Michele J. Grimm. Development of a madymo model to investigate fetal branchial plexus injury during compli-

cated vaginal delivery. In *Summer Bioengineering Conference*, June 25-29 2003.

[93] M. Brunel, C. Duriez, A. Kheddar, and C. Devine. Preliminary design of a childbirth simulator with haptic feedback. In *IEEE/RSJ International Conference on Intelligent Robots and Systems*, 2004.

[94] Y. C. Fung. *Biomechanics: Mechanical Properties of Living Tissues*. Springer, 1993.

[95] Matthew D. Barber. Contemporary views on female pelvic anatomy. *Cleveland Clinic Journal of Medicine*, 72(Supplement 4):S3–11, December 2005.

[96] Rudy J. Lapeer and R. W. Prager. Fetal head moulding: finite element analysis of a fetal skull subjected to uterine pressures during the first stage of labour. *Journal of Biomechanics*, 34:1125–1133, 2001.

[97] K-M Su, M-H Yu, H-Y Su, Y-C Wang, and K-C Su. Investigating biomechanics of different matemater and angles of blade of forceps for operative delivery by finite element analysis. *Journal of Mechanics in Biology and Medicine*, 16(4):1–12, 2016.

[98] Vilius Audinis. Simulating shoulder dystocia. Master's thesis, University of East Anglia, Department of Computing Sciences, 2008.

[99] Autodesk. 3D studio max.

[100] Tomas Akenine-Möller. Fast 3d triangle-box overlap testing. In *ACM SIGGRAPH 2005 Courses*, SIGGRAPH '05, New York, NY, USA, 2005. ACM.

[101] Olivier Devillers and Philippe Guigue. Faster triangle-triangle intersection tests. Technical Report RR-4488, INRIA, 2002.

[102] O. Tropp, Ayellet Tal, and I. Shimshoni. A fast triangle to triangle intersection test for collision detection. *Computer Animation and Virtual Worlds*, 17:527–535, 2006.

[103] L. Lindgren. The causes of foetal head moulding in labour. *Acta Obstet. Gynecol. Scand.*, 39:46–62, 1960.

[104] L. Lindgren. The influence of pressure upon the fetal head during labour. *Acta Obstet. Gynecol. Scand.*, 56(4):303–309, 1977.

[105] Blender Online Community. *Blender - a 3D modelling and rendering package*. Blender Foundation.

[106] Carole Kenner. *Comprehensive Neonatal Nursing Care*. Springer Publishing Company, 2014.

[107] Christine A. Gleason and Sandra E Juul. *Avery's Diseases of the Newborn*. Elsevier Health Sciences, 2011.

[108] Simulia. *Abaqus Theory Guide (6.14)*. Simulia, 2015.

[109] Donita I. Bylski, Timothy J Kriewall, Nuri Akkas, and John W. Melvin. Mechanical behavior of fetal dura mater under large deformation biaxial tension. *Journal of Biomechanics*, 19(1):19–26, 1986.

[110] B Sorbe and S Dahlgren. Some important factors in the molding of the fetal head during vaginal delivery - a photographic study. *International Journal of Gynaecology and Obstetrics*, 21(3):205–212, June 1983.

[111] Susan Tucker Blackburn. *Maternal, Fetal, & Neonatal Physiology: A Clinical Perspective*. Elsevier Health Sciences, 2007.

[112] Sinha P. and Langford K. Forceps delivery in 21st century obstetrics. *The Internet Journal of Gynecology and Obstetrics*, 11(2), 2008.

[113] F. Pu, L. Xu, D. Li, S. Li, L. Sun, L. Wang, and Y. Fan. Effect of different labor forces on fetal skull molding. *Medical Engineering Physics*, 33:620–625, 2011.

[114] Tierney Kinnison, Neil David Forrest, Stephen Philip Frean, and Sarah Baillie. Teaching bovine abdominal anatomy: Use of a haptic simulator. *Anatomical Sciences Education*, 2(6):280–285, 2009.

[115] O.C. Zienkiewicz, R.J. Taylor, and J.Z. Zhu. *The Finite Element Method: Its Basis & Fundamentals*. Elsevier, 2005.

[116] Klaus-Jürgen Bathe. *Finite Element Procedures*. Prentice-Hall, 1996.

[117] The National Health Service Litigation Authority. NHS litigation authority report and accounts 2013-2014, July 2014.

[118] The National Health Service Litigation Authority. NHS litigation authority report and accounts 2012-2013, July 2013.

[119] The National Health Service Litigation Authority. NHS litigation authority report and accounts 2011-2012, June 2012.

[120] The National Health Service Litigation Authority. NHS litigation authority report and accounts 2010-2011, July 2011.

[121] Sabrina Badir, Edoardo Mazza, Roland Zimmermann, and Michael Bajka. Cervical softening occurs early in pregnancy: characterization of cervical stiffness in 100 healthy women using the aspiration technique. *Prenatal Diagnosis*, 33:737–741, 2013.

[122] K. Baeck, J. Goffin, and J. Vander Sloten. The use of different csf representations in a numerical head model and their effect on the results of fe

head impact analyses. In *8th European LS-DYNA Users Conference*, May 2011.

[123] Christian Bamberg, Jan Deprest, Nikhil Sindhwani, Ulf Teichgraberg, Felix Güttler, Joachim W. Dudenhausen, Karim D. Kalache, and Wolfgang Henrich. Evaluating fetal head dimension changes during labor using open magnetic resonance imaging. *Journal of Perinatal Medicine*, 2016.

[124] Katherine Butler, Meenakshi Ramphul, Clare Dunney, Maria Farren, Aoife McSweeney, Karen McNamara, and Deirdre J Murphy. A prospective cohort study of the morbidity associated with operative vaginal deliveries performed by day and at night. *BMJ Open*, 4, 2014.

[125] Brittany Coats and Susan S. Margulies. Parametric study of head impact in the infant. *Stapp Car Crash Journal*, 51:1–15, October 2007.

[126] Cecilia Ekéus, Ulf Högberg, and Mikael Norman. Vacuum assisted birth and risk for cerebral complications in term newborn infants: a population-based cohort study. *BMC Pregnancy and Childbirth*, 14(36), 2014.

[127] Nayra Grau, Joseph L. Daw, Rupal Patel, Carla Evans, Naama Lewis, and Jeremy J. Mao. Nanostructural and nanomechanical properties of synostosed postnatal human cranial sutures. *The Journal of Craniofacial Surgery*, 17(1):91–99, January 2006.

[128] Maria C. Jimenez Hamann, Michael S. Sacks, and Theodore I. Malinin. Quantification of the collagen fibre architecture of human cranial dura mater. *Journal of Anatomy*, 192:99–106, 1998.

[129] S. C. Jasinoski, B. D. Reddy, K. K. Louw, and A.Chinsamy. Mechanics of cranial sutures using the finite element method. *Journal of Biomechanics*, 43:3104–3111, 2010.

[130] R. B. Johanson, E. Heycock, J. Carter, A. H. Sultan, K. Walklate, and P. W. Jones. Maternal and child health after assisted vaginal delivery: five-year follow up of a randomised controlled study comparing forceps and ventouse. *British Journal of Obstetrics and Gynaecology*, 106:544–549, 1999.

[131] J. A. Z. Loudon, K. M. Groom, L. Hinkson, D. Harrington, and S. Paterson-Brown. Changing trends in operative delivery performed at full dilatation over a 10-year period. *Journal of Obstetrics and Gynaecology*, 30(4):370–375, May 2010.

[132] Susan S. Margulies and Kirk L. Thibault. Infant skull and suture properties: Measurements and implications for mechanisms of pediatric brain injury. *Transactions of the ASME*, 122:364–371, August 2000.

[133] Kristin M. Myers, Helen Feltovich, Edoardo Mazza, Joy Vink, Michael Bajka, Ronald J. Wapner, Timothy J. Hall, and Michael House. The mechanical role of the cervix in pregnancy. *Journal of Biomechanics*, 48(9):1511–1523, June 2015.

[134] J. M. Nursherida, B. B. Sahari, A. A. Nuraini, and A. Manohar. Finite element modelling of 1 year-old pediatric head with fontanel impact: Validation against experimental data. *Australian Journal of Basic and Applied Sciences*, 9(8):53–61, 2015.

[135] Arna Oskarsdottir. Finite element analysis of infant skull trauma using ct images. Master's thesis, Royal Institute of Technology, Stockholm, Sweden, 2012.

[136] Joong Shin Park, Julian N. Robinson, and Errol R. Norwitz. Rotational forceps: Should these procedures be abandoned? *Seminars in Perinatology*, 27(1):112–120, February 2003.

[137] Aalap Patel and Tarun Goswami. *Comparison of Intracranial Pressure by Lateral and Frontal Impacts - Validation of Computational Model*, chapter 6, pages 95–115. InTech, July 2012.

[138] Nicola Perone. Clinician to clinician: Bringing operative vaginal delivery into the 21st century. *Contemporary OB/GYN*, January 2014.

[139] James A. Thorp, Philip G. Jones, Reese H. Clark, Eric Knox, and Joyce L. Peabody. Perinatal factors associated with severe intracranial hemorrhage. *American Journal of Obstetrics and Gynecology*, 185:859–862, 2001.

[140] Erika F. Werner, Teresa M. Janevic, Jessica Illuzzi, Edmund F. Funai, David A. Savitz, and Heather S. Lipkind. Mode of delivery in nulliparous women and neonatal intracranial injury. *Obstetrics and Gynecology*, 118(6):1239–1246, December 2011.

[141] E. H. Whitby, P. D. Griffiths, S. Rutter, M. F. Smith, A. Sprigg, P. Ohadike, N. P. Davies, A. S. Rigby, and M. N. Paley. Frequency and natural history of subdural haemorrhages in babies and relation to obstetric factors. *The Lancet*, 363:846–851, 2004.

[142] S. Christine Zahniser, Juliette S. Kendrick, Adele L. Franks, and Audrey F. Saftlas. Trends in obstetric operative procedures, 1980 to 1987. *American Journal of Public Health*, 82(10):1340–1344, October 1992.

[143] Stephen Joseph Ball. *Novel robotic mechanisms for upper-limb rehabilitation and assesment.* PhD thesis, Queen's University, Kingston, Ontario, Canada, August 2008.

[144] Elizabeth G. Baxley and Robert W. Gobbo. Shoulder dystocia. *American Family Physician*, 69(7):1707–1714, 2004.

[145] Alberta Walker, Bernard Gonik, and Michele Grimm. Mathematical modeling of forces associated with shoulder dystocia a comparison of endogenous and exogenous sources. *American Journal of Obstetrics and Gynecology*, 182(3):698–691, March 2000.

[146] Lisa Brousard. Simulation-based learning how simulators help nurses improve clinical skills and preserve patient safety. *Nursing for Women's Health*, 12(2):521–524, 2008.

[147] P. Youngblood and C. M. Pugh. Development and validation of assessment measures for a newly developed physical examination simulator. *Journal of the American Medical Informatics Association*, 9(5), Sept/Oct 2002.

[148] Andrew J. Satin and Christopher S. Ennen. Training and assesment in obstetrics: the role of simulation. *Best Practice and Research Clinical Obstetrics and Gynaecology*, 24:747–758, 2010.

[149] Ambarish Goswami, Deepak Tolani, and Norman I. Badler. Real-time inverse kinematics techniques for antromorphic limbs. *Graphical Models*, 62:353–388, 2000.

[150] Scott L. Delp and J. Peter Loan. A graphics-based software system tobjective develop and analyze models of musculoskeletal structures. *Computers in Biology and Medicine*, 25:21–34, 1995.

[151] Erik J. Dijkstra. Upper limb project. Master's thesis, Department of Engineering Technology, University of Twente, October-December 2010.

[152] Nathalie Doriot and Laurence Cheze. A three-dimensional kinematic and dynamic study of the lower limb during the stance phase of gait using an homogeneous matrix approach. *IEEE Transactions on Biomedical Engineering*, 51:21–27, 2004.

[153] P. P. Valentini, L. Vita, E. Pennestri, and R. Stefanelli. Virtual musculoskeletal model for the biomechanical analysis of the upper limb. *Journal of Biomechanics*, 40:1350–1361, 2007.

[154] Robert H. Allen, Edith D. Gurewitsch, and Tara L. Johnson. After shoulder dystocia: Managing the subsequent pregnancy and delivery. *Seminars in Pernatology*, 31:185–195, 2007.

[155] Robert Hanscom. Medical simulation from an insurer's perspective. *Academic Emergency Medicine*, 15:984–987, 2008.

[156] Neville Hogan. The mechanics of multi-joint posture and movement control. *Biological Cybernetics*, 52:315–331, 1985.

[157] Daniel M. Corcos, James S. Thomas, and Ziaul Hasan. Kinematic and kinetic constraints on arm, trunk, and leg segments in target-reaching movements. *Journal of Neurophysiology*, 93:352–364, 2004.

[158] Blok SB, Janda S, and Van der Helm FCT. Measuring morphological parameters of the pelvic floor for finite elements modelling purposes. *Journal of Biomechanics*, 36:749–757, 2003.

[159] Benjamin J. Fregly, Byung Il Koh, Raphael T. Hafka, Alan D. George, Kim H. Mitchell, Jeffery A. Reinbolt, and Jaco F. Schutte. Determination of patient-specific multi-joint kinematic models through two-level optimization. *Journal of Biomechanics*, 38:621–626, 2005.

[160] Nicole Malfait, Jeremy Wong, Elizabeth T. Wilson, and Paul L. Gribble. Limb stiffness is modulated with spacial accuracy requirements during movement in the absence of destabilizing forces. *Journal of Neurophysiology*, 101:1542–1549, 2009.

[161] J F Crofts, C Bartlett, D Ellis, L P Hunt, R Fox, and T J Draycott. Training for shoulder dystocia: a trial of simulation using low-fidelity and high-fidelity mannequins. *Obstetrics and Gynecology*, 108(6):1477–1485, December 2006.

[162] Mike Read, Thabani Sibanda, Timothy J. Draycott, Joanna F. Crofts, and Georgios Attilakos. Shoulder dystocia training using a new birth training mannequin. *BJOG: an International Journal of Obstetrics and Gynaecology*, 112:997–999, 2005.

[163] Sarah J. Kilpatrick and Russel K. Laros. Characteristics of normal labor. *Obstetrics and Gynecology*, 74(1):85–87, July 1989.

[164] Matjaz Mihelj. Inverse kinematics of human arm based on multisensor data integration. *Journal of Intelligent Robot Systems*, 47:139–153, 2006.

[165] Jeffrey Allen Nall. High-fidelity birth simulators in american culture: An ecofeminist analysis. *The Journal of American Culture*, 35(1):52–64, March 2012.

[166] Jacob A. Goble, Natalia Dounskaia, and Wanyue Wang. The role of intrinsic factors in control of arm movement direction: implications from directional preferences. *Journal of Neurophysiology*, 105:999–1010, 2010.

[167] A. Zentner, A. Dittmar, P. Gaucherand, M. Cucherat, T. Redarce, O. Dupuis, R. Silveira, and R.C. Rudigoz. Birth simulator: Reliability

of transvaginal assessment of fetal head station as defined by the american college of obstetricians and gynecologists classification. *American Journal of Obstetrics and Gynecology*, 195:868–874, 2005.

[168] O. Olaby. *Obotique pour l'apprentissage de gestes medicaux. Mise en oeuvre de sequences d'accouchement automatisees.* PhD thesis, INSA de Lyon, 2006.

[169] Jessica Clerc, Richard Moreau, Minh-Tu Pham, Olivier Dupuis, and Evelyne Decullier. Does forceps training on a birth simulator allow obstetricians to improve forceps blade placement? *European Journal of Obstetrics, Gynecology, and Reproductive Biology*, 159:305–309, 2011.

[170] Rieko Osu and Hiroaki Gomi. Multijoint muscle regulation mechanisms examined by measured human arm stiffness and emg signals. *Journal of Neurophysiology*, 81:1458–1468, 1999.

[171] J. F. Pearson. Shoulder dystocia. *Current Obstetrics and Gynaecology*, 6:30–34, 1996.

[172] Davind B. Peisner. A device that measures the pulling force and vector of delivering a baby. *American Journal of Obstetrics and Gynecology*, 205:221.e1–7, 2011.

[173] B. Shariat, T. Redarce, R. Buttin, and F. Zara. A biomechanical model of the female reproductive system and the fetus for the realization of a childbirth virtual simulator. In *31st Annual International Conference of the IEEE EMBS*, 2009.

[174] R. W. Prager and R. J. Lapeer. Fetal head moulding: finite element analysis of a fetal skull subjected to uterine pressures during the first stage of labour. *Journal of Biomechanics*, 34:1125–1133, 2001.

[175] I. C. Wright, R. R. Neptune, and A. J. van der Bogert. A method for numerical simulation of single limb ground contact events: Application to heel-toe running. *Computer Methods in Biomechanics and Biomedical Engineering*, 3:321–334, 1999.

[176] Milliard Debrew, David Hananel, Rajesh Aggarwal, and Oliver T. Mytton. Training and simulation for patient safety. *Quality & Safety in Healthcare*, 19(suppl 2):i34–i43, 2009.

[177] Bing-Shiang Yang, Eric J. Perreault, Randy D. Trumbowler, and Matthew A. Krutky. Use of self-selected postures to regulate multi-joint stiffness during unconstrained tasks. *PLoS One*, 4(5):e5411, 2009.

[178] Moreau R, Pham MT, Silveira R, Redarce T, Brun X, and Dupuis O. Design of a new instrumented forceps: Application to safe obstetrical forceps blade placement. *IEEE Transactions on Biomedical Engineering*, 54(7):1280–1290, July 2007.

[179] Gherman RB, Chauhan S, Ouzounian JG, Lerner H, Gonik B, and Goodwin TM. Shoulder dystocia: The unpreventable obstetric emergency with empiric management guidelines. *American Journal of Obstetrics and Gynecology*, 195:657–672, 2006.

[180] Jagadish Sorab, Robert H. Allen, and Bernard Gonik. Risk factors for shoulder dystocia: An engineering study of clinician-applied forces. *Obstetrics and Gynecology*, 77(3):352–355, March 1991.

[181] Lindsay M. Kranker, Tara L. Johnson, Edith D. Gurewitsch, Robert H. Allen, and Stephanie L. Cha. Comparing mechanical fetal response during descent, crowning and restitution among deliveries with and without shoul-

der dystocia. *American Journal of Obstetrics and Gynecology*, 196:539.e1–5, 2007.

[182] Deering S, Poggi S, Macedonia C, Gherman R, and Satin AJ. Improving resident competency in the management of shoulder dystocia with simulation training. *Obstetrics and Gynecology*, 103(6):1224–1228, June 2004.

[183] Joyce C. Foster, Susan L. Hansen, and Steven L. Clark. Active pushing versus passive fetal descent in the second stage of labor: A randomized controlled trial. *Obstetrics and Gynecology*, 99(1):29–34, 2002.

[184] Draycott TJ, Crofts JF, Ash JP, Wilson LV, Yard E, Sibanda T, and Whitelaw A. Improving neonatal outcome through practical shoulder dystocia training. *Obstetrics and Gynecology*, 112(1):14–20, 2008.

[185] Niels Uldbjerg, Tomasz Rechberger, and Hans Oxlund. Connective tissue changes in the cervix during normal pregnancy and pregnancy complicated by cervical incompetence. *Obstetrics and Gynecology*, 71(4):563–567, April 1988.

[186] J.G. Villagrana-Espinosa. Designing a 3d interface to simulate the use of obstetric forceps. Master's thesis, University of East Anglia, 2003.

[187] Wendy M. Murray, Xiao Hu, and Eric J. Perreault. Muscle short-range stiffness can be used to estimate the endpoint stiffness of the human arm. *Journal of Neurophysiology*, 105:1633–1641, 2010.

[188] J. P. VanDorsten, G. D. V. Hankins, L. C. Gilstrap, and F. G. Cunningham. *Operative obstetrics*. Springer, 2002.

[189] Kim E J, Allen R H, Yang J H, McDonald M K, Tam W, and Gurewitsch E D. Simulating complicated human birth for research and training.

In *Conference Proceedings: Annual International Conference of the IEEE Engineering in Medicine and Biology Society*, 2004.

[190] Danilo Ascione, Giuliano Laccetti, Marco Lapegna, and Diego Romano. A real-time method for manipulating a realistic human upper limb. In *Proceedings of the 11th IASTED International Conference Computer Graphics and Imaging (CGIM 2010)*. Acta Press, 2010.

[191] Walter Herzog, Antonie J. van den Bogert, Ahmet Erdemir, and Scott McLean. Model-based estimation of muscle forces exerted during movements. *Clinical Biomechanics*, 22:131–154, 2007.

[192] Bamberg C, Rademacher G, Güttler F, Teichgräber U, Cremer M, Bührer C, Spies C, Hinkson L, Henrich W, Kalache KD, and Dudenhausen JW. Human birth observed in real-time open magnetic resonance imaging. *American Journal of Obstetrics and Gynecology*, 206(6):505.e1–6, 2012.

[193] Bendetti T, Deering SH, and Weeks L. Evaluation of force applied during deliveries complicated by shoulder dystocia using simulation. *American Journal of Obstetrics and Gynecology*, 204:234.e1–5, 2011.

[194] Dena Goffman, Hye Hoe, Setul Pardanani, Irwin R. Merkatz, and Peter S. Bernstein. Improving shoulder dystocia management among resident and attending physicians using simulations. *American Journal of Obstetrics and Gynecology*, 199(3):294.e1–5, 2008.

[195] M. C. Dunkerton. Posterior dislocation of the shoulder associated with obstetric brachial plexus palsy. *The Journal of Bone and Joint Surgery*, 71-B:764–766, 1989.

[196] A. E. Hardy. Birth injuries of the brachial plexus incidence and prognosis. *The Journal of Bone and Joint Surgery*, 63-B:98–101, 1981.

[197] Mark James, Linda P. Hunt, Robert Fox, Timothy J. Draycott, Joanna F. Crofts, and Denise Ellis. Pattern and degree of forces applied during simulation of shoulder dystocia. *American Journal of Obstetrics and Gynecology*, 197:156.e1–6, August 2007.

[198] B H Aylworth. Manikin for illustrating practice of obstetrics, March 1869. US Patent 88,432.

[199] H. R. Beebe. Ball joint between doll head and body, March 1964. US Patent 3,124,901.

[200] John Cotey and Lee S. Volpe. Soft flexible articulated doll, May 1981. US Patent 4,268,991.

[201] Eades G and Knapp C. Dynamic childbirth simulator for teaching maternity patient care, July 1974. US Patent 3,822,486.

[202] Mary M. Jurmain and John C. Fusi. Neck assembly for infant simulator, August 1999. US Patent 5,941,757.

[203] Robert Allen, Edith Gurewitsch, Paul Gilka, Esther Kim, and Parnduangjai Theprungsirikul. Birthing simulator, December 2008. US Patent 7,465,168.

[204] M. Klautsch. Accouchement apparatus for instruction, May 1891. US Patent 451,675.

[205] Blender Online Community. *Blender - a 3D modelling and rendering package*. Blender Foundation, Blender Institute, Amsterdam. http://www.blender.org.

[206] Tomas Möller. A fast triangle-triangle intersection test. *Journal of Graphics Tools*, 2:25–30, 1997.

[207] R.J. Lapeer. A mechanical contact model for the simulation of obstetric forceps in a virtual/augmented environment. In J.D. Westwood, R. S. Haluck, H. M. Hoffman, G. T. Mogel, R. Phillips, R. A. Robb, and K. G. Vosburgh, editors, *Studies in Health Technology and Informatics*, number 111, pages 284–289. IOS Press, January 2005.

[208] Simulia. Abaqus CAE. http://www.3ds.com/.